TECHNISCHE
UNIVERSITÄT
MÜNCHEN

WALTHER-MEISSNER-
INSTITUT FÜR TIEF-
TEMPERATURFORSCHUNG

BAYERISCHE
AKADEMIE DER
WISSENSCHAFTEN

In situ tunable nonlinearity and competing signal paths in coupled superconducting resonators

PhD Thesis

Michael Fischer

Supervisor: Prof. Dr. Rudolf Gross

Munich, January 2021

TECHNISCHE UNIVERSITÄT MÜNCHEN

Fakultät für Physik

In situ tunable nonlinearity and competing signal paths in coupled superconducting resonators

Michael Fischer

Vollständiger Abdruck der von der Fakultät für Physik der Technischen Universität München zur Erlangung des akademischen Grades eines

Doktors der Naturwissenschaften

genehmigten Dissertation.

Vorsitzender:	Prof. Dr. Michael Knap
Prüfer der Dissertation:	1. Prof. Dr. Rudolf Gross
	2. Prof. Jonathan J. Finley, Ph.D.

Die Dissertation wurde am 30.09.2021 bei der Technischen Universität München eingereicht und durch die Fakultät für Physik am 21.01.2022 angenommen.

Contents

List of Figures

Chapter 1

Introduction and Motivation

The concept of quantum simulation was first introduced by Richard Feynman [1] in 1982. He said, that quantum systems are difficult to simulate on classical computers, as they are, by nature, more complex than classical systems. To achieve a fast, reliant and in some cases even a possible simulation, one has to use quantum mechanical simulators in order to model quantum mechanical systems. This requirement stems from the Hilbert space of a quantum mechanical system, which grows exponentially with its particle number. A quantum simulation therefore uses a well defined and otherwise experimentally easier accessible quantum mechanical system to emulate the physics of an experimentally inaccessible quantum system [2].

Platforms for analog quantum simulation

The search for the best simulators for this task is still ongoing after more than 30 years [3]. Advocates for different available platforms are quick to tell you what the advantages of their system of choice are and why it is the only possible solution to all problems. In reality, the Swiss army knife of simulation platforms has not been found yet. Although the currently proposed and used simulators all have their distinct advantages, they also come with a set of disadvantages. Here, we want to give a small overview of the platforms that are most commonly used in quantum simulation experiments. First, there are atoms in optical lattices, also called cold atoms [4]. Atoms are also used in cavity quantum electrodynamics, where atoms are confined in, e.g., optical cavities [5, 6]. Similarly, one can also use ions trapped with electric fields [7]. Another platform are superconducting quantum circuits [8–10], which are often referred to as circuit quantum electrodynamics (cQED). Here, superconducting resonators [11] serve as the equivalent of an optical cavity. Non-linear elements made from Josephson junctions substitute atoms [12–16]. Signals are guided with the help of superconducting waveguides [17]. CQED systems have several important strengths. For one, they offer a high design flexibility, as one can use many different building blocks already invented by the community, such as different quantum bit (qubit) types [10, 18, 19], which can be useful for different types of problems. The different building blocks can then be combined in the circuit design and fabricated

in a scalable way using established thin-film deposition and micro-/nanostructuring techniques [20, 21]. In addition, measurements are typically performed in the microwave regime, where one can borrow highly developed measurement devices and techniques from classical telecommunication applications. Although the design process creates a very well defined experimental system, cQED also allows for in-situ controllability of some design parameters with the help of local electromagnetic fields. For example, one can use a waveguide antenna to control the transition frequency of a qubit with a current source and simultaneously excite this qubit through another waveguide [22–24]. Waveguides and resonators are also able to mediate couplings over longer distances on a sample [25]. It is therefore, in principle, also possible to couple non-neighboring sites. Scalability prospects are promising given the fabrication techniques mentioned above. In practice, however, it has proofed to be quite challenging to actually scale up superconducting circuits, because the increasing cross-talk tends to rapidly destroy the fragile quantum states. Nevertheless, very recently, Martinis et. al were now able to build a chip with 54 qubits [26], proving once and for all that scalability is in fact an advantage of cQED. Superconducting circuits naturally offer low photon loss rates inside a resonator [27, 28] and recent experiments have shown that by using 3D cavities made from aluminum even higher coherence times can be reached [29, 30]. When simulating a many-body system with superconducting circuits, one can use photons to model the particles of the system, which allows to control the number of particles by adjusting a microwave drive power [31]. A steady-state where driving and losses level each other out and the total number of particles is fixed at the chosen value can then be created. This so called driven-dissipative regime is difficult or even impossible to reach in other simulation platforms. The main challenge is the relatively low coupling strength between resonators and non-linear elements and low coherence times of the non-linear elements. But with the help of high fidelity resonators [32] progress is also being made in this direction. Overall cQED is a promising candidate to become the preferred platform for quantum simulation and quantum computing.

Quantum simulations of many-body systems

As already mentioned, the complexity of the Hilbert space of a quantum mechanical system grows exponentially with the number of particles in the system. This is especially critical when discussing many-body physics [33]. Many-body systems are therefore a prime candidate for quantum simulations [34–36]. First simulations in this field have been performed with ultra-cold atoms. After a first simulation of a Bose-Hubbard system [37], multiple more quantum simulations of many-body systems followed and are still being performed [38]. Also other platforms such as trapped ions [39, 40] and cavity QED [41] show interesting experimental results. In the area of cQED, there have also been a number of experimental realization of many-body quantum simulations [42–45]. Here, we want to specifically go into the details of quantum simulations of the Bose-Hubbard model.

Quantum simulation of the Bose-Hubbard model

In the 1980s, the Bose-Hubbard model gained prominence and it describes the interaction of bosons that are confined in a network with next neighbour interactions. The simplest case is a chain of confinement sites. Due to quantum fluctuations a quantum state transition from a superfluid to a mott-insulator phase can occur in such a system, if, e.g., the lattice depth changes. Bosons then switch from being delocalized across the whole lattice to being confined in a single lattice site. The Heisenberg uncertainty relation predicts a stable coherent phase of all particles in the delocalized state and a fluctuating incoherent one in the localized state. Trapped ions proofed to be a good fit to perform quantum simulations of such a system, but it has also been shown, that superconducting circuits offer the capability to simulate Bose-Hubbard physics. In contrast to cold atoms, where interacting bosons are being used, cQED naturally offers non-interacting Bosons, i.e. photons, as the particle of choice. We therefore have to create an environment in which the photons can interact with each other. This is achieved by introducing a Kerr nonlinearity into the lattice formed by superconducting resonators. With this, it has been shown, that we can map the Bose-Hubbard system on a lattice of superconducting non-linear resonators [46–49] and first experimental results have been achieved [50, 51].

Important steps towards experimental quantum simulations

In order to perform large scale quantum simulations using superconducting quantum circuits, careful preparations of the circuit and theory have to be made. In this thesis, we present a system of two nonlinear tunable resonators, suitable for quantum simulation of the Bose-Hubbard model and perform important steps towards its usage as a simulator. As a first step, one has to ensure that the sample emulates the correct physics. We show, that the Hamiltonian of the circuit is equivalent to the one of the Bose-Hubbard model. We also perform classical simulations of the behavior of the system which can later be compared to measurements of the system. This is obviously only possible, as long as the complexity of the system is still low enough. Using the results of these simulations, we design and fabricate a superconducting circuit with the same parameters as the classical simulation. For further experiments, it is vital to fully and fundamentally characterize the sample, including its response to magnetic fields, which tune the resonator parameters. Especially, we need to be able to measure and experimentally control the parameters such as the nonlinearity of the resonators. Additionally, we set up an experimental setup that can be used to measure the quantum effects of the simulator. Taking these steps, we are able to verify the possible usage of our sample in quantum simulation experiments.

Content

This thesis is structured as following. First, in Sec. 2, we give an overview of the theoretical description both of the superconducting circuit we investigate and of the Bose-Hubbard system in general. We also show, that the physics of the circuit are equivalent to the one of the Bose-Hubbard model. In Sec. 3, we show our results of a classical simulation of the Bose-Hubbard model for a two site lattice. Although the phase shift predicted by the Bose-Hubbard model cannot be observed in a two site lattice such as the device presented here, the photon states in each resonator hold interesting quantum mechanical physics. We show, that the theory predicts second order correlation functions both above and below 1 for the photon field inside each resonator and similar results for the cross correlation functions between each resonator. Afterwards, we present our experimental setup and the sample fabrication of the nonlinear two-resonator circuit (Sec. 4). In this part, we also present characterization measurements of the sample, which allows us to understand and control the superconducting circuit within the chosen design space. In Sec. 5, we present further experimental findings of our sample. Most importantly, we extract the nonlinearity of the resonators using two different techniques. First, we model the circuit using a simple circuit model expanded with a parasitic path. From the parameters of this model, we can calculate the nonlinearity. Second, we perform a direct measurement of the nonlinearity from the power dependence of the resonators. With this , we are able to show, that the circuit is suitable for a quantum simulation of the Bose-Hubbard model. Lastly, in Sec. 6, we give a summary of the thesis and a brief outlook towards future projects.

Chapter 2

Theory

2.1 General cQED

In analogy to cavity quantum electrodynamics (QED), circuit quantum electrodynamics (cQED) uses a set of fundamental building blocks such as resonators (similar to cavities) and qubits (similar to atoms) in order to create circuits that allow us to study and use the impact of quantum mechanical effects on the interaction of light and matter. In the following parts, we want to motivate and explain the different building blocks that are important for the experiments in this thesis. Furthermore, we go into the details of the circuits we create and on how to characterize them.

2.1.1 Transmission line

In order to have propagating electromagnetic signals, we use transmission lines. Transmission lines consist of at least two conductors which are separated from each other. Using an ac voltage source, we can create a time varying potential difference between the two conductors which then propagates along the transmission line. We can model a transmission line as a series of lumped element equivalent circuits, that each feature a conductance G_{gap} and capacitance C_{gap} between the conductors and a resistance R_{l} and inductance L_{l} along the line in propagation direction. The conductance stems from the dielectric loss of the separating material, the inductance is the self inductance of the conductors and the capacitance stems from the proximity of the two. Using Kirchhoff's laws, we can derive the so called telegrapher equations [52] in the limit of a vanishing length of the lumped element circuits.

For sinusoidal signals $I(l,t) = I(l)e^{i(\omega t+\pi/2)}$ and $V(l,t) = V(l)e^{i(\omega t)}$ with an angular wave frequency of ω, a travelling wave in the form of

$$V(l) = V_0^+ e^{-\gamma l} + V_0^- e^{\gamma l}, \tag{2.1}$$

$$I(l) = I_0^+ e^{-\gamma l} + I_0^- e^{\gamma l} \tag{2.2}$$

is a solution of the telegrapher equation. Here, γ is the complex propagation function,

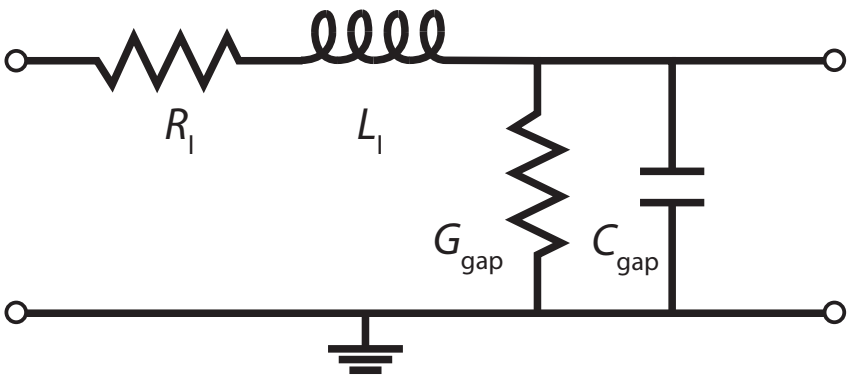

Figure 2.1: Circuit diagram of a lumped element equivalent circuit part of a transmission line.

given as

$$\gamma = \alpha + i\beta = \sqrt{(R_\mathrm{l} + i\omega L_\mathrm{l})(G_\mathrm{gap} + i\omega C_\mathrm{gap}}. \tag{2.3}$$

$e^{-\gamma l}$ ($e^{\gamma l}$) describes the propagation in positive (negative) l direction with amplitudes V_0^+ (V_0^-) and I_0^+ (I_0^-). Note that α, the real part of γ, describes the damping of the travelling wave, and the imaginary part β its propagation properties.

We can derive a relation between the voltage and current for a given direction as

$$\frac{V_0^+}{I_0^+} = Z_0, \tag{2.4}$$

with

$$Z_0 = \sqrt{\frac{R_\mathrm{l} + i\omega L_\mathrm{l}}{G_\mathrm{gap} + i\omega C_\mathrm{gap}}}. \tag{2.5}$$

At low temperatures, we can estimate R_l to be very close to 0, as the conductors are superconducting. Similarly, also the conductance G_gap can be neglected, as we use high-resistivity silicon as dielectric material separating the conductors. Therefore Eq. (2.5) simplifies to

$$Z_0 = \sqrt{\frac{L}{C}}. \tag{2.6}$$

Z_0, the characteristic impedance of the transmission line, plays an especially important role, if we combine multiple elements, e.g. two transmission lines. At the transition from a transmission line with impedance $Z_{0,1}$ to one with impedance $Z_{0,2}$, part of the signal will be reflected. The reflection coefficient of such a connection is given by

$$r = \frac{Z_{0,1} - Z_{0,2}}{Z_{0,1} + Z_{0,2}}. \tag{2.7}$$

For a non-matched connection, $r \neq 0$, one obtains reflections, which can lead to interference effects. Hence, it is advised to keep impedance mismatches as small as possible. We therefore match all our circuits to the industrial standard for devices and cables of $Z_0 = 50\,\Omega$. In this simplified case, we can also easily calculate the phase velocity of the propagating wave to be

$$v_\mathrm{p} = \frac{\omega}{\beta} = \frac{1}{\sqrt{LC}}. \tag{2.8}$$

2.1.2 Scattering matrix

In order to describe the effect an arbitrary system has on a traveling wave described by Eq. (2.1), we define the scattering matrix for a two-port system by the voltage amplitudes entering (V^-) and exiting (V^+) the system

$$\begin{bmatrix} V_1^+ \\ V_2^+ \end{bmatrix} = \begin{bmatrix} S_{11} & S_{12} \\ S_{21} & S_{22} \end{bmatrix} \begin{bmatrix} V_1^- \\ V_2^- \end{bmatrix}. \tag{2.9}$$

Here, each element of the scattering matrix can be calculated or measured by the relation

$$S_{ij} = \left.\frac{V_i^-}{V_j^-}\right|_{V_k^+ = 0,\ \text{for}\ k \neq i}. \tag{2.10}$$

In this thesis, we refer to transmission or reflection measurements meaning a measurement of the transmission coefficient or magnitude $T = |S_{ij}|^2$ for $i \neq j$ or the reflection coefficient or magnitude $R = 1 - T = |S_{ii}|^2$.

For a better visualization of the features in our measurements, we typically plot the scattering parameters in dB

$$S_{ij}(\mathrm{dB}) = 20\log(S_{ij}). \tag{2.11}$$

In some measurements, we also show the phase ϕ of the scattering parameter, which can be calculated via

$$\phi = \arg(S_{ij}) = \operatorname{arctan2}\left(\Im(S_{ij}), \Re(S_{ij})\right). \tag{2.12}$$

2.1.3 Resonators

The previously discussed transmission line can hold a continuum of modes for a broad frequency range. In vast contrast to this, a microwave resonator can only support excitations in a small frequency band. To understand its behavior, we can model a

microwave resonator as a parallel RLC circuit. Such a circuit has an input impedance of

$$Z_{\text{in}} = \left(\frac{1}{R} + \frac{1}{i\omega L} + j\omega C\right)^{-1}. \tag{2.13}$$

Resonance occurs, when the average energy stored in the inductance $W_{\text{ind}} = \frac{1}{4}|V|^2 \frac{1}{\omega^2 L}$ and capacitance $W_{\text{cap}} = \frac{1}{4}|V|^2 C$ are equal. From this we can calculate a resonant frequency of

$$\omega_0 = \frac{1}{\sqrt{LC}}. \tag{2.14}$$

At this frequency, a standing wave forms inside the resonator. For a $\lambda/2$ resonator, we can calculate and therefore design the resonant frequency using the length l of the resonator

$$l = \frac{\pi v_{\text{p}}}{\omega_0} = \frac{\pi \text{c}}{n\omega_0}. \tag{2.15}$$

The phase velocity $v_{\text{p}} = \frac{\text{c}}{n}$ depends only on the speed of light c and the refractive index n. As the field of the wave lives both in the chip substrate silicon ($n \approx 4$) and the air above the chip ($n \approx 1$), the actual refractive index is a combination of the two and can be estimated to be $n = \sqrt{(1+\epsilon_{\text{r}})/2}$ where ϵ_{r} is the relative permittivity of silicon.

Q Factor

A signal entering a resonator can oscillate there many times, so that even small losses can add up and drastically change the behavior of the system. To account for these losses, we introduce the Q factor (quality factor) of a resonator as

$$Q = \omega \frac{\text{average energy stored}}{\text{energy loss/second}} = \omega \frac{W_{\text{m}} + W_{\text{e}}}{P_{\text{loss}}}. \tag{2.16}$$

For the resonant case of a parallel circuit, we get an unloaded or internal quality factor of $Q_{\text{int}} = \omega_0 RC$. The unloaded quality factor only takes internal losses into account. Additional loss channels to the outside, which are introduced, e.g., by coupling to an external transmission line, are being taken into account in the loaded quality factor

$$\frac{1}{Q_{\text{l}}} = \frac{1}{Q_{\text{ext}}} + \frac{1}{Q_{\text{int}}} \tag{2.17}$$

We can also show that the full width at half maximum κ_{tot} of the resonance is related to the loaded quality factor of a $\lambda/2$ resonator in a transmission experiment

$$Q_l = \frac{\omega_0}{\kappa_{\text{tot}}}. \tag{2.18}$$

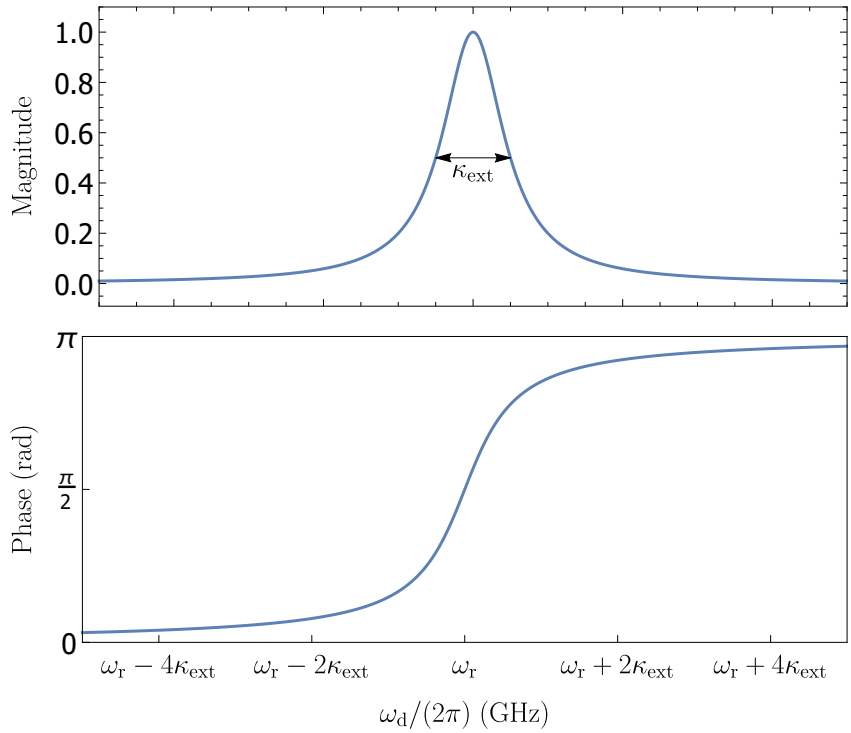

Figure 2.2: Magnitude and phase of the transmission through a $\lambda/2$ resonator. The magnitude exhibits a peak at the resonance frequency with a width that is related to the loss rate of the resonator. The phase shifts by π.

Transmission through a resonator

We can use an input output formalism [53] to model a single-resonator system and calculate transmission and reflection of the resonator. We assume the resonator to be capacitively coupled to a transmission line at both ends. The boundary conditions can then be written as

$$\begin{aligned} a_{\mathrm{IN}} - a_{\mathrm{OUT}} &= \sqrt{\frac{\kappa_{\mathrm{ext}}}{2}} a \\ -b_{\mathrm{IN}} + b_{\mathrm{OUT}} &= \sqrt{\frac{\kappa_{\mathrm{ext}}}{2}} a. \end{aligned} \tag{2.19}$$

a_{IN} and a_{OUT} (b_{IN} and b_{OUT}) are the signals flowing in and out of the left (right) side of the resonator. Left flowing signals are negative by convention. κ_{ext} is the coupling rate of the resonator to the transmission lines excluding internal losses in the resonator. For simplicity reasons we assume that the coupling rates to both sides are equal. We neglect internal losses of the resonator. The field inside the resonator can then be written as a

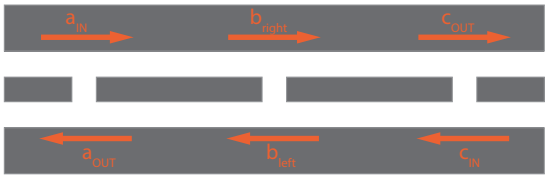

Figure 2.3: Sketch of the signal flow in a two resonator system.

function of the input signals,

$$a = \frac{\sqrt{\frac{\kappa_{\text{ext}}}{2}}a_{\text{IN}} - \sqrt{\frac{\kappa_{\text{ext}}}{2}}b_{\text{IN}}}{\frac{\kappa_{\text{ext}}}{2} - i(\omega - \omega_0)}. \tag{2.20}$$

Combining these equations, we obtain the output field a_{OUT} as a function of the input fields,

$$a_{\text{OUT}} = \frac{i(\omega - \omega_0)a_{\text{IN}} - \frac{\kappa_{\text{ext}}}{2}b_{\text{IN}}}{\frac{\kappa_{\text{ext}}}{2} - i(\omega - \omega_0)}. \tag{2.21}$$

Equivalently, we can derive an expression for b_{OUT}. In Fig. 2.2, we plot the magnitude (top panel) and phase (bottom panel) of the output field for $a_{\text{IN}} = 0$ and $b_{\text{IN}} = 1$. We observe a resonance peak with amplitude 1 at the resonance frequency ω_0, meaning that all power is transmitted through the resonator. The FWHM is equal to the loss rate κ_{ext}. Looking at the phase, we can see a clear phase shift of π that occurs on the scale of the bandwidth of the resonance.

Transmission through a two-resonator system

Going towards more complex structures, we next look at a system of coupled resonators. Similarly to the previous calculation, we look at system where the resonators are capacitively coupled the transmission line as input and output ports. The two resonators are additionally capacitively coupled to each other. A sketch of this can be seen in Fig. 2.3. We expand the calculations of the input and output formalism shown previously to model not only the resonators as individual devices, but also the coupling between them. The signals flowing into, out and inside of the system can be calculated from the fields a and c inside the resonators

$$\begin{aligned} a_{\text{IN}} - a_{\text{OUT}} &= \sqrt{\kappa_{\text{ext}}}a \\ -b_{\text{left}} + b_{\text{right}} &= \sqrt{\kappa_{\text{c}}}a \\ -b_{\text{left}} + b_{\text{right}} &= \sqrt{\kappa_{\text{c}}}c \\ -c_{\text{IN}} + c_{\text{OUT}} &= \sqrt{\kappa_{\text{ext}}}c. \end{aligned} \tag{2.22}$$

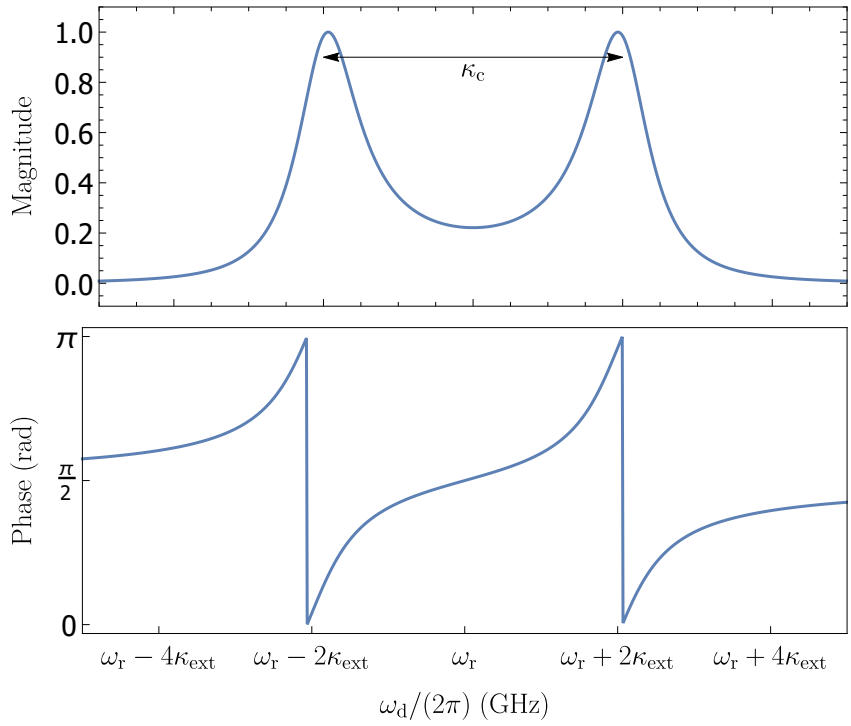

Figure 2.4: Transmission magnitude and phase of a two resonator system with $\kappa_{ext} = 10\,\text{MHz}$, $\kappa_c = 40\,\text{MHz}$ and $\omega_0 = 7.0\,\text{GHz}$. We observe two distinct peaks in the magnitude that are separated by the coupling rate.

The definition of signals can be seen in Fig. 2.3. a_{IN} and a_{OUT} (c_{IN} and c_{OUT}) are the signals flowing in and out of the left (right) resonator. Note that all signals flowing to the right have a plus sign while the ones flowing to the left have a minus sign. The signals b_{left} and b_{right} couple the resonators via a capacitor with coupling rate κ_c. The resonators are coupled to the external transmission lines with κ_{ext}. We neglect internal losses of the system.

On the other hand, we can describe the fields inside the resonators as a function of the input signals:

$$a = \frac{\sqrt{\kappa_{ext}}a_{IN} - \sqrt{\kappa_c}b_{left}}{\frac{\kappa_{ext}+\kappa_c}{2} - i(\omega - \omega_0)} \tag{2.23}$$

$$c = \frac{\sqrt{\kappa_c}b_{right} - \sqrt{\kappa_{ext}}c_{IN}}{\frac{\kappa_{ext}+\kappa_c}{2} - i(\omega - \omega_0)}. \tag{2.24}$$

If we use these expressions for the fields in Eq. (2.22), we find the coupled equations

$$b_{\text{right}} = \frac{\sqrt{\kappa_{\text{ext}}\kappa_{\text{c}}}a_{\text{IN}} + \left(\frac{\kappa_{\text{ext}}-\kappa_{\text{c}}}{2} - i\left(\omega-\omega_0\right)\right) b_{\text{left}}}{\frac{\kappa_{\text{ext}}+\kappa_{\text{c}}}{2} - i\left(\omega-\omega_0\right)} \tag{2.25}$$

$$b_{\text{left}} = \frac{\sqrt{\kappa_{\text{ext}}\kappa_{\text{c}}}c_{\text{IN}} + \left(\frac{\kappa_{\text{ext}}-\kappa_{\text{c}}}{2} - i\left(\omega-\omega_0\right)\right) b_{\text{right}}}{\frac{\kappa_{\text{ext}}+\kappa_{\text{c}}}{2} - i\left(\omega-\omega_0\right)}, \tag{2.26}$$

and a function for the output signals in a reflection measurement where a_{IN} or c_{IN} are 0 respectively,

$$c_{\text{OUT}} = \frac{\sqrt{\kappa_{\text{ext}}\kappa_{\text{c}}}b_{\text{right}} + \left(\frac{\kappa_{\text{c}}-\kappa_{\text{ext}}}{2} - i\left(\omega-\omega_0\right)\right) c_{\text{IN}}}{\frac{\kappa_{\text{ext}}+\kappa_{\text{c}}}{2} - i\left(\omega-\omega_0\right)} \tag{2.27}$$

$$a_{\text{OUT}} = \frac{\sqrt{\kappa_{\text{ext}}\kappa_{\text{c}}}b_{\text{left}} + \left(\frac{\kappa_{\text{c}}-\kappa_{\text{ext}}}{2} - i\left(\omega-\omega_0\right)\right) a_{\text{IN}}}{\frac{\kappa_{\text{ext}}+\kappa_{\text{c}}}{2} - i\left(\omega-\omega_0\right)} \tag{2.28}$$

To get an expression for c_{OUT} we solve Eqs. (2.25) and (2.26) for b_{right} and plug it into equation (2.28).

In Fig. 2.4, we plot the magnitude and phase of the output field c_{OUT} for $a_{\text{IN}} = 1$ and $c_{\text{IN}} = 0$. In magnitude, we observe a splitting of the resonance peak by the coupling strength $\kappa_{\text{c}} = 40\,\text{MHz}$. The bare resonance frequencies of the two resonators are chosen to be equal. The coupling lifts the degeneracy of the resonance modes, which differ in frequency. Note that the linewidth of the two resonators is not influenced by the coupling and is still determined by the external coupling rates κ_{ext}. The two-resonator system is analogous to two pendula which are coupled with a spring. At the resonance with a lower frequency, the resonators oscillate in phase, at the resonance with a higher frequency, they oscillate out of phase.

The phase of transmission undergoes a jump at each effective resonance frequency.

2.1.4 Josephson junctions as nonlinear elements

So far we only looked at linear circuits, but superconducting circuits also offer easy access to nonlinear elements. The most prominent one is the Josephson junction (JJ) which makes use of the Josephson effect. In this section, we give a brief introduction to JJs before introducing a so called DC superconducting interference device (SQUID) as a particularly relevant example of a superconducting nonlinear circuit.

Josephson junctions

Josephson junctions consist of two superconducting electrodes separated by a thin layer of nonsuperconducting material. Due to the small separation of the two electrodes, the two superconducting wave functions overlap and allow for a superconducting current flowing

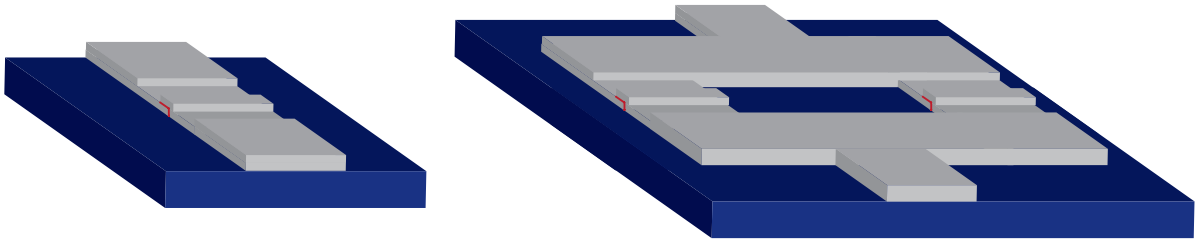

Figure 2.5: Sketch of a Josephson junction (left) and a DC-SQUID (right). Metal parts are shown in silver, the insulating layer is shown in red. Although not visible, the insulating layer expands through the whole width of the junction, completely separating the two electrodes from each other. The structure in the metal parts stems from fabrication (Sec. 4.1.2).

across the junction. This current is carried by tunneling Cooper pairs. Here, we focus on superconductor-insulator-superconductor (SIS) junctions, where, as the name suggests, the two superconductors are separated by an insulating layer. Josephson showed that both the superconducting tunnel current I_s through the junction and the voltage drop V between the two superconductors depend on the phase difference φ of the corresponding macroscopic wave functions in each electrode. The first Josephson equation is

$$I_\mathrm{s} = I_\mathrm{c} \sin \varphi. \tag{2.29}$$

The supercurrent I_s cannot exceed the material- and dimension-dependent critical current I_c and depends on the sine of the phase difference between the macroscopic wavefunctions of the Cooper pairs at each side of the junction. A change of this phase difference in time relates to a voltage drop across the junction, as can be seen in the second Josephson equation

$$\dot{\varphi} = \frac{2\pi}{\Phi_0} U, \tag{2.30}$$

with the magnetic flux quantum $\Phi_0 = h/2e$, where h is the Planck constant and e the elementary charge. When integrating the second Josephson equation and combining it with the first one, we find, that the super current through the junction is oscillating in time with a frequency of $2\pi V/\Phi_0$ if we apply a DC voltage V.

The nonlinearity of the junction also shows when we calculate its inductance from the Josephson equations

$$L_j = \frac{U}{\mathrm{d}I_\mathrm{s}/\mathrm{dt}} = \frac{\Phi_0}{2\pi I_\mathrm{c} \cos(\varphi)}. \tag{2.31}$$

The important energy scales of a JJ are its Josephson energy E_j and its charging energy E_C. E_j describes the energy that is stored in the junction for no applied current and can

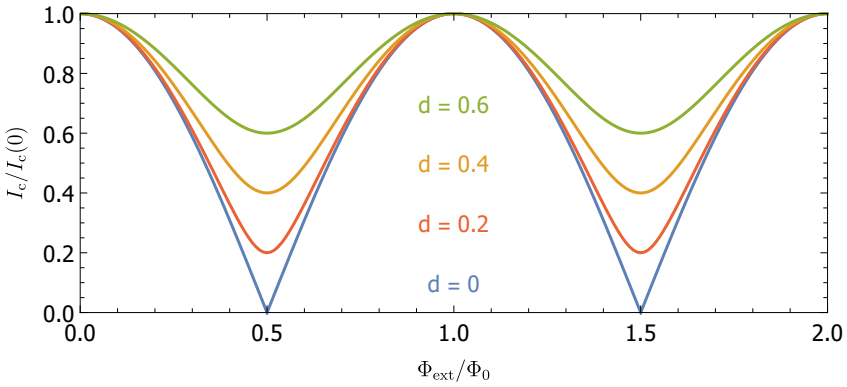

Figure 2.6: Critical current as a function of the external flux for different asymmetry parameters. The critical current is tuned from its maximum to its minimum and back by applying Φ_0. The minimal value increases with increasing asymmetry parameter d.

be calculated via

$$E_j = \int_0^{\varphi} (I_s U) \mathrm{d}\tilde{\varphi} = \frac{\Phi_0 I_c}{2\pi}(1 - \cos\varphi) = E_{J0}(1 - \cos\varphi). \tag{2.32}$$

The charging energy $E_C = e^2/2C_j$ describes the energy stored inside the capacitance C_j of the junction.

DC-SQUIDs

A DC-SQUID is a parallel circuit with two Josephson junctions [54] in its arms. It inherits many of the properties of a single junction, such as the critical current flowing through the SQUID, which is the sum of the critical currents of the individual junctions

$$I_{c,tot} = I_{c1} + I_{c2}. \tag{2.33}$$

Due to interference effects in the SQUID loop, this total critical current can be modulated by applying an external flux Φ_{ext} through the loop

$$I_c(\Phi) = I_{c,tot}(0) \left| \cos\left(\pi \frac{\Phi_{ext}}{\Phi_0}\right) \right|. \tag{2.34}$$

This formula holds only true if the screening parameter $\beta_L = \frac{2LI_{c,tot}}{\Phi_0} \ll 1$ and if $I_{c1} = I_{c2}$. For larger screening parameters, the loop inductance L plays a larger role and the critical current will not reduce to 0. Note that Eq. (2.34) allows us to directly control the nonlinear inductance of the junction (see Eq. (2.31)). By applying an external flux to the SQUID loop, we decrease the critical current below its maximum value and, in turn, increase the inductance of the junction. In practice, the fabrication accuracy is not high enough to ensure equal critical currents for both junctions. A difference in the two currents changes

the behavior of Eq. (2.34) in the following way

$$I_c(\Phi) = I_{c,tot}(0)\left|\cos\left(\pi\frac{\Phi_{ext}}{\Phi_0}\right)\right|\sqrt{1+d^2\tan^2\left(\pi\frac{\Phi_{ext}}{\Phi_0}\right)}, \tag{2.35}$$

with the asymmetry parameter $d = (I_{c1} - I_{c2})/I_{c,tot}$. As it can be seen in Fig. 2.6, an increase in asymmetry also increases the minimal critical current we can reach. This effect reduces the maximal nonlinearity of the junction. On the plus side, the junction becomes less susceptible to flux noise as the flux derivative flattens. For this reason, we design our SQUIDs to be asymmetric. For more details see Sec. 4.1.

2.1.5 Nonlinear resonators

We now look at more complex circuits, that can be build by combining the previously introduced devices. By galvanically coupling a DC-SQUID to a resonator, we can use its nonlinearity to change the excitation spectrum of the resonator. In order to understand the behavior of this coupled system, we first look at the field inside the resonator and how it is changed by the presence of the SQUID.

Mode function of a resonator

We can write the field $\Psi(x,t) = \int_{-\infty}^{t} V(x,t)dt$ inside the resonator as a sum over combinations of time-dependent $\psi_m(t)$ and dimensionless spatial modes $u_m(x)$

$$\Psi(x,t) = \sum_m \psi_m(t)u_m(x). \tag{2.36}$$

The Lagrangian of a $\lambda/2$-resonator with length l is then given by

$$\mathcal{L} = \int_{-l/2}^{l/2}\left[\frac{C_0(x)}{2}\dot{\Psi}^2(x,t) - \frac{[\partial_x\Psi(x,t)]^2}{2L_0(x)}\right]dx, \tag{2.37}$$

with the capacitance per unit length C_0 and inductance per unit length L_0. We can write the Lagrangian for the capacitances as

$$\mathcal{L}_{input} = \frac{C_{io}}{2}[\dot{\Psi}(-L/2,t) - V_{input}(t)]^2 \tag{2.38}$$

$$\mathcal{L}_{output} = \frac{C_{io}}{2}[\dot{\Psi}(L/2,t) - V_{output}(t)]^2, \tag{2.39}$$

with $V_{input/output}$ being the input and output voltages at the ends of the resonator which are coupled to transmission lines with a capacitance of C_{io}. Lastly, the Lagrangian of the

SQUID is given by

$$\mathcal{L}_j = \frac{C_j}{2}\dot{\delta}^2 + E_j \cos\left(\frac{2\pi\delta}{\Phi_0}\right). \tag{2.40}$$

Expanding the cosine allows us to separate the full description of the resonator into a linearized part and a fully nonlinear part.

$$\mathcal{L} = \mathcal{L}'_{\mathrm{r}} + \mathcal{L}_{\mathrm{input}} + \mathcal{L}_{\mathrm{output}} - U_{\mathrm{NL}}(\delta). \tag{2.41}$$

Coupling the system via output capacitors to transmission lines places boundary conditions on the voltage of the field, which depend on the bias voltage at the capacitances. In addition to this, the currents flowing on the left and right side of the junction have to be equal, which leads to the relation

$$\frac{1}{L_0}\partial_x \Psi(x,t) = C_j\ddot{\delta} + \frac{\delta}{L_j} \tag{2.42}$$

Both of these conditions can be fulfilled with a sinusoidal envelope function

$$u_m(x) = \begin{cases} A_l \sin[k_m(x + l/2) - \varphi_m^l] \\ A_r \sin[k_m(x - l/2) - \varphi_m^r] \end{cases}. \tag{2.43}$$

For equal impedance, capacitance per unit length and inductance per unit length, we find two possible constrains on $A_{l,r}$ where either $A_r = A_l$ (even modes) or $A_r = -A_l$ (odd modes).

If we plug this ansatz into Eq. (2.42), we obtain a transcendental equation for the wave vector k_m

$$k_m^{\mathrm{odd}} \tan\left(k_m^{\mathrm{odd}}\frac{l}{2}\right) = -\frac{Z_0}{\nu}C_j\left(\omega_{\mathrm{p}}^2 - (k_m^{\mathrm{odd}}\nu)^2\right), \tag{2.44}$$

with the plasma frequency of the Josephson junction $\omega_{\mathrm{p}} = 1/\sqrt{C_j L_j}$ and the phase velocity $\nu = 1/\sqrt{C_0 L_0}$. Equivalently, we can also get an equation for the wave vectors of the even modes. Numerically solving these equation gives us possible wave vectors for different values of ω_p, which depends on the external flux bias via L_j. Using Eq. (2.43), we can then calculate the spatial mode function of the fields inside the resonator at resonance frequency dependent on the external flux (see Fig. 2.7). We can see that even modes are not effected by the presence of the SQUID. Odd modes experience a jump in the spatial mode function at the SQUID location. This stems from the fact that even modes have vanishing current at the SQUID location. The jump Δu in the odd modes can be directly calculated as the difference between the mode on the left (position x_j^-) and right (position x_j^+) side of the junction, $\Delta u = u(x_j^-) - u(x_j^+)$. This quantity is a direct measure

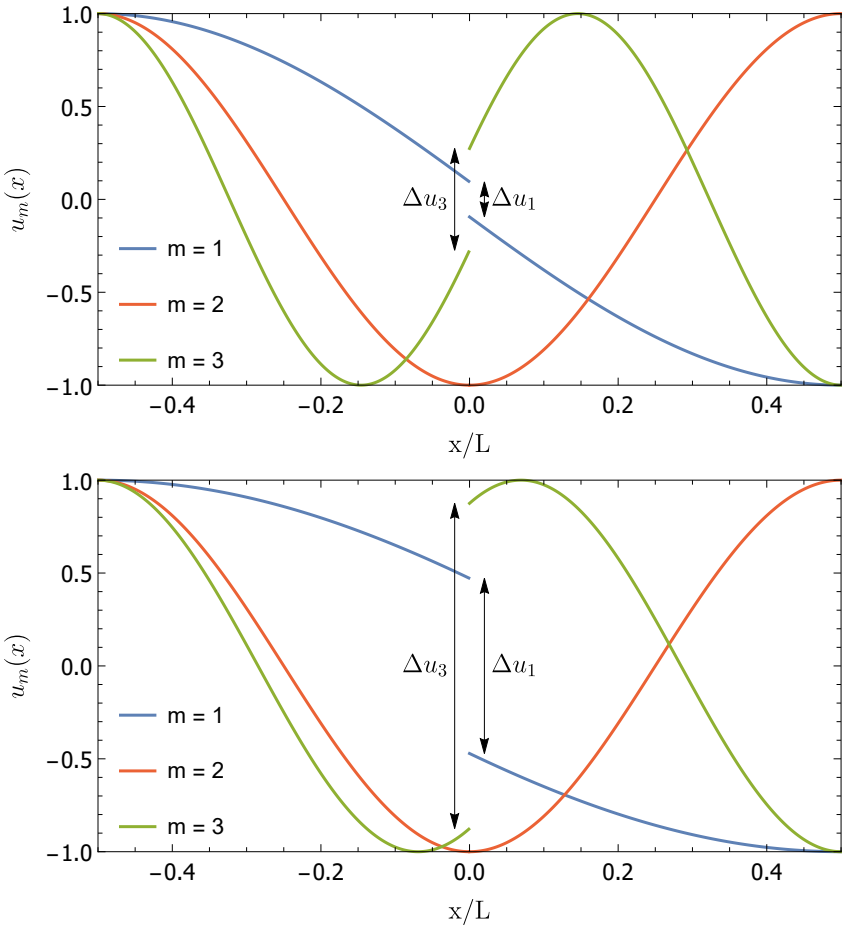

Figure 2.7: First three modes of the spatial mode function of the field inside a resonator with a SQUID in the center for different values of external flux. The top picture shows the modes for an external flux $\Phi_{\text{ext}} = 0$, the bottom one for $\Phi_{\text{ext}} = \Phi_0$.

for the strength of the nonlinearity (see Sec. 2.1.6) of the system. We can also see that Δu depends on the externally applied flux. At $\Phi_{\text{ext}} = 0$, the nonlinearity is minimal, leading to the smallest jump in the mode (Fig. 2.7, top panel). At $\Phi_{\text{ext}} = \Phi_0/2$, the nonlinearity is at its maximum and therefore the jump is at its maximum. If we look at a symmetric SQUID ($d = 0$), the jump would be equal to 1, but in our system it is reduced due to the finite asymmetry ($d = 0.13$).

Looking at the wave form of the resonator, we can see that the SQUID elongates the wavelength of the resonance. This leads to a decrease of the resonance frequency $\omega_r/(2\pi) = k\nu$ dependent on the height of the jump at the SQUID. Therefore, the resonator exhibits its maximum resonance frequency at zero flux bias and its minimum resonance frequency at $\Phi_{\text{ext}} = \Phi_0/2$ (see Fig. 2.8). At this point, in the case of a symmetric SQUID, the wavelength would reach infinity, leading to a resonance frequency of zero. Due to the asymmetry of our SQUID, the resonance frequency does not modulate to zero (see Fig. 2.6).

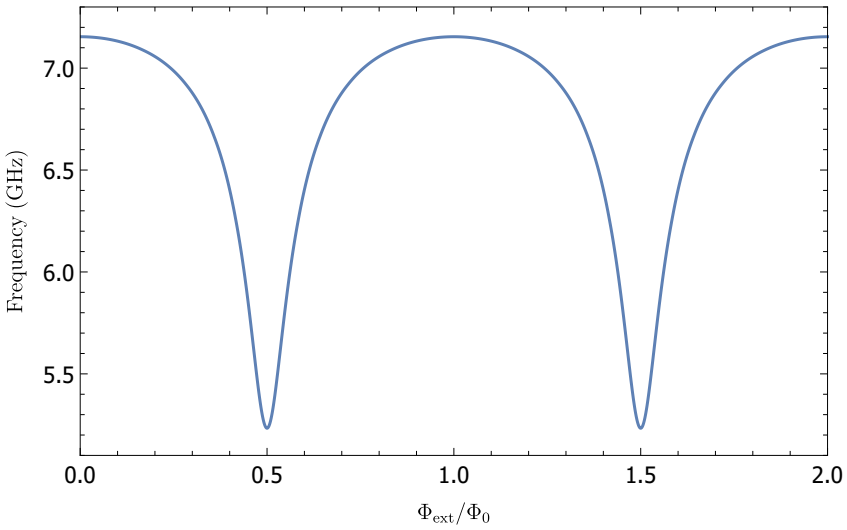

Figure 2.8: Resonance frequency of the first mode of a resonator with a SQUID in the center, as a function of the external flux bias Φ_{ext}. The parameters for this calculation have been taken from Tab. 4.2.

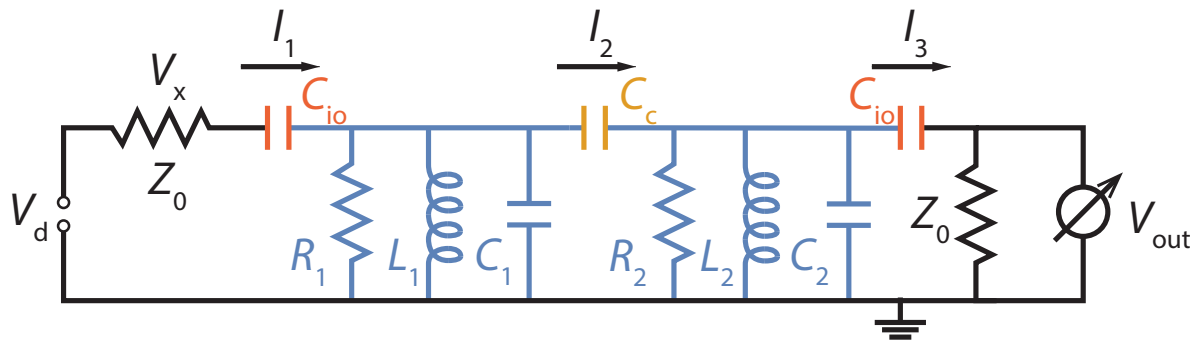

Figure 2.9: Circuit diagram of a two-resonator (blue) system coupled to a transmission line and to each other via lumped-element capacitors (red and yellow).

Circuit model of a two-resonator system

In order to better understand our system, we create a circuit description of a serially connected, capacitively coupled two-resonator system. From this we can extract scattering parameters and various interesting parameters such as the coupling capacitances, the resonator capacitance and inductance and the resonance frequencies of the coupled system. In this first calculation, we include the dependency of the spatial mode function on the SQUID inductance, but ignore its nonlinear effects that arise if we heavily drive the system. The previously given Langrangian for the output capacitances of the single resonator

system change to

$$\mathcal{L}_{\text{input}} = \frac{C_{\text{io}}}{2}[\dot{\Psi}_1(-L/2,t) - V_{\text{input}}(t)]^2 \tag{2.45}$$

$$\mathcal{L}_{\text{output}} = \frac{C_{\text{io}}}{2}[\dot{\Psi}_2(L/2,t) - V_{\text{output}}(t)]^2. \tag{2.46}$$

The fields $\Psi_{\text{n}}(x,t)$ are here the fields of resonators n= 1,2, with x being the position inside each resonator. The coupling capacitance adds an additional equation,

$$\mathcal{L}_{\text{c}} = \frac{C_{\text{c}}}{2}[\dot{\Psi}_1(L/2,t) - \dot{\Psi}_2(-L/2,t)]^2. \tag{2.47}$$

A circuit diagram can be seen in Fig. 2.9. We use the Norton approach, where we model the resonator as a distributed parallel circuit. For the driving voltage (V_{d}) and output voltage (V_{out}) we find

$$V_{\text{d}} = Z_0 I_1 + V_{\text{x}} \tag{2.48}$$

$$V_{\text{out}} = Z_0 I_3, \tag{2.49}$$

with I_1 (I_3) being the current flowing into (out of) the two resonator system. V_{x} is the voltage drop across the impedance Z_0 of the input cable.

We can describe the currents I_i flowing in our system using the amplitude of the voltage mode V_j at the in- and output capacitors (capacitance C_{io}) and the coupling capacitor (capacitance C_{c}). The index i of I_i denotes the capacitor starting from driving side, the index j of V_j the resonator number.

$$I_1 = (V_{\text{x}} - V_1) i\omega_d C_{\text{io}} \tag{2.50}$$

$$I_2 = (-V_1 - V_2) i\omega_d C_{\text{c}} \tag{2.51}$$

$$I_3 = (-V_2 - V_{\text{out}}) i\omega_d C_{\text{io}}. \tag{2.52}$$

As we are looking at odd voltage modes, the signs of V_1 and V_2 change at their second appearance. In each resonator the in- and outflowing currents have to be the same,

$$I_1 = (i\omega_d C_1 + \frac{1}{R_1} + \frac{1}{i\omega_d L_1})V_1 - I_2, \tag{2.53}$$

$$I_2 = (i\omega_d C_2 + \frac{1}{R_2} + \frac{1}{i\omega_d L_2})V_2 - I_3. \tag{2.54}$$

Here, C_n, L_n and R_n are the capacitance, inductance and resistance of resonator $n = 1,2$. To include the tunability of the circuit introduced by the DC-SQUIDs, we calculate C_i and L_i as functions of the external flux Φ_{ext} penetrating the SQUID loops, using the standard ansatz for the spatial mode functions $u_i(x)$ introduced in Sec. 2.1.5:

$$C_i = C_j \Delta u_{\mathrm{m}}\left(k,\Phi_{\mathrm{ext}}\right)^2 + C_0 \int_{-L/2}^{+L/2} u_{\mathrm{m}}\left(x,k,\Phi_{\mathrm{ext}}\right)^2 \mathrm{dx}, \tag{2.55}$$

$$\begin{aligned} L_i = \Bigg(& \frac{1}{L_0} \int_{-L/2}^{+L/2} \left(\delta_{\mathrm{x}} u_{\mathrm{m}}\left(x,k,\Phi_{\mathrm{ext}}\right)^2\right) \mathrm{dx} \\ & + \frac{1}{L_j\left(\Phi_{\mathrm{ext}}\right)} \Delta u_{\mathrm{m}}\left(k,\Phi_{\mathrm{ext}}\right)^2 \Bigg)^{-1}. \end{aligned} \tag{2.56}$$

The S-Parameters calculated with this circuit model are used in Sec. 5.1.

2.1.6 Hamiltonian of the two-resonator system

The total Lagrangian of the system, including two resonators ($i = 1, 2$), the coupling between them and the two DC-SQUIDS, can be written as

$$\mathcal{L}_{\mathrm{tot}} = \sum_{i=1}^{N=2} \left[\mathcal{L}_{\mathrm{r},i} + \mathcal{L}_{\mathrm{J},i}\right] + \mathcal{L}_{\mathrm{input}} + \mathcal{L}_{\mathrm{output}} + \mathcal{L}_{\mathrm{c}}. \tag{2.57}$$

We perform a Legendre transformation and quantize the field [48] with ladder operators, leaving us with the full Hamiltonian of

$$\hat{H} = \hbar \sum_{i=1}^{2} \omega_{\mathrm{r},i} \hat{n}_i + \hbar C_{\mathrm{c}} \sqrt{\frac{\omega_{\mathrm{r},1}\omega_{\mathrm{r},2}}{C_1' C_2'}} \left(\hat{a}_1^\dagger \hat{a}_2 + \hat{a}_2^\dagger \hat{a}_1\right) - \frac{e^2}{2\hbar L_{\mathrm{J}}} \sum_{i=1}^{2} \frac{L_i'}{C_i'} \left(\Delta u_i\right)^4 \left(\hat{a}_i^\dagger \hat{a}_i^\dagger \hat{a}_i \hat{a}_i\right). \tag{2.58}$$

For $\omega_{\mathrm{r},1} = \omega_{\mathrm{r},2}$ and $C_1' = C_2'$, we can define the coupling constant between the two resonators as

$$J = -\omega_{\mathrm{r}} \frac{C_{\mathrm{c}}}{C'} \tag{2.59}$$

and a purely nonlinear term

$$U = -\frac{e^2}{2\hbar} \frac{L'}{C'} \frac{(\Delta u)^4}{L_{\mathrm{J}}}. \tag{2.60}$$

We will show in Sec. 2.2 that this Hamiltonian is equivalent to the one of a Bose-Hubbard system.

2.1.7 Circuit model with addition of a parasitic path

In our measurements, we cannot view our system as an isolated instance without any influences from its environment, but have to take possible interactions with background fields into account. This includes, e.g., standing waves inside a not optimally impedance matched cable or a box mode inside the sample box. When the input signal couples to a mode in the sample box, this interaction opens up new paths that the signal can take to reach the output port without exciting the resonator system. In the following, we call

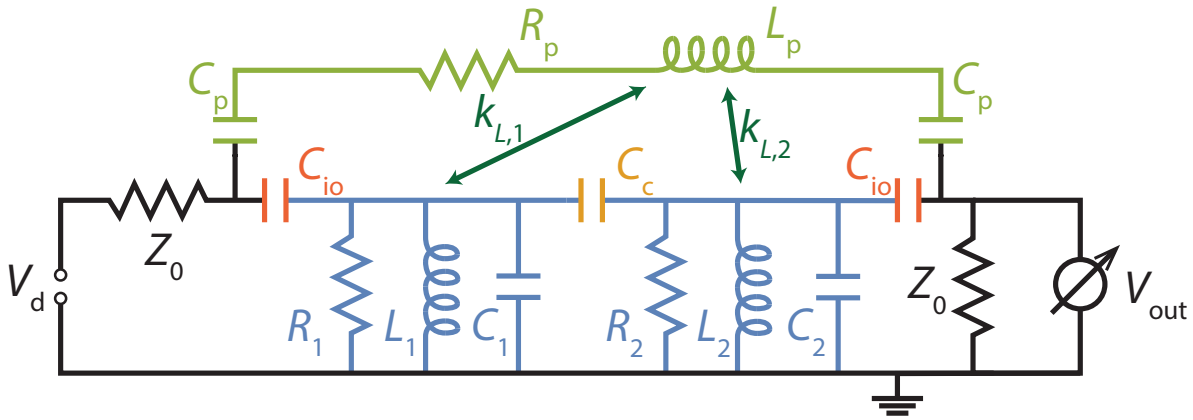

Figure 2.10: Circuit model of the two resonator system. Resonators are shown in blue along with their coupling (yellow) and input/output (red) capacitors. The parasitic path is shown in green and input and output lines in black. The path is capacitively coupled to the input and output lines and inductively coupled to the resonators with the strength quantified by the coupling constants $k_{L,i}$. Microwave drive and measurement signal are denoted by V_d and V_out, respectively. Here, the contribution of the SQUIDs is included in the effective capacitance C_i and inductance L_i of the resonators.

such an additional path a parasitic path.

In Fig. 2.10, we introduce such a parasitic path into the circuit model, that couples both capacitively to the input and output lines of the resonators and inductively to the inductance of each resonator. With the addition of this path, some equations we derived in Sec. 2.1.5 change to include terms that take the additional components into account.

For the driving voltage (V_d) and output voltage (V_out) we now include the additional current I_p flowing through the parasitic path.

$$V_\mathrm{d} = Z_0(I_1 + I_\mathrm{p}) + V_\mathrm{x} \tag{2.61}$$

$$V_\mathrm{out} = Z_0(I_3 + I_\mathrm{p}). \tag{2.62}$$

In the equations for the currents inside the resonators, we also have to take the current in the parasitic path into account as it can induce a current in the resonator.

$$I_1 = (i\omega_d C_1 + \frac{1}{R_1} + \frac{1}{i\omega_d L_1})V_1 - k_{\mathrm{L},1}\frac{\sqrt{L_1 L_\mathrm{p}}}{L_1} I_\mathrm{p} - I_2 \tag{2.63}$$

$$I_2 = (i\omega_d C_2 + \frac{1}{R_2} + \frac{1}{i\omega_d L_2})V_2 - k_{\mathrm{L},2}\frac{\sqrt{L_2 L_\mathrm{p}}}{L_2} I_\mathrm{p} - I_3. \tag{2.64}$$

Here, k_n is the inductive coupling strength of resonator n = 1,2 to the parasitic path. L_p, C_p and R_p are the inductance, capacitance and resistance of the parasitic path. An

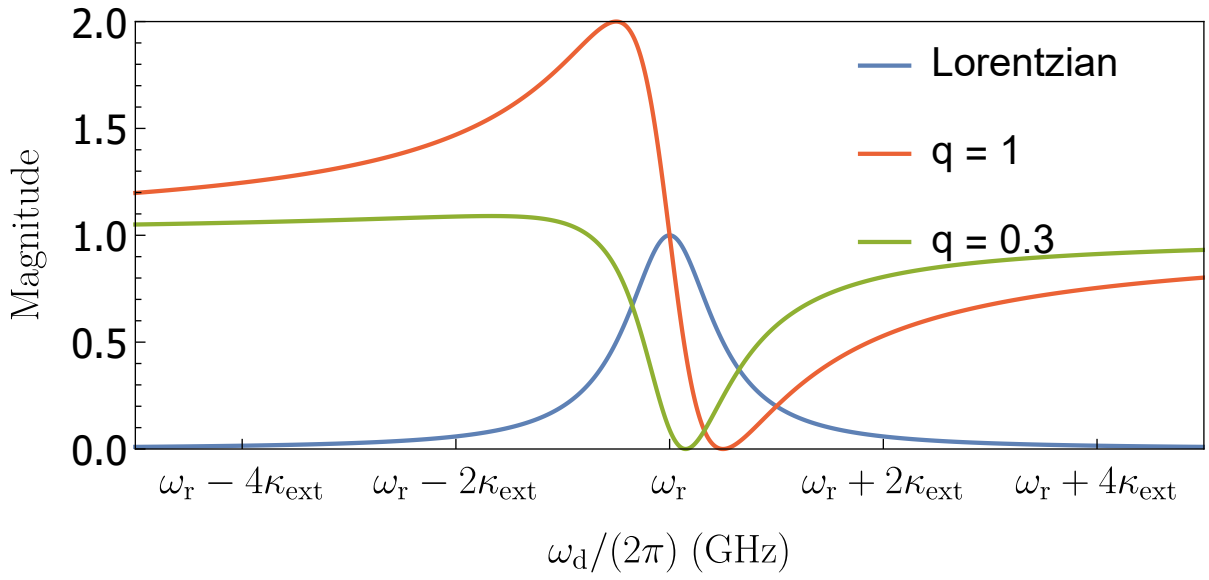

Figure 2.11: Unnormalized transmission magnitude through a resonator with a lorentzian (blue) or fano (red and green) line shape. While the lorentzian shape is perfectly symmetric, the fano resonance shows a strong asymmetry.

additional equation describes the voltage drops inside the parasitic path:

$$\begin{aligned}\frac{1}{i\omega_d C_\mathrm{p}} I_\mathrm{p} - i\omega_d k_{\mathrm{L},1}\sqrt{L_1 L_\mathrm{p}}\frac{V_1}{i\omega_d L_1} + i\omega_d k_{\mathrm{L},2}\sqrt{L_2 L_\mathrm{p}}\frac{V_2}{i\omega_d L_2} \\ + i\omega_d L_\mathrm{p} I_\mathrm{p} + R_\mathrm{p} I_\mathrm{p} + \frac{1}{i\omega_d C_\mathrm{p}} I_\mathrm{p} = V_\mathrm{x} - V_\mathrm{out}.\end{aligned} \tag{2.65}$$

The S-parameters calculated with the parasitic-path model can also be used in Sec. 5.1. In general, the simulations of the model show that the additional path in our system creates a broad resonance mode which is far detuned from the drive frequency ω_d and acts as a continuum at the resonance frequencies of the two resonators. This behavior can also be described by a Fano resonance, which we will discuss in the next part in more detail.

2.1.8 Fano resonances

If a singular resonance mode is coupled to a continuum of modes, the line shape of the resonance can be changed [55]. This change occurs due to an interference effect, as near the resonance of the single mode, the phase of the resonance signal quickly changes (see Sec. 2.1.3) while the phase of the continuum stays constant. This situation gives rise to asymmetric peaks, which are commonly known as Fano resonances. In contrast to a single

mode resonance, which can be modelled with a lorentzian line shape

$$L = \frac{(\frac{\kappa}{2})^2}{(f_0 - f)^2 + (\frac{\kappa}{2})^2}, \tag{2.66}$$

a Fano resonance is modeled by

$$F = \frac{((f_0 - f) + q\frac{\kappa}{2})^2}{(f_0 - f)^2 + (\frac{\kappa}{2})^2}. \tag{2.67}$$

Here, q is the fano parameter which indicates the participation ratio of the single mode versus the continuum. Vanishing participation of the continuum ($q \to \infty$) transforms Eq. (2.67) into Eq.(2.66). In Fig. 2.11 we plot the two different models. We can see that the Lorentzian (blue) gives a symmetric peak as shown in Sec. 2.1.3. For the Fano resonance, we observe a finite field while the signal is far detuned from the resonance, due to the continuum background. Otherwise, the line shape drastically depends on q. For $q \geq 1$, we observe a clear peak-dip structure, where the peak increases in size with increasing participation of the single resonance (increasing q). For $q < 1$, the peak decreases in size compared to the dip. At $q = 0.3$, the peak is almost invisible. For $q = 0$, the asymmetry vanishes and one obtains a symmetric dip.

The take home message here is that, depending on the nature of the background field, the shape of a resonance can vary from a dip to a peak or a peak-dip feature. This is especially important, if a background field is not constant in frequency and the resonance frequency can be tuned, like in the case of a resonator that is intersected by a DC-SQUID. When tuning the resonance through the background field, the line shape of the resonance can change in addition to the resonance frequency.

2.1.9 Nonlinearity

So far, we have neglected the nonlinear terms in our calculations of the circuit. We can take them into account by looking again at the full Lagrangian of one resonator,

$$\mathcal{L} = \mathcal{L}_\mathrm{r} + \mathcal{L}_j. \tag{2.68}$$

Using the Euler-Lagrange equation and expanding the cosine term in $\mathcal{L}_j$, we can calculate the equation of motion of the nonlinear resonator and end up with a Duffing equation, describing a harmonic oscillator with a cubic restoring force,

$$\frac{\Psi}{L'} + C'\ddot{\Psi} + \frac{\dot{\Psi}}{R} + \beta\Psi^3 = 0. \tag{2.69}$$

Here β is the prefactor of the next higher order terms in the Lagrangian of the Josephson junction. β is therefore a direct measure for the nonlinearity of the system and can be

written as

$$\beta = \frac{1}{24}\left(\frac{2\pi}{\Phi_0}\right)^2 \frac{\Delta u^4}{L_j}. \tag{2.70}$$

As we typically work with driven systems, we finally add a driving term with a frequency ω_d and obtain

$$\frac{\Psi}{L'} + C'\ddot{\Psi} + \frac{\dot{\Psi}}{R} + \beta\Psi^3 = F_0 e^{i\omega_\mathrm{d} t}. \tag{2.71}$$

Frequency response equation

In order to calculate the behavior of a Duffing system, and especially the amplitude $a = |\Psi|$, we use an ansatz for small driving strength and small deviations around the resonance frequency [56],

$$\Psi(t) = Ae^{i\omega_0 t} + A^* e^{-i\omega_0 t}, \text{ with} \tag{2.72}$$

$$A = \frac{1}{2}ae^{ib}. \tag{2.73}$$

We then find an implicit function for a, which depends on the driving strength and the nonlinearity of the system,

$$\left[\frac{1}{4R^2} + \left((\omega - \omega_0)C' - \frac{3}{8}\frac{\beta}{\omega_0}a^2\right)^2\right] a^2 = \left(\frac{F_0}{2\omega_0 C'}\right)^2. \tag{2.74}$$

This function is called the frequency response equation. We can plot its behavior in a frequency response curve by solving the equation either for a or for $\omega - \omega_0$. The second approach leads to an expression for frequency detunings as a function of the amplitude a,

$$\omega - \omega_0 = \frac{3}{8}\frac{\alpha}{\omega_0 C'}a^2 \pm \left[\left(\frac{F_0}{2\omega_0 C' a}\right)^2 - \frac{1}{4R^2 C'^2}\right]^{-1/2}. \tag{2.75}$$

A plot can be seen in Fig. 2.12. Comparing this response to one of a linear resonator (Fig. 2.2), we can see that the line shapes are similar for low driving strengths. For higher driving powers, we can see that the maximal amplitude of the resonator increases and the frequency of maximal amplitude decreases. We will discuss this point of maximal amplitude in the next section. Higher driving strength also create regions with three possible amplitude solutions per drive frequency. Note that, while the upper and lower branches of these regions are stable, the intermediate solution is unstable and cannot be observed in experiments. Performing frequency sweeps on a system like this will lead to a hysteretic behavior. Starting from frequencies lower than the resonance frequency leads to the system staying in the lower amplitude branch until the end of the bistability region, where it will jump to the higher amplitude branch. Similarly, starting from higher

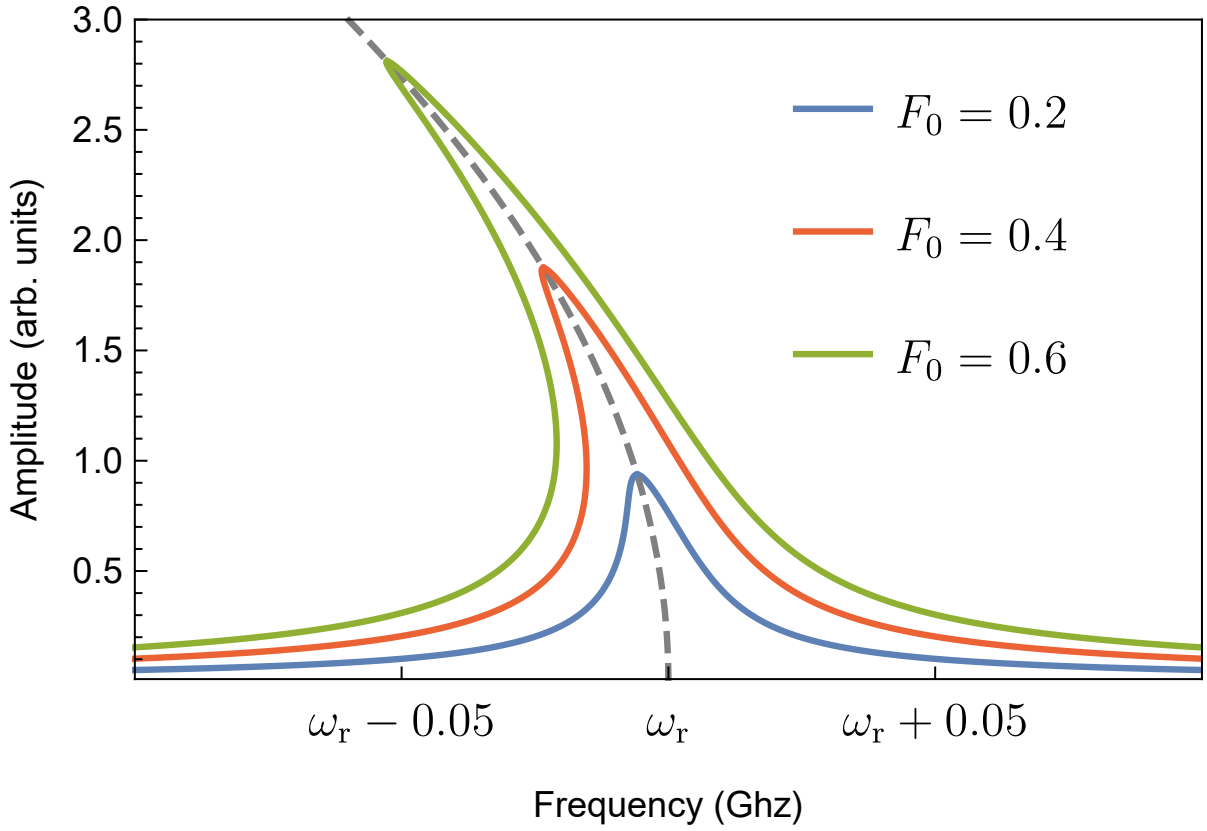

Figure 2.12: Frequency response curve of a Duffing oscillator calculated with Eq. (2.74). Driving the oscillator with higher power F_0 shifts the resonance frequency to lower values. The points of maximum frequency form a parabola (gray dashed line).

frequencies will lead to the system staying in the higher amplitude branch. Here, the jump to the lower branch occurs at the point of maximal amplitude.

Estimating the nonlinearity of the system

For the Duffing-like equation of motion from Eq. (2.71), we can show that the maximum amplitude of the resonance peak is proportional to the inverse nonlinearity,

$$|\Psi|^2 = a^2 = \frac{8}{3}\frac{\omega_0 C'}{\beta}(\omega - \omega_0)\,. \tag{2.76}$$

In an experiment, we measure the voltage V_{ext} emitted from the resonator into its microwave feedline. Therefore, we use $\Psi = \int V \mathrm{d}t = V/(i\omega)$ to rewrite this equation as

$$\frac{V^2}{\omega^2} = \frac{8}{3}\frac{\omega_0 C'}{\beta}(\omega - \omega_0)\,. \tag{2.77}$$

Here, V is the voltage of the internal mode. It is related to the measured voltage via the external quality factor

$$Q_{\mathrm{ext}} = \omega \frac{W_{\mathrm{m}} + W_{\mathrm{e}}}{P_{\mathrm{loss}}} = \omega \frac{|V_{\mathrm{int}}|^2 / (2L\omega^2)}{|V_{\mathrm{ext}}|^2 / Z_0}. \tag{2.78}$$

We use that, on resonance, the energy stored in the capacitor is equal to the one stored in the inductance, $W_{\mathrm{m}} = W_{\mathrm{e}}$. Furthermore, the power of an electrical signal in our waveguide can be written as $P = V^2/Z_0$. We therefore obtain

$$\frac{V_{\mathrm{int}}^2}{\omega^2} = \frac{2V_{\mathrm{out}}^2 Q_{\mathrm{ext}} L}{Z_0 \omega}. \tag{2.79}$$

As a consequence the experimentally accessible voltage V_{out} exhibits a similar dependence as for the internal flux field, but with an additional scaling factor:

$$V_{\mathrm{out}}^2 = \frac{8}{3} \frac{\omega_0 C'}{\beta} (\omega_0 - \omega) \frac{Z_0 \omega}{2Q_{\mathrm{ext}} L} G. \tag{2.80}$$

In this equation, G is the power gain in our experiment (see experimental setup in Sec. 4.2.2).

2.2 Bosonic quantum manybody systems

The platform of superconducting quantum circuit allows us to experimentally investigate the solutions for interacting manybody systems. In the Bose-Hubbard system, the interacting particles are bosons. They experience a periodic potential, where they can hop between lattice sites and interact with each other. The competition between hopping and on-site interaction gives rise to interesting phenomena such as a Mott insulator state and superfluid phase. In this section, we motivate the derivation of the Bose-Hubbard Hamiltonian and explain its properties for some special cases. Furthermore, we discuss the implementation of Bose-Hubbard physics with superconducting circuits.

2.2.1 The Bose-Hubbard Hamiltonian

For the derivation of the Bose-Hubbard Hamiltonian, we assume a periodic potential $V(x)$ with distance r between each potential well of the form of,

$$V(x) = \eta \sin^2(kx), \tag{2.81}$$

with k being the wave vector of the periodicity and η the depth of the lattice. This potential can be estimated to be parabolic near the position x_i of lattice site i,

$$V(x \approx x_i) = \frac{1}{2} m\omega_r^2 (x - ir)^2. \tag{2.82}$$

Solutions for particles in such a periodic lattice are Wannier functions

$$w(x - x_i)^{(n)} = \frac{1}{\sqrt{N}} \sum_k u_k^{(n)}(x - ir) e^{ik(x - x_i)}. \tag{2.83}$$

Here, N is the number of lattice sites and $u_k(x)$ is a periodic function showing the same periodicity as the underlying potential V. Wannier functions are localized at the lattice sites and decay exponentially away from them. The deeper the potential, the quicker the functions decay. Assuming a deep potential, we can apply the tight binding model, where, due to the the fast exponential decay, interactions beyond the nearest neighbor can be neglected. We also assume that all particles stay in the lowest band solution $n = 1$ of the Wannier functions. This is valid, as we operate our experiments at very low temperatures. The thermal energy of our particles is therefore much lower than the excitation energy to a higher Wannier mode.

We can then write the field operator of the bosons inside our lattice as a sum of Wannier functions over all lattice sites,

$$\Psi_\mathrm{B} = \sum_i \hat{a}_i w(x - ir). \tag{2.84}$$

Here, a_i denotes the bosonic annihilation operator and $w(x)$ is the Wannier function for $n = 1$. Using this operator, we can then easily derive its Hamiltonian as

$$\hat{H} = \int \mathrm{d}z \; \Psi_\mathrm{B}^\dagger(z) \left[-\frac{\hbar^2}{2m_\mathrm{B}} \Delta + V(z) \right] \Psi_\mathrm{B}(z). \tag{2.85}$$

Using the Wannier ansatz (Eq. 2.84), we find

$$\begin{aligned} \hat{H}_\mathrm{potential} = &\sum_i \hat{a}_i^\dagger \hat{a}_i \int \mathrm{d}z \; w^*(z) \left[-\frac{\hbar^2}{2m_\mathrm{B}} \Delta + V(z) \right] w(z) \\ &+ \sum_{\langle \mathrm{i,j} \rangle} (\hat{a}_i^\dagger \hat{a}_j + \hat{a}_j^\dagger \hat{a}_i) \int \mathrm{d}z \; w^*(z + r) \left[-\frac{\hbar^2}{2m_\mathrm{B}} \Delta + V(z) \right] w(z), \end{aligned} \tag{2.86}$$

where $\langle$i,j$\rangle$ denote all pairs neighboring lattice sites. The first term is equal to the Hamiltonian of a harmonic oscillator with the excitation energy

$$\hbar\omega_r = \int \mathrm{d}z \; w^*(z) \left[-\frac{\hbar^2}{2m_\mathrm{B}} \Delta + V(z) \right] w(z). \tag{2.87}$$

The second term describes hopping between neighboring lattice sites with the coupling rate

$$\hbar J = -\int \mathrm{d}z\; w^*(z+r)\left[-\frac{\hbar^2}{2m_\mathrm{B}}\Delta + V(z)\right] w(z). \tag{2.88}$$

So far, we only discussed the Hamiltonian based on the the structure of the underlying lattice, and neglected any forms of interaction between the particles. We assume a localized interaction of the form of $V(x-x') = g\delta(x-x')$.

The Hamiltonian of this interaction can be written as

$$\begin{aligned}\hat{H}_\mathrm{interaction} &= \frac{g}{2}\int \Psi_\mathrm{B}^\dagger(z)\Psi_\mathrm{B}^\dagger(z)\Psi_\mathrm{B}(z)\Psi_\mathrm{B}(z) \\ &= \frac{g}{2}\sum_i \hat{a}_i^\dagger\hat{a}_i^\dagger\hat{a}_i\hat{a}_i \int \mathrm{d}z\; w^*(z)w^*(z)w(z)w(z).\end{aligned} \tag{2.89}$$

Here we define the on-site nonlinearity as

$$\hbar U = g\int \mathrm{d}z\; w^*(z)w^*(z)w(z)w(z). \tag{2.90}$$

The total Hamiltonian of the system is then given by

$$\hat{H}_\mathrm{BH} = \hbar\omega_r\hat{a}_i^\dagger\hat{a}_i - \hbar J\sum_{\langle \mathrm{i,j}\rangle}(\hat{a}_\mathrm{i}^\dagger\hat{a}_j + \hat{a}_j^\dagger\hat{a}_i) + \frac{\hbar U}{2}\sum_i \hat{a}_i^\dagger\hat{a}_i^\dagger\hat{a}_i\hat{a}_i, \tag{2.91}$$

which is known as the Bose-Hubbard Hamiltonian.

2.2.2 Phases of a Bose-Hubbard system

The physics in a Bose-Hubbard system are governed by two drastically different phases. The phases arise from the competition between the hopping term J and the on-site nonlinearity U. If $U \gg J$, adding an additional particle to one site requires the energy given by the nonlinearity. Therefore the number of particles in the system is constant and the ground state is given by a state with the same number of particles in each lattice side

$$|\Psi_\mathrm{MI}\rangle \sim \sum_i \left(\hat{a}_i^\dagger\right)^\mathrm{n}|0\rangle\,. \tag{2.92}$$

This state is called a Mott insulator. Hopping between lattice sites does not occur, as the energy cost of adding a (n+1)th particle on lattice site i ($\sim (2n+1)U/2$) is larger than the energy gain of removing the nth particle on lattice site i$\pm$1 ($\sim (-2n+1)U/2$), leading to an energy difference of U compared to the ground state shown above.

If, on the other hand, the coupling is the dominating energy scale in the system ($J \gg U$), the behavior changes drastically towards a superfluid phase. Here, the state can be written

as

$$|\Psi_{\mathrm{SF}}\rangle \sim \left(\sum_i \hat{a}_i^\dagger\right)^{\mathrm{n}} |0\rangle\,. \tag{2.93}$$

Here there is no energy difference created by hopping between sites, meaning that particles can move freely through the lattice.

2.2.3 Particle numbers and driving

In the theoretical description of the Bose-Hubbard system, the number of particles in the system is of great interest and depends on the chemical potential

$$\mu = \frac{\partial E}{\partial N}. \tag{2.94}$$

In cold atom experiments, the particle number is typically fixed by the number of atoms during initialization of the system. Working with superconducting circuits allows us to quickly change and adjust the number of particles using microwave drives. We can model the drive by adding the additional term

$$\hat{H}_{\mathrm{driving}} = \sum_i (\Omega_i e^{-i\omega_{\mathrm{d}} t}\hat{a}_i^\dagger + \Omega_i^* e^{i\omega_{\mathrm{d}} t}\hat{a}_i^\dagger) \tag{2.95}$$

to the Hamiltonian of the undriven system [Eq. (2.91)]. Here, we drive lattice site i with frequency ω_{d} and amplitude or Rabi frequency Ω_i.

The behavior of this driven system does not directly depend on absolute frequencies, but rather on the detuning between them. This effect is best illustrated by moving into a frame rotating with the drive frequency ω_{d}. Mathematically, this transformation corresponds to the unitary operator

$$\hat{U}_{\mathrm{rot}} = e^{i\omega_{\mathrm{d}} t \sum_i \hat{a}_i^\dagger \hat{a}_i}. \tag{2.96}$$

The unitary transformation of the time-dependent driving Hamiltonian $\hat{H}_{\mathrm{driving}}$ is given by

$$\hat{H}'_{\mathrm{driving}} = \hat{U}\hat{H}_{\mathrm{driving}}\hat{U}^\dagger + i\hbar\dot{\hat{U}}\hat{U}^\dagger. \tag{2.97}$$

Note that this transformation does not change parts of the Hamiltonian with higher order dependence on $\hat{a}$, such as the coupling term $\hat{H}_{\mathrm{coupling}} \sim \hat{a}^\dagger\hat{a}$. The transformation of $\hat{H}_{\mathrm{driving}}$ to

$$\hat{H}'_{\mathrm{driving}} = \sum_i (\Omega_i\hat{a}_i^\dagger + \Omega_i^*\hat{a}_i^\dagger) - \hbar\omega_{\mathrm{d}}\sum_i \hat{a}_i^\dagger\hat{a}_i \tag{2.98}$$

We can combine the second part of the driving Hamiltonian with the harmonic oscillator

Hamiltonian, which leaves us with the driven Bose-Hubbard Hamiltonian

$$\begin{aligned}\hat{H}_{\mathrm{BH}} = \hbar\Delta \sum_i \hat{a}_i^\dagger \hat{a}_i - \hbar J \sum_{\langle \mathrm{i,j} \rangle} (\hat{a}_i^\dagger \hat{a}_j + \hat{a}_j^\dagger \hat{a}_i) \\ + \frac{\hbar U}{2} \sum_i \hat{a}_i^\dagger \hat{a}_i^\dagger \hat{a}_i \hat{a}_i + \sum_i (\Omega_i \hat{a}_i^\dagger + \Omega_i^* \hat{a}_i^\dagger).\end{aligned} \tag{2.99}$$

Here, $\Delta = \omega_\mathrm{r} - \omega_\mathrm{d}$ is the detuning between the drive tone and the resonator frequency.

If we compare Eq. (2.99) to Eq. (2.58), we see that they model the same physics. The difference between the two is the missing driving in Eq. (2.58), which can be easily realized by adding microwave drive tones at the resonator inputs. The potential of the Bose Hubbard system is here given by the superconducting resonators. The photons exciting the resonator are the bosons that populate the potential. The hopping between the potential well with amplitude J is realized by the capacitive coupling between single resonators. The on-site interaction U is created by the addition of the DC-SQUID, that is galvanically coupled to the middle of the resonator.

2.2.4 Lindblad master equation

When studying the driven Hamiltonian, we also have to include losses. In the case of a superconducting circuit, these losses stem from either the coupling capacitors (external) or from coupling to other environments (internal, see also Sec. 2.1.3). Typical internal losses are, e.g., losses to the dielectric material. We include the effect of these losses using a Lindblad master equation approach [57],

$$\frac{\mathrm{d}}{\mathrm{d}t}\hat{\rho}(t) = \mathcal{L}\hat{\rho}(t). \tag{2.100}$$

This equation is valid as long as a loss process is described as a Markov process. In the quantum description discussed here, the classical probability distribution $p_t(x)$ is replaced by the density matrix $\hat{\rho}(t)$. Its solution are defined by a linear map $\mathcal{L}$, which can be written according to Lindblad [58] as

$$\mathcal{L}\hat{\rho}(t) = -\frac{i}{\hbar}\left[\hat{H},\hat{\rho}\right] + \sum_i \frac{\gamma_i}{2}\left(2\hat{a}_i\hat{\rho}\hat{a}_i^\dagger - \hat{a}_i\hat{a}_i^\dagger\hat{\rho} - \hat{a}_i^\dagger\hat{a}_i\hat{\rho}\right). \tag{2.101}$$

Here, γ_i is the loss rate of a specific process at the lattice site i. $\mathcal{L}$ is often referred to as a superoperator, i.e. an operator acting on operators.

2.2.5 States and operators of the Bose-Hubbard system

We assume that the bosonic states on each lattice site can be written as a linear combination of d Fock states,

$$|\Psi\rangle = \sum_{\mathrm{n}=1}^{d} c_{\mathrm{n}} |\mathrm{n}\rangle \,. \tag{2.102}$$

The finite dimension d is introduced in order to reduce processing time in calculations. This approximation is valid if the driving strengths are low compared to the loss rates. For high drive powers, higher Fock states are also populated. It is therefore necessary to investigate the population of different Fock states during simulations in order to check the validity of the approximation.

For pure quantum states, we can then formulate the density matrix as

$$\hat{\rho} = \sum_{\mathrm{n,m}=1}^{d} \rho_{\mathrm{nm}} |\mathrm{n}\rangle \langle \mathrm{m}| \,, \tag{2.103}$$

with $\rho_{\mathrm{nm}} = \langle n| \hat{\rho} |m\rangle$ [59]. Additionally, we can write the Fock state $|\mathrm{n}\rangle$ with the photon number limited to $\mathrm{n} < d$ as a d-dimensional vector with only zeros except a 1 at position n. Using this vector form, we can also find an easy representation of the annihilation and creation operators $\hat{a}^\dagger$ and $\hat{a}$. The two fulfill the following equations:

$$\begin{aligned} \hat{a} |\mathrm{n}\rangle &= \sqrt{\mathrm{n}} |\mathrm{n}-1\rangle \\ \hat{a}^\dagger |\mathrm{n}\rangle &= \sqrt{\mathrm{n}+1} |\mathrm{n}+1\rangle \,. \end{aligned} \tag{2.104}$$

Hence, the matrix representation of these operators is

$$\hat{a} = \begin{bmatrix} 0 & 1 & & & & \\ & 0 & \sqrt{2} & & 0 & \\ & & 0 & \sqrt{3} & & \\ & & & \ddots & \ddots & \\ & 0 & & & 0 & \sqrt{d} \\ & & & & & 0 \end{bmatrix} \tag{2.105}$$

$$\hat{a}^\dagger = \begin{bmatrix} 0 & & & & & \\ 1 & 0 & & & & 0 \\ & \sqrt{2} & 0 & & & \\ & & \sqrt{3} & 0 & & \\ & 0 & & \ddots & \ddots & \\ & & & & \sqrt{d} & 0 \end{bmatrix} \tag{2.106}$$

If we adjust the density matrix for a system with two lattice sites which can each hold a superposition of Fock states, we end up with a $d^2 \times d^2$ dimensional density matrix that

represents the whole Hilbert space of the two lattice system.

To find the expectation value of an operator for a system state ρ, we use

$$\left\langle \hat{O} \right\rangle = \mathrm{tr}(\hat{O}\hat{\rho}) \tag{2.107}$$

2.2.6 Steady-state solutions

In a system with competing driving and losses, one expects to find nontrivial steady-state solutions. The steady state is defined by a density matrix which is constant in time,

$$\frac{\mathrm{d}}{\mathrm{d}t}\hat{\rho}(t) = 0, \tag{2.108}$$

leading to

$$-\frac{i}{\hbar}\left[\hat{H},\hat{\rho}\right] + \sum_i \frac{\gamma_i}{2}\left(2\hat{a}_i\hat{\rho}\hat{a}_i^\dagger - \hat{a}_i\hat{a}_i^\dagger\hat{\rho} - \hat{a}_i^\dagger\hat{a}_i\hat{\rho}\right) = 0, \tag{2.109}$$

with the commutator $\left[\hat{H},\hat{\rho}\right] = \hat{H}\hat{\rho} - \hat{\rho}\hat{H}$. One can show [59], that this equation can be written as

$$\left[-i\left(\hat{H}\otimes\hat{I} - \hat{I}\otimes\hat{H}^T\right) + \sum_i \frac{\gamma}{2}\left(2\hat{a}\otimes\hat{a}^* - \hat{a}^\dagger\hat{a}\otimes\hat{I} - \hat{I}\otimes\hat{a}^T\hat{a}^*\right)\right]\hat{\rho} = 0 \tag{2.110}$$

with $\hat{I}$ being the $d^2 \times d^2$ identity matrix and $\otimes$ the tensor product of two matrices. All operators are in a superspace of the two Hilbert spaces of the two resonators. The resulting linear equation can then be solved by standard means.

2.3 Correlation functions

In the simulations of the Bose-Hubbard system, we take special interest in the density-density or second-order correlation functions $g^{(2)}$ of the fields inside the resonators. This correlation describes the likelihood of measuring two photons at the same time. Values larger than 1 signify a higher likelihood than in a coherent field, values smaller than 1 signify a lower one. The second-order correlation function for the field at lattice site i is given by [60]

$$g_i^{(2)}(0) = \frac{\left\langle \hat{a}_i^\dagger\hat{a}_i^\dagger\hat{a}_i\hat{a}_i \right\rangle}{\left\langle \hat{a}_i^\dagger\hat{a}_i \right\rangle^2}. \tag{2.111}$$

$g^{(2)}$ is a good measure for the quantum mechanical nature of a field, as all classical fields exhibit only $g^{(2)}(0)$ values larger than or equal to 1. A coherent field, for example, has $g^{(2)}(0) = 1$, while chaotic fields [60] have $g^{(2)}(0) = 2$. A correlation function of 0 is reached for a single photon. This can easily be seen, if we express $g^{(2)}$ in terms of the photon

number $\hat{n}_i = \hat{a}_i^\dagger \hat{a}_i$

$$g_i^{(2)}(0) = \frac{\langle \hat{n}_i(\hat{n}_i - 1)\rangle}{\langle \hat{n}_i \rangle}. \tag{2.112}$$

We can also look at correlations between the fields at two different lattice sites. These describe then the likelihood of finding an excitations at both lattice sites at the same time. This cross correlation is given as [61]

$$g^{(2X)}(0) = \frac{\left\langle \hat{a}_1^\dagger \hat{a}_2^\dagger \hat{a}_2 \hat{a}_1 \right\rangle}{\left\langle \hat{a}_1^\dagger \hat{a}_1 \right\rangle \left\langle \hat{a}_2^\dagger \hat{a}_2 \right\rangle}. \tag{2.113}$$

Chapter 3

Classical simulations of the Bose-Hubbard model

For few lattice sites and low excitations of the system, it is still possible to perform classical simulations of the Bose-Hubbard model, within a reasonable time span. These simulations allow one to get a deeper understanding of the physics of the system, find a set of parameters, that one wants to look at in an experiment and finally validate results of a possible quantum simulation experiment. Here, we present results of calculations of a Bose-Hubbard system that corresponds in its size (two lattice sites) and the parameter space to the experimental setup we investigate in chapter 5. We take a special interest in the second-order correlation function $g^{(2)}(0)$ of the field inside the resonators and the cross-correlation function $g^{(2X)}(0)$ between the two resonators.

3.1 Implementation

We investigate the behavior of the Bose-Hubbard Hamiltonian for a lattice with two sites. This means that, for calculation purposes, all sums over the lattice sites contract to two summands. In order to perform steady-state calculations, we express Eq. (2.99) in the matrix form presented in Sec. 2.2.5. Note that $\hat{a}$ and $\hat{a}^\dagger$ take slightly more complex forms in order to take all possible states of the two lattice site system into account. The ones given in the previous section, are only valid for the subspace of a single site. Translating them into the combined Hilbert space gives

$$\begin{aligned} \hat{a}_{1,d^2\times d^2} &= \hat{I}^d \otimes \hat{a}_{d\times d} \otimes \hat{I}^1, \\ \hat{a}_{2,d^2\times d^2} &= \hat{I}^1 \otimes \hat{a}_{d\times d} \otimes \hat{I}^d. \end{aligned} \tag{3.1}$$

We solve Eq. (2.110), taking the normalization of the density operator $\mathrm{tr}(\hat{\rho}) = 1$ into account. We then use the solution for the density matrix to calculate the expectation values of operators by means of Eq. (2.107). For example, the expectation value for $\hat{a}$ is given by

$$\langle \hat{a} \rangle = \mathrm{tr}(\hat{\rho}\hat{a}). \tag{3.2}$$

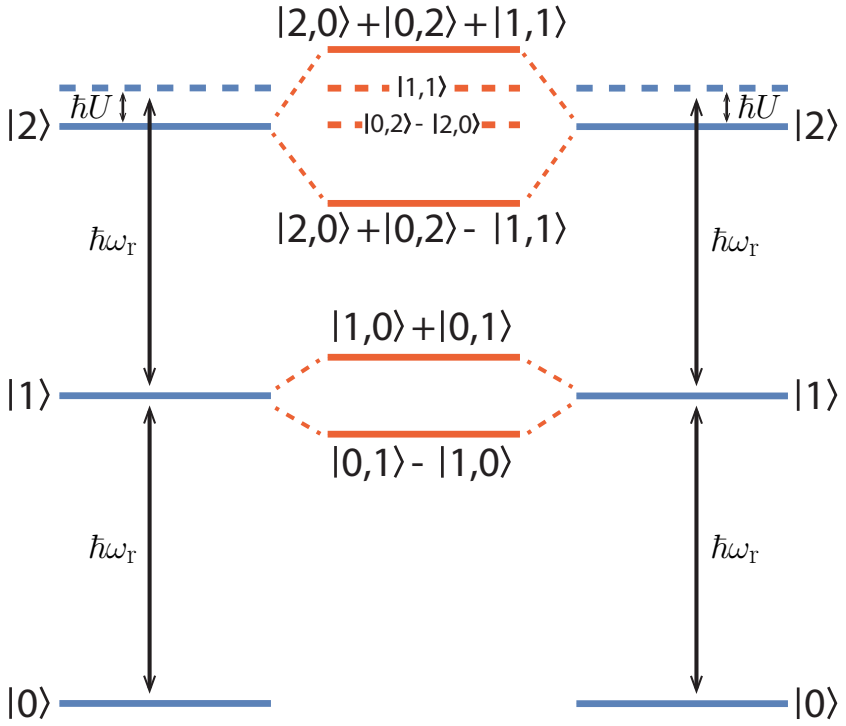

Figure 3.1: Level spectrum of a system of two nonlinear resonators. Levels of the uncoupled system are shown in blue, excited levels of the coupled one in red. Dashed levels are not populated by our protocol. Due to the nonlinearity, higher levels are detuned from the $|0\rangle - |1\rangle$ transition. State descriptions are given without the normalization factor.

This method can be used to calculate the expectation value of the polariton number $\left\langle \hat{a}^\dagger \hat{a} \right\rangle$ on each lattice site and also to calculate correlation functions.

In our calculations, we truncate the Fock basis at $d = 8$. In this way, we significantly reduce the calculation time, but introduce an approximation into the calculation. In order to determine an acceptable compromise between these two competing interests, we perform a detailed study of the Hilbert space truncation on the calculation time and the severity of the approximation [62].

In the simulations, we focus on a parameter space similar to the one of the sample chip studied in chapter 5. We set the coupling rate $J = 7.62\,\mathrm{MHz}$, which corresponds to a value well within the range of the experiment. We vary the nonlinearity from 0 to 10 MHz and the driving strength from 0 to 15 MHz. As we calculate the steady-states of the driven system, the loss rate of the system has to be taken into account as well. We set $\kappa = 1\,\mathrm{MHz}$.

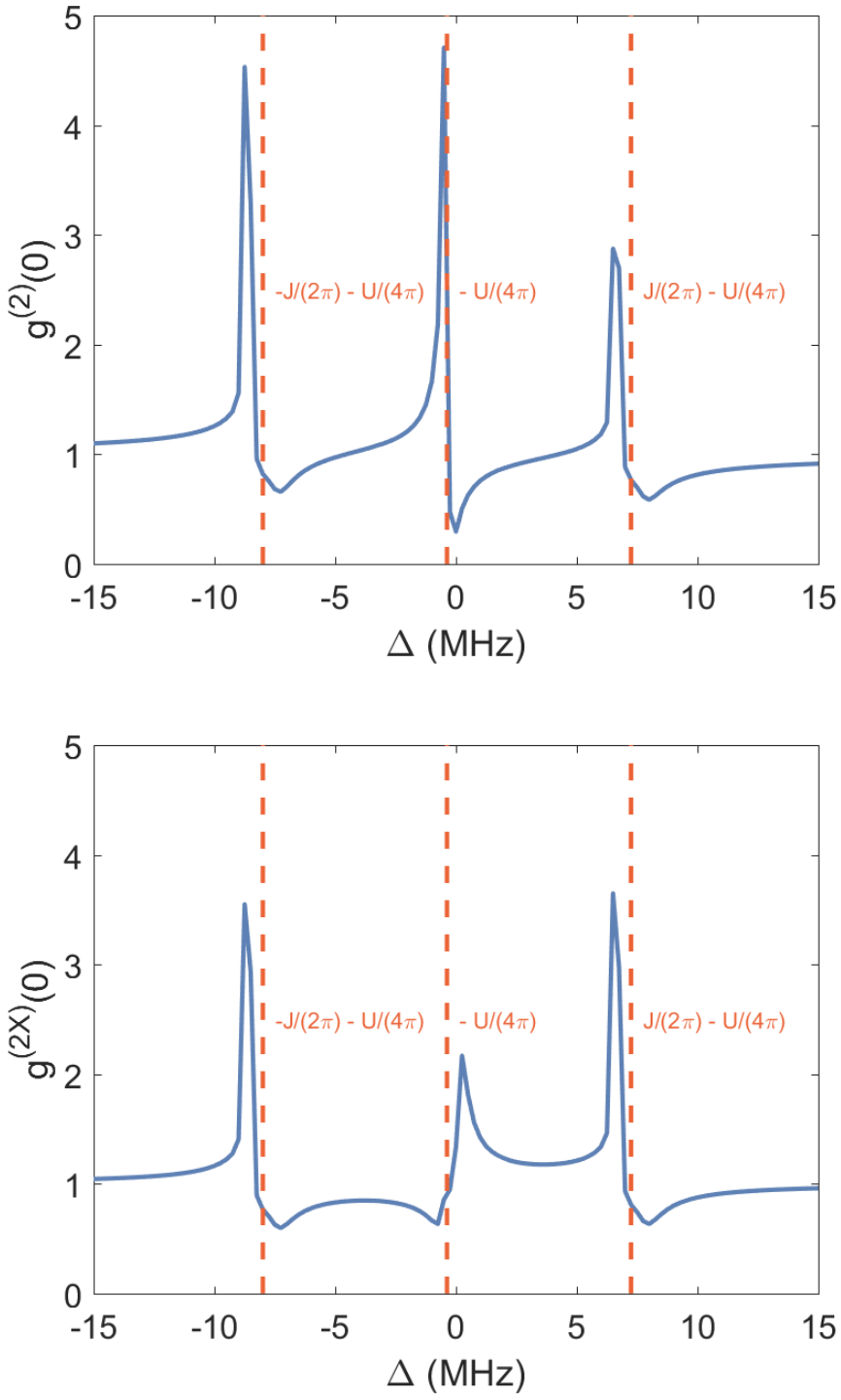

Figure 3.2: Second-order on-site (top) and cross (right) correlation function of a nonlinear two resonator system with fixed nonlinearity $U/2\pi = 0.75\,\mathrm{MHz}$ and driving strength $\Omega = 1\,\mathrm{MHz}$ as a function of the detuning Δ of the drive frequency from the unperturbed single resonator frequency. Red dashed lines show expected drive frequencies for transitions from the ground state to energy levels of the coupled system (see Fig. 3.1).

3.2 Second-order correlation functions

Using the method and parameters described in the previous section, we simulate the second-order correlation functions of the resonators. In Fig. 3.2, we show the results of the correlation functions for a fixed nonlinearity $U/2\pi = 0.75\,\mathrm{MHz}$ and a fixed driving strength $\Omega = 1\,\mathrm{MHz}$. By varying the detuning of the driving signal from the unperturbed frequency of the resonators, and evaluating the correlation functions, we find different regimes for our system. A level scheme can be seen in Fig. 3.1. In summary, we observe that, far away from any transitions, the on-site second order correlation function is governed by the drive and therefore corresponds to the one of a classical driving field $g_2^{(0)}(0) = 1$ while $g_2^{(0)}(0)$ is smaller than 1 near single polariton transitions. On the other hand, near two-polariton transitions, $g_2^{(0)}(0)$ is larger than 1 as it is unlikely to observe single excitations in these regions. Similarly, the second-order cross correlation function $g^{(2X)}(0)$ is close to 1 if the system is detuned from any transition. Near transitions that allow excitations in both resonators, $g^{(2X)}(0)$ is larger than 1, while it is smaller than 1 near transitions that only allow excitations in one of the two resonators.

Details of the on-site correlation functions

We take a closer look at the second-order correlation function of the field in one resonator shown in the top panel of Fig. 3.2. Starting from a detuning of $-15\,\mathrm{MHz}$, the correlation function is close to 1, which corresponds to a classical system. If we increase the signal frequency, we approach the transition from the 0 polariton state to the $|2,0\rangle + |0,2\rangle - |1,1\rangle$ state. This transition is detuned by $J/2\pi - U/2\pi$ from the single resonator energy level with two polaritons. As it is a two-polariton energy level and as there is no single polariton energy level at this frequency, the signal inside the resonator has a correlation function larger than 1. As we can see, the actual peak of the correlation function is below the frequency of the actual transition and at the point of the transition, the correlation function is actually smaller than 1. The reason for this is mainly the power dependence of the resonators. As discussed in Sec. 2.1.9, the resonator frequency is shifted to lower frequencies. In addition, energy levels with higher polariton numbers are even further detuned from the coupled resonance frequency (e.g., the three polariton energy level is detuned by $3U$, the four polariton one by $12U$). Decreasing the detuning further, tunes the signal out of resonance with the $|2,0\rangle + |0,2\rangle - |1,1\rangle$ transition and in resonance with the $|1,0\rangle - |0,1\rangle$ transition. As this energy level is a single polariton one, the correlation function falls below 0, reaching a minimum directly on resonance with the mentioned transition.

This behavior is repeated for two additional drive frequencies, where we can also see a transition from a high correlation function to one below 1. Due to its strong similarity to the previously discussed feature, we will continue with the explanation of the feature that occurs at the highest frequency. The energy spectrum around this frequency contains the

upper energy levels of the coupled resonator states $|1,0\rangle + |0,1\rangle$ for a single polariton energy level and $|2,0\rangle + |0,2\rangle + |1,1\rangle$ for a two-polariton energy level. The two-polariton energy level is shifted towards lower frequencies, by the nonlinearity, detuning this transition from two times the single polariton energy level. If we therefore set the drive signal at a frequency detuning of $J/2\pi$, we are only in resonance with the $|1,0\rangle + |0,1\rangle$, leading to $g_2^{(0)}(0) < 1$. Setting the detuning to a frequency lower than this transition, the drive comes into resonance with two-polariton excitation of the $|2,0\rangle + |0,2\rangle + |1,1\rangle$ transition, leading to a larger correlation function $g_2^{(0)}(0) > 1$. Again, the actual peak is shifted downwards due to the non-zero driving strength.

The third feature, which appears around zero detuning, can also be explained by using the energy level structure of the system. In contrast to the two previous features, the population of the states, that are dominating the physics in this frequency range, is heavily suppressed. This makes it especially difficult to measure the correlation function inside a resonator as almost no signal is leaking out of it. Nevertheless, the simulations show that the correlation functions show a behavior similar to the other features. We observe a correlation function of below 1 for a signal of $\Delta = 0$. Here, the signal is on resonance with both the signal polariton energy level of one resonator and the two-polariton energy level with one polariton in each resonator. Both of these transitions allow only for one polariton in each resonator, which explains the small correlation function. Decreasing the signal frequency, tunes the signal into resonance with the uncoupled two-polariton transition which is shifted by $(U/2\pi)$. As this transition enforces a polariton number $n > 1$, the correlation function is larger than 1.

Details of the cross-correlation functions

In addition to the correlation function describing the polariton statistics inside each resonator, we can also investigate cross-correlations between the polariton fields of the two resonators via the second-order cross-correlation function $g^{(2X)}(0)$. The cross-correlation describes the likelihood of find an excitation in the second resonator if there is an excitation in the first one. Looking at the calculations of this correlation (Fig. 3.2 , bottom panel), we can see, that the Bose-Hubbard system features cross-correlation functions that lie both below and above 1, which indicates a lower or higher probability of finding an excitation in both resonators at the same time compared to a classical coherent field, respectively. Similar to the on-site correlation, we observe three clear features, that correspond to different energies in the excitation spectrum of the coupled system. In comparison with the on-site correlation function we discussed in the previous section, these features in the cross-correlation lie at roughly the same drive frequency, indicating that the underlying effects are related. Similarly, we will now discuss now discuss these in detail. We start again at a detuning of $-15\,\mathrm{MHz}$, where the correlation function is at 1, and increase the drive frequency. As the drive is in resonance with the $|2,0\rangle + |0,2\rangle - |1,1\rangle$ transition that is shifted downwards by the nonlinearity, we observe a peak in the cross-correlation function

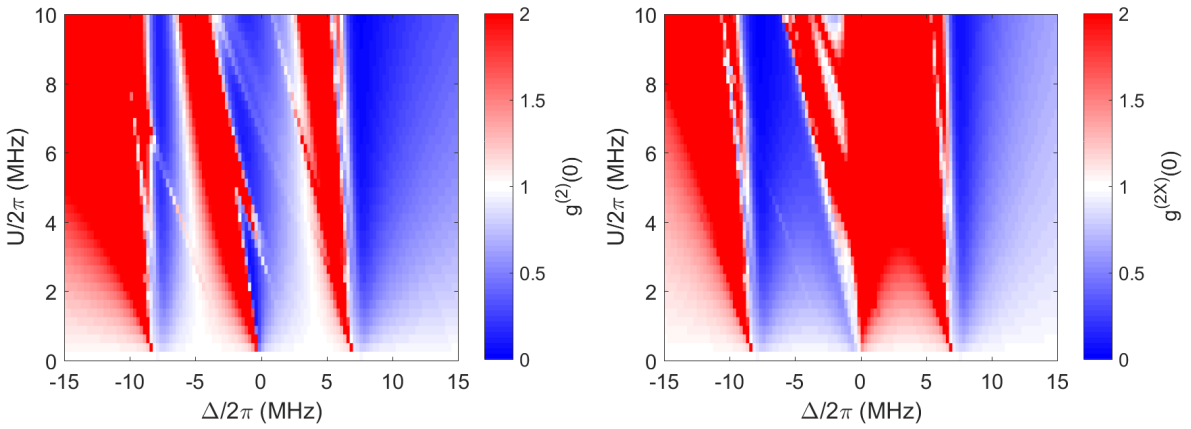

Figure 3.3: On-site (left) and cross (right) correlation function of a nonlinear two-resonator system with fixed driving strength $\Omega = 1\,\mathrm{MHz}$ at one resonator as a function of the detuning Δ of the drive frequency from the unperturbed single resonator frequency and the nonlinearity U. We limit the color scale of the correlation functions to 2, as the values can get quite large, which makes the effects to be less visible as we are mostly interested in whether the correlation functions are below or above 1.

clearly above 1, that created by the contribution of the $|1,1\rangle$ state. Again, the peak is shifted from the actual transition energy, as we apply a non-zero drive tone. Increasing the frequency further tunes the system into resonance with the $|1,0\rangle - |0,1\rangle$ transition, which is unaffected by the nonlinearity of the resonators. Here, the cross-correlation function falls below 1, as the $|1,0\rangle - |0,1\rangle$ state enforced exactly one polariton in only one of the resonators. The second feature, which can be seen near $\Delta = 0$, is flipped in comparison to all previously discussed features. At negative detuning, the system is in resonance with the $|2,0\rangle - |0,2\rangle$ transition, which also only allows polaritons in one of the two resonators. Therefore, the cross-correlation function is below 1 in this region. Tuning the drive into resonance with the unperturbed resonance frequency, we then observe the effect of the $|1,1\rangle$ state, which leads to a cross-correlation function above 1 as it allows only excitations with one polariton in each resonator. The third feature is then analogous to the first one, where the drive is first in resonance with $|2,0\rangle + |0,2\rangle + |1,1\rangle$ which leads to a $g^{(2X)}(0) > 1$. At slightly higher frequencies it is in resonance with $|1,0\rangle - |0,1\rangle$, leading to $g^{(2X)}(0) < 1$.

3.2.1 Correlation functions and nonlinearity

In our experiment, we have the possibility to tune the nonlinearity U in situ. In the previously discussed calculations, a constant nonlinearity of 0.75 MHz has been used. This nonlinearity has a big impact on the correlation functions, as it modifies the energy level structure of the coupled system. In this section, we therefore investigate the effect of the nonlinearity on both the on-site and the cross-correlation function. The results of this

calculation for the fixed driving strength $\Omega = 1\,\mathrm{MHz}$ can be seen in Fig. 3.3. First, we can see that for vanishing nonlinearity, both correlation functions are 1 for all drive frequencies. This shows us that the change in the correlation functions is a purely nonlinear effect. For $U = 0$, energy levels are equidistant and we obtain a coherent behaviour. The case of a small, but nonzero nonliearity has been discussed in the previous sections. If we increase the nonlinearity further, the parts of the on-site correlation function which show $g^2(0) > 1$ move towards lower frequencies and broaden. As the involved modes are shifted by $\hbar U$, the shift is directly affected by the nonlinearity. The broadening can be explained by the Duffing-like behaviour of the resonators. As explained in Sec. 2.1.9, increasing nonlinearity leads to a broader resonance frequency in systems governed by a Duffing-like behaviour. For the two features around the coupled modes, the transition to the region of low on-site correlation functions at $\Delta = \pm 15\,\mathrm{MHz}$ is not changed by the increase in nonlinearity, as the responsible one polariton excitations are unaffected by its change. We can also observe that the larger the nonlinearity, the lower is the value of the correlation function in these regions. Also, the value of the correlation function gets bigger with increasing nonlinearity in regions with $g^{(2)}(0) > 1$. The dependence of the cross-correlation function on the nonlinearity is similar to that of the on-site-correlation function as the underlying transitions behave in the same way.

3.2.2 Correlation functions and driving strength

Another parameter that we investigate numerically is the strength of the drive signal. In an experimental setup, this is easily controlled by increasing the power of the microwave drive. We set the nonlinearity again to 0.75 MHz and calculate the correlation functions for varying driving strength from 1 to 15 MHz. The result of this calculation can be seen in Fig. 3.4. As we have discussed in Sec. 2.1.9, an increase in power leads to a shift of the effective resonance frequency. We can observe this behaviour very clearly both in the on-site and cross-correlation function. In both cases, the features near the two coupled modes are clearly shifted towards lower frequencies with increasing drive power. The feature around zero detuning seems to be unaffected by the driving strength. Naively, we would expect that also this feature is shifted, as the $|2,0\rangle - |0,2\rangle$ state should also be affected by it. In our calculations, this is not visible because the transition is forbidden and therefore the state is not populated due to the coupling of the resonators. As a result, the corresponding transition frequency stays unchanged up to until approximately 12 MHz, where we observe a small trend towards lower frequencies. For higher driving strength, we observe additional resonances that show correlation functions larger than 1. Due to the higher driving, these resonances which are higher-order excitations of the system can be reached and therefore contribute to the overall behaviour of the system. As can be seen in the Hamiltonian, these higher-order excitations are shifted by multiples of the nonlinearity and therefore appear at frequencies just below the one and two-polariton

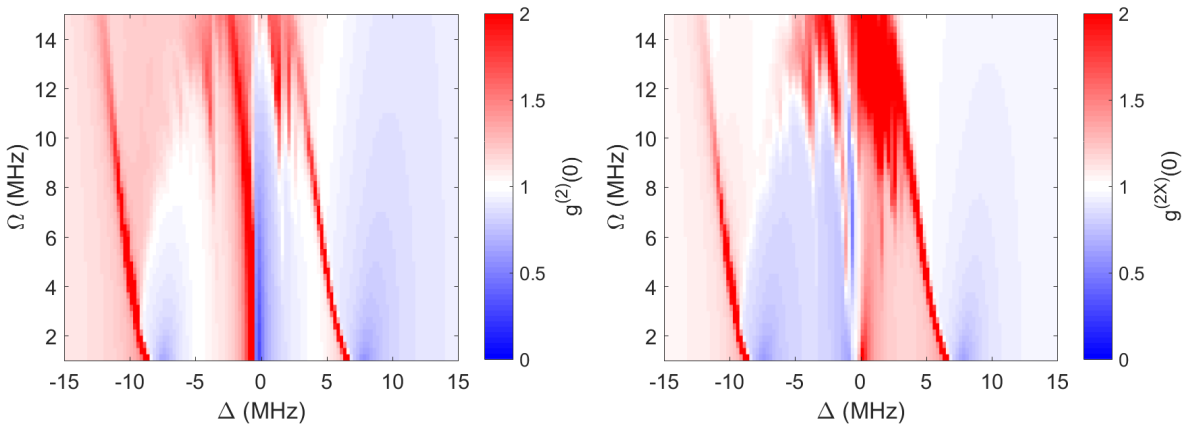

Figure 3.4: On-site (left) and cross (right) correlation function of a nonlinear two resonator system with fixed nonlinearity $U/2\pi = 0.75\,\mathrm{MHz}$ as a function of the detuning Δ of the drive frequency from the unperturbed single resonator frequency and the driving strength Ω.

transitions we previously discussed.

3.2.3 Comparing on-site and cross-correlation functions

If we compare the results for the on-site and cross-correlation functions, we find that there are parameter regions, where the two almost coincide and regions, where they clearly differ from each other. Especially if we compare the two functions to the value of a coherent field, we can distinguish four different regimes. In Fig. 3.5, we plot both correlation functions and mark the four regimes with different background colors. The orange background indicates that both functions have values above 1. The highest values can be observed at the resonance frequency of the coupled resonators, where the two are heavily excited and transmission through the system is possible. Green indicates correlation functions below 1, meaning that if an excitation occurs it is less likely than in a coherent field to find additional excitations either in the same resonators or the adjacent one. In the regime colored with red, the on site correlation is larger than 1 but the cross-correlation is below 1. This means, we are likely to find multiple excitations in one resonator, while the second one is not excited. Lastly, we find a regime, colored in blue, where this relation is turned around. Here, the cross-correlation is larger than 1 and the on-site one is lower. We can visualize this as a state where it is likely to find excitations in both resonators at the same time, but unlikely to find multiple excitations in a single resonator. For a larger lattice this can be viewed as a form of a polariton crystal, where we find a polariton at each lattice site due to the high cross-correlation. For the last three regimes (green, red and blue), the transmission through the system is low as it is suppressed by either correlation function being below 1.

Experimentally, it is therefore vital to build a very sensitive correlation function

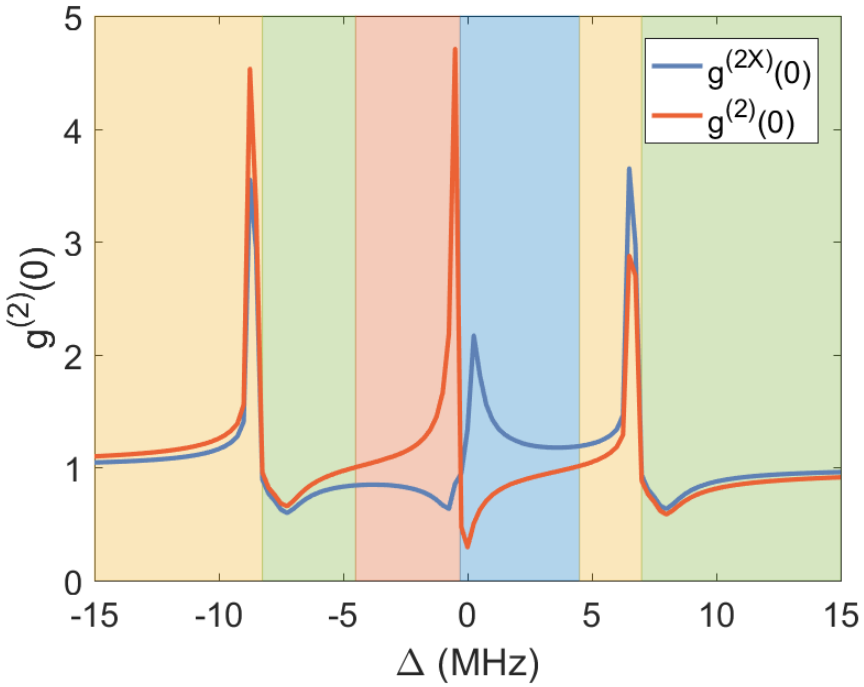

Figure 3.5: On-site (red) and cross (blue) correlation function of a nonlinear two resonator system with fixed nonlinearity $U/2\pi = 0.75\,\mathrm{MHz}$ and fixed driving strength $\Omega = 1\,\mathrm{MHz}$ as a function of the detuning Δ. The colored background indicates regions where both correlation functions are larger than 1 (orange), smaller than 1 (green) or where $g^{(2X)}(0) < 1$ and $g^{(2)}(0) > 1$ (red) and vice versa (blue).

measurement setup. In the following, we present a measurement setup which allows us to measure the correlation functions of such weak signals.

Chapter 4

Sample fabrication and measurement setup

In this section, we focus on the experimental setup. The first part (Sec. 4) shows the sample design of the superconducting circuit we use for the experiments. In the second part (Sec 4.2), we present the different measurement setups used for the experiments done in the scope of this thesis.

4.1 Sample

Here, we show the sample and its fabrication procedure. In Sec. 4.1, the circuit design in general and its design parameters are discussed. Section 4.1.2 describes the fabrication of the sample.

4.1.1 Sample design

The sample is a 525 µm thick silicon chip with superconducting aluminum circuits on top of it. The Josephson junctions are fabricated using double-angle shadow evaporation. The total thickness of the aluminum structure is 140 nm (see sec. 4.1.2). A sketch of the sample and micrographs of different important parts of it can be seen in Fig. 4.1. The circuit consists of two superconducting, serially-connected resonators, which are each intersected by a DC-SQUID.

Resonators

The main part of the superconducting circuit is formed by two capacitively coupled resonators. They are fabricated in the coplanar waveguide (CPW) design. The width of the inner conductor is 13.2 µm and the two gaps between inner and outer conductor are 8 µm each. This results in an impedance of 50 Ω, which is also the impedance of the used cables and electronics. Matching the impedance between all components is helpful to avoid losses and reflections that would occur at impedance mismatches. The resonators

are confined by finger capacitors to form a resonator length of 7420 µm. This length of the resonator sets the unperturbed resonator frequency. The DC-SQUID only tunes the resonance towards lower frequencies, so that the unperturbed frequency sets a theoretical upper limit, that cannot be reached due to the finite Josephson inductance of the SQUID. As we are limited to a measurement window between 4 GHz to 8 GHz by cryogenic circulators, we want to set the resonator length in a way that the maximum resonator frequency is around 8 GHz. From the resonator length, we calculate $f_{\mathrm{res}} = 8.043\,\mathrm{GHz}$. Including the SQUID, which tunes the resonance frequency down, the real maximum resonance frequency will lie inside the measurement window.

Coupling capacitor

The resonators are coupled via a finger capacitor (see Fig. 4.1) with a finger length of 20 µm. Finger capacitors can achieve a higher capacitance and with this higher coupling strength between the resonators as compared to, e.g., gap capacitors. Since we aim for an intermediate capacitance, we only use a single finger. Additional fingers would further increase the size of the capacitor and with this the capacitance. We aim for a coupling strength of $\frac{J}{2\pi} = 10\,\mathrm{MHz}$. To be able to predict the coupling strength of different capacitor designs, we investigate different samples with different capacitor designs [63]. We find that a finger length of 20 µm leads to a frequency splitting of the two resonances in a transmission measurement of 21.1 MHz. The coupling can be calculated from the splitting with $\frac{J}{2\pi} = \frac{\sqrt{(\delta f)^2 - \Delta^2}}{2}$, where J is the couling strength, δf is the frequency splitting and Δ is the detuning of the bare resonator frequencies. We can see, that with a finite detuning of the resonators, the coupling strength is always lower than half the frequency splitting. Due to inaccuracies in fabrication, building resonators with the exact same frequency is almost impossible and detunings of a few MHz are not unusual. With this in mind, we choose the finger length of 20 µm and expect to get a coupling strength of around 10 MHz.

In- and output capacitors

On either side of the resonator dimer, the resonators are capacitively coupled to external feedlines with additional finger capacitors (see Fig. 4.1). There are two main constrains on the design parameters. Firstly, the strength of the signal leaking out of the resonator. For a high-power experiment, where the resonator is populated by thousands of photons, the signal will be easily detectable even with low output coupling. But for measurements with low power, where the average population of the resonator is in the order of one or even less than one photon, it is critical to have high enough output coupling to be able to measure the field inside the resonators. Secondly, we want to get access to the driven dissipative regime, where a driving tone and the losses of the resonator compensate each other to build a steady state. In our theoretical simulations, we find steady state solutions for a loss rate $\kappa = 0.5\,\mathrm{MHz}$. In this simulation with a driving strength of $0\,\mathrm{MHz} \leqslant \Omega \leqslant 20\,\mathrm{MHz}$, we

find an average population of our system of $0.1 \leqslant n \leqslant 3$ in interesting regions. A thorough estimation of the signal strength that we can resolve in our system is very challenging, as we would need to know the exact amplification rates and noise numbers and our exact measurement bandwidth, but as most of the experimental setup was newly set up after the sample design, the best estimation that we can do is to compare it to similar setups. In house, we can achieve resolutions of signal down to $n \leqslant 1$. We conclude, that a bandwidth of 0.5 MHz should satisfy both our design goals. Similar to the coupling capacitor, we use a set of resonators with different output capacitors to obtain the right finger length for our design goals. We choose a finger length of 40 µm which leads to the desired loss rate.

DC-SQUIDs

We place a DC-SQUID near the current maximum of each resonator. The area of the SQUID loop is $A_{\mathrm{SQUID}} = 10.5\,\mu\mathrm{m} \times 24.5\,\mu\mathrm{m}$. This area determines how strong the magnetic field has to be at the SQUID, in order to get a specific amount of flux in the loop. Loop size is always trade off between being able to tune the critical current of the SQUID with little current flowing through the antennas and noise sensitivity of the SQUID. If the SQUID loop is too large, flux noise can easily couple to the SQUID and lead to an unstable or broadened frequency of the resonator. Previous work done at the Walther-Meissner-Institute shows that, with a similar SQUID and antenna design, one can achieve good tunability through on-chip antennas [64]. As we can also tune the resonator frequency via an external coil, which allows for larger magnetic field sweeps, tunability of the flux via the antennas by less then a flux quantum are enough to ensure full control of our resonators. The inner conductor of the resonator shrinks to 750 nm starting at a distance of 19.5 µm from the SQUID. The width of the conductor in the SQUID loop is 550 nm. This loop is interrupted by two Josephson junctions with slightly different dimensions. Junction 1 has an area $A_{\mathrm{JJ1}} = 101.0 \cdot 10^3\,\mathrm{nm}^2$ and junction 2 an area $A_{\mathrm{JJ2}} = 54.4 \cdot 10^3\,\mathrm{nm}^2$. This leads to an asymmetric SQUID, which is described in Sec. 2.1.4. An asymmetric SQUID is advantageous for us, as we are limited to a window between 4 GHz to 8 GHz, and therefore don't have access to low frequency ranges. In addition, a flatter dependence of the frequency on the applied magnetic flux leads to less sensitivity to flux noise. The estimated overlap from the design is 150 nm for both junctions although the actual overlap varies because the fabrication is not one hundred percent exact (see Sec. 4.1.2). With an estimated critical current density $J_{\mathrm{c}} = 150\,\mathrm{A/cm}^2$ this gives design values for the critical current of the two junctions of $I_{\mathrm{c},1} = 151.5\,\mathrm{nA}$ and $I_{\mathrm{c},2} = 81.6\,\mathrm{nA}$ and a total critical current of the SQUID $I_{\mathrm{c}} = 233.1\,\mathrm{nA}$.

Antennas

The on-chip antennas are shorted CPWs [see Fig. 4.1 (e)]. The current flowing through the shorting strips then causes a magnetic field at the SQUID position. These types of

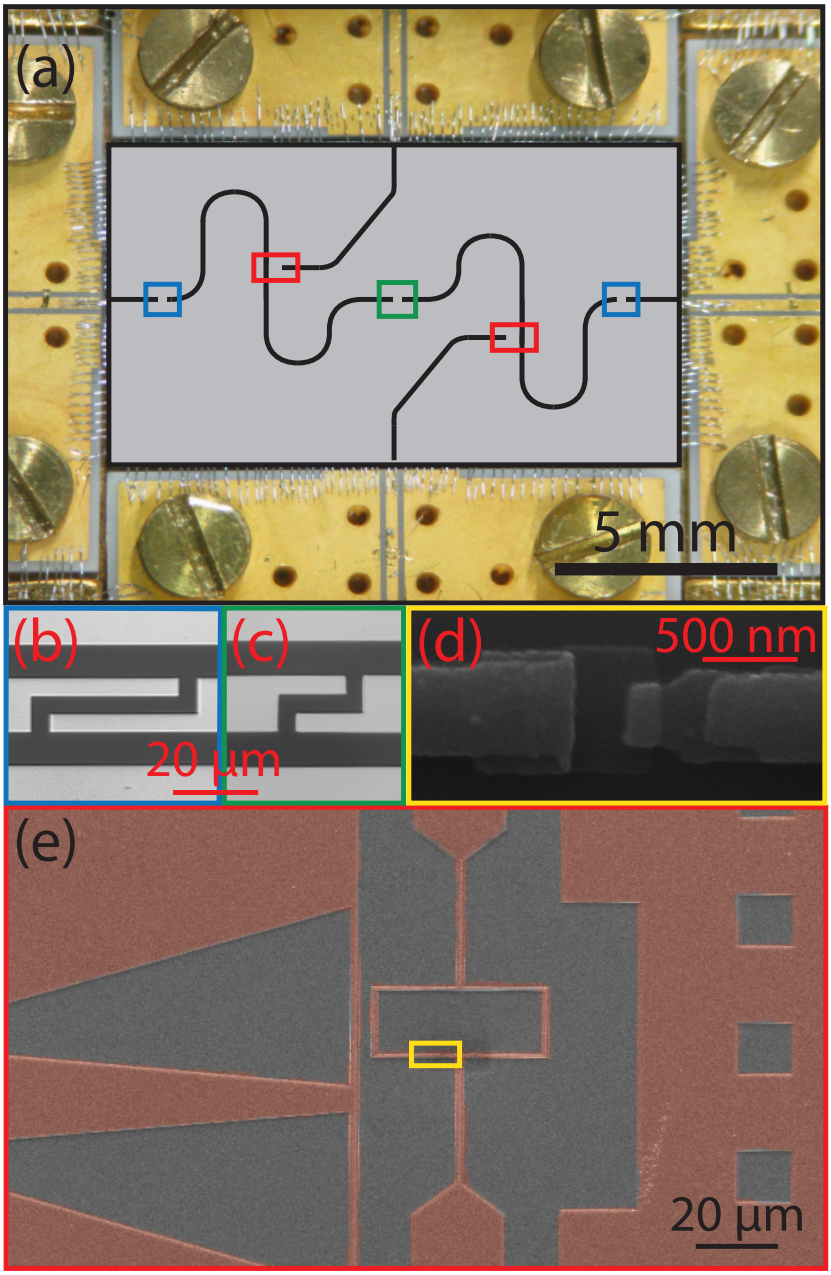

Figure 4.1: (a) Sketch of the two-resonator sample chip (black lines: resonators, feed lines and antennas) mounted into a photograph of the sample holder. The ground planes on both sides of the CPW structures are connected to each other using aluminum bonds. Colored rectangles indicate zoom-in views. (b) 40 µm long finger capacitor to couple the resonator to the external feedline. The width of the inner conductor of the waveguide is 13.2 µm and gaps between inner and outer conductor are 8 µm each. (c) 20 µm finger capacitor connecting the two coplanar waveguide resonators. (d) Zoom-in view showing one of the Josephson junctions of the (e) dc SQUIDs (false color micrograph). The SQUIDs are galvanically coupled to the inner conductor of each resonator at the current antinode. The structure on the left of the SQUID loop is one of the on-chip antennas.

Table 4.1: Brief overview of the fabrication recipe.

Step	Details
Cleaning	Acetone and Isopropanol
Apply Resist	AR-P 617.08 and ARP 679.02
Apply gold particles	Used to focus on the chip with EBL
Writing in EBL	Write whole chip, but specific parts with different doses
Developing	Developer AR-600-56 and Isopropanol
Two angle shadow evaporation	Full chip aluminum evaporation with intermediate oxidation
Cleaning	Remove all resist and aluminum on top of the resist with acetone

antennas create an antisymmetric field distribution, which leads to zero flux inside the loop, if the center of antenna and loop align. Therefore, we place the antenna 12 µm off center. The inner conductor at the end of the antenna is 4 µm long and the strips are 28 µm long and 1 µm wide. The CPW structure used to connect the antennas to the outside has the same dimensions as the resonators.

In- and output lines

The lines connecting the resonators to the external feed lines are also CPWs. They have the same dimensions as the resonators and antennas, only at the edge of the chip, they are broadened with tapers. Here, the width of the inner conductor is 127 µm and the gap is 101 µm wide. The tapering is done over a length of 750 µm, so that the changes in impedance are as smooth as possible. The increase in width is important, as the chip is connected with wire bonds to the surrounding printed circuit board (see Sec. 4.2.1).

4.1.2 Fabrication

In this section, we report on the process we used to fabricate the sample measured in the scope of this thesis. We use an all-aluminum process and fabricate everything in the facilities of the WMI. In the following, we present our recipe and also dive into details on fabrication parameters and important steps that lead to a working sample.

Recipe overview

Here we give an overview over the fabrication recipe. A very brief overview can be seen in Tab. 4.1 and a visualization of the most important steps of the junction fabrication in Fig. 4.2. We start our process with pre-cut high-resistivity ($R > 3\,\mathrm{k\Omega}$) silicon wafers with a thickness of 525 µm. They are not artificially oxidized and therefore only have a thin layer of naturally formed SiO_x on them. The dimensions of the chips are 6 mm × 10 mm.

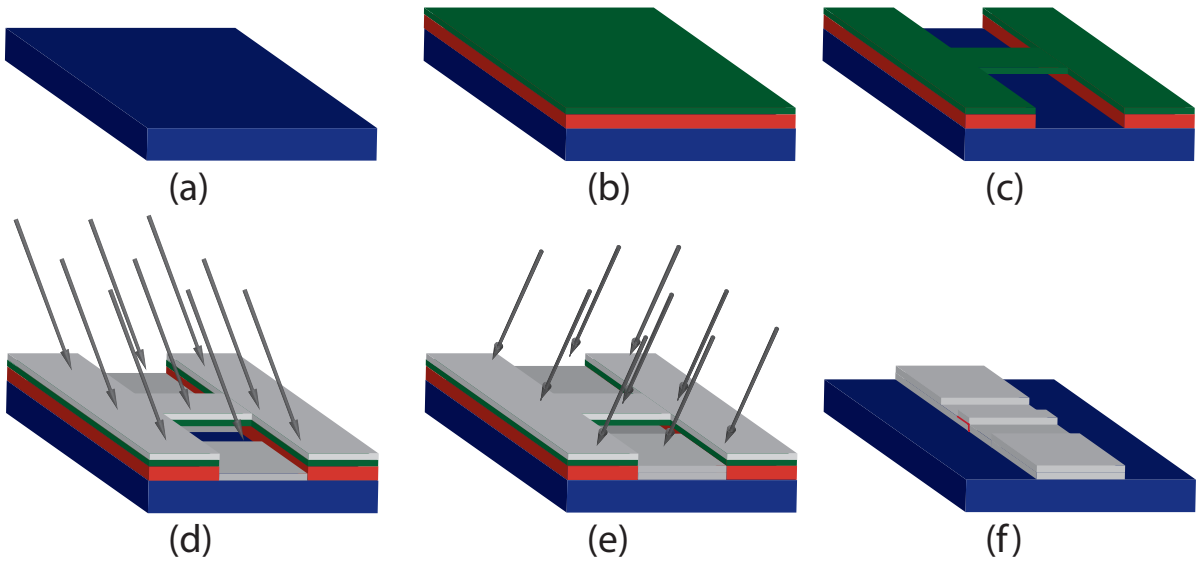

Figure 4.2: Sketch of the sample fabrication. Josephson junctions are fabricated with double-angled shadow evaporation. First, two resist layers are applied to the sample (b), exposed and developed (c). Next, two layers of aluminum are evaporated with an aluminum oxide layer in between (d,e). Finally the resist including the unwanted aluminum is removed (f).

The sample is then cleaned with a standard cleaning process using acetone and isopropanol. This step removes dirt on the chips, a layer of protective varnish and the glue that kept the chip attached to a foil after cutting and during transportation. The chips are put into 70 °C warm acetone for 30 s. Afterwards, the chips are cleaned three times in an ultrasonic bath for 2 min using, in that order, technical acetone, high purity acetone and high purity isopropanol. During these steps, we make sure the chips are never exposed to air. Then, the chips are dried with pressurized nitrogen. In the next step, we apply two resist layers onto the sample [Fig. 4.2(c)]. The bottom resist layer is made from AR-P 617.08 e-beam resist[1]. We start by baking the chip for 5 min at 200 °C on a hotplate. Afterwards, the chip is spin-coated in a nitrogen atmosphere. We use 2000 rpm for 2 min, leading to a layer thickness of approximately 680 nm. Afterwards, the chip is baked at 160 °C for 10 min. We then repeat the spin coating process with the top layer resist PMMA/950K/AR-P 679.02[1]. The layer thickness of this resist when spin coating with 2000 rpm is 100 nm. In order to easily set the focus in the electron beam lithography (EBL) machine, we apply gold particles to the edges of the sample. These particles can be easily found under the microscope of the EBL machine as bright dots. Then, we write the structure of our sample using EBL. We write the whole chip in one step, but vary the dose applied in different parts. We relate all used doses to the highest used dose, which is 7. We use this dose for the metallized parts of the SQUID loop and the conductor leading to the loop. The ground plane and the inner conductors far from the SQUID are written with a dose of

[1]Made by Allresist GmbH

0.66 times the base dose, to reduce the time it takes to write the sample. The edges of the CPW are written with a dose of 0.82 times the base dose to increase sharpness and, on the other hand, to reduce the proximity effect of the big ground planes. Around the junctions, we create an undercut by applying only very little dose (0.2 times the base dose). This amount is too little to fully expose the top resist layer, which means that, after developing, a free-standing bridge of the top resist still remains. This bridge is required to perform shadow evaporation to create the Josephson junctions. Developing is done by putting our samples in the developer AR-600-56[1] for 45 s and afterwards in 4 °C cold isopropanol for 2 min. Doing the second step in cold isopropanol as opposed to room temperature proved to increase the sharpness of the fabricated structures. During development, we constantly move the sample inside the beakers to ensure that fresh developer reaches the resist. To terminate the development process, we wash the chips with clean water twice.

We then perform double-angle shadow evaporation using aluminum. We tilt the sample by $\pm 17°$ and evaporate 40 nm of aluminum in the first step and 70 nm in the second step [see Fig. 4.2(d) and (e)]. In between, we expose the sample to a controlled oxygen environment for 9000 s. From previously fabricated samples, we estimate the critical current density to be $J_c = 150\,\mathrm{A/cm^2}$ for the oxygen layer that is formed in this time span. After evaporating, we perform a lift-off process, where the remaining resist and with it the aluminum on top of it is cleaned away. We do this by putting the samples in a beaker with 70 °C hot acetone for one hour. Every 15 min, we use a pipette to create a strong flow around the sample that helps loosen the resist and aluminum from the sample. To fully remove all unwanted material, we place the sample inside an ultrasonic bath on low power for 1 min. During this whole lift-off process, we never expose the sample to air, as this would lead to particles sticking to the surface.

4.2 Measurement setup

In this part, we describe the measurement setup, used for our experiments. This description includes how we connect our sample in the sample box (see Sec. 4.2.1), the cryogenic setup (see Sec. 4.2.2) and the room temperature setup for different measurements (see Sec. 4.2.3 and Sec. 4.2.4).

4.2.1 Sample box

To connect our sample to the external feed lines, we place it in a gold plated copper box with four ports. The connectors are 2.92 mm (K) connectors. We fabricate the box in our in-house workshop and also solder the connectors ourselves. Inside the box are four printed circuit boards that we use as a link between chip and connectors. They are made of alumina with a gold layer on top. Each PCB has a straight CPW leading from the

[1] Made by Allresist GmbH

chip to the connector. On the connector side, we solder the inner conductor of the PCB to the center pin of the connector. In addition, we use silver glue to connect the outer conductors to the sample holder metal. In this way, we increase the impedance matching between connector and board drastically. On the other side, the chip is connected to the PCBs with aluminum wire bonds. We place five bonds on each inner conductor and around 200 bonds on the outer conductors. In addition, we use bonds to avoid potential differences between the ground planes on the sample. We bond approximately 40 times over the CPW structures in regular intervals. The lid of the sample features four pillar like structures, that should increase the frequency of possible box modes, so that they don't interact with our resonators.

4.2.2 Cryogenic setup

We perform our experiments in a home-made ^{3}He/^{4}He dilution refrigerator with a base temperature of 27 mK. In the following, we briefly outline the working principles of such a cryostat and present the experimental setup inside the fridge.

Thermalization

In Fig. 4.3, one can see a schematic of the experimental components inside the cryostat. From top to bottom, all input and output lines, as well as the DC-wires, pass through the different temperature stages of the refrigerator. At each stage, the wires are thermalized. The temperature stages each feature metal plates, to which cabling can be connected in order to thermalize them. The input lines are each thermalized through attenuators which are fixed to the stages with metal clamps. As attenuators cannot be used in output lines, as they would decrease the already low signal strength, we directly clamp the outer conductor of the output cables to parts of the temperature stage all along the output lines. For this, we use gold-platted copper clamps and annealed silver wire. In addition, the output lines are thermalized at the 30 mK stage and the 600 mK stages through cryogenic circulators, which are directly connected with the plate due to their fixture. The DC-wiring is thermalized by glueing the wire bundles to different parts of the temperature stages for a few centimeters. In addition, the wires are connected to small anchors, where the cables coming from the top are each soldered to a small metal pin and the cables going further down into the cryostat are soldered to the other sides of the metal pins. The anchor itself is directly placed onto the plate of the temperature state.

Microwave input lines

For microwave signals, we use coaxial cables. Starting at room temperature, where the signal generator is connected to the fridge with flexible cables, the input lines feature attenuation at each temperature stage. The attenuation is needed in order to protect the

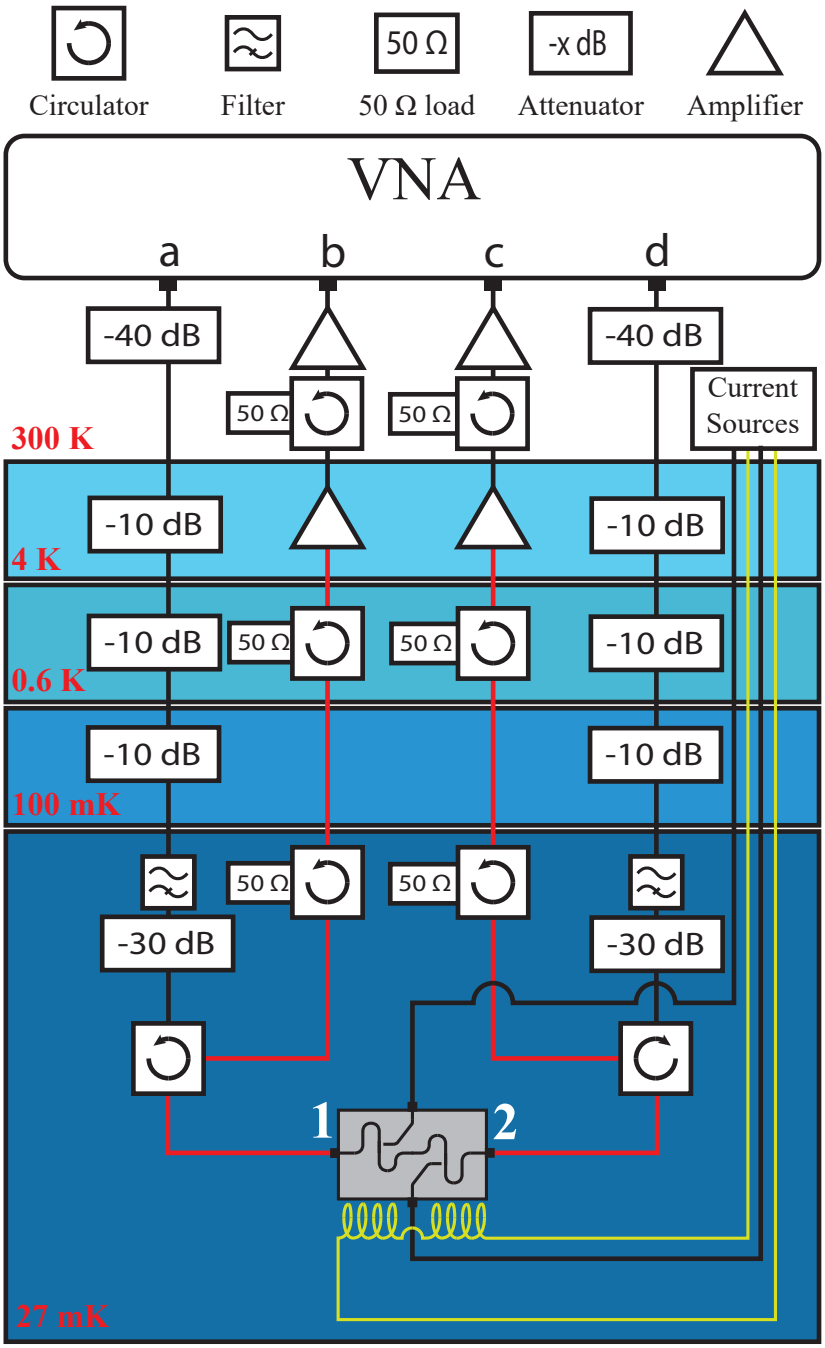

Figure 4.3: Cryogenic setup. We apply a probe signal with a VNA (port a or d) through heavily attenuated input lines. The attenuation is distributed over multiple temperature stages of the cryostat to decrease the heat load on the system and to shield the sample from high-temperature noise. All output lines are made from superconducting niobium-titanium coaxial cables (red). In the output path, cryogenic circulators isolate the sample from high-temperature noise. The output signal is amplified with cryogenic and room temperature high-frequency amplifiers and then detected by the VNA (port b or c). The on-chip antennas and the external coil (yellow) are connected to current sources via twisted-pair wires. We label the feed line of the sample reached by input port a '1' and the opposing side '2'.

sample from room temperature noise. Ideally, we would like to place all of the attenuation at the lowest temperature stage, because the output noise of each attenuator depends on its temperature. But since the cooling power of the cryostat is limited, especially at low temperature stages, it is important to divide the attenuation between different stages. With this, the heat created by the attenuators can be easily cooled and doesn't heat up the cryostat, even if we apply a high input power. In total we attenuate the signal strength by 100 dB, most of which we apply at room temperature (40 dB) and 30 mK (30 dB). The rest is divided into three 10 dB attenuators at each stage. Input lines are made from stainless steel, which also contributes to the attenuation. The input signal is then filtered around the frequency of the resonator. We choose a broad filter[2] with a passband between 4 GHz and 8 GHz as the resonators are tunable. After the attenuator at 30 mK, the cabling is made from the superconductor Niobium-Titanium. The input and output signals connected at the sample are separated by a cryogenic circulator.

Microwave output lines

The microwave output signals from the sample to the detector are guided through coaxial cables. A second circulator at 30 mK shields the sample from noise signals from higher-temperature stages. Via the 50 Ω load of this circulator, the inner conductor is thermalized to this temperature stage. Another circulator is placed at the still stage. As we are dealing with very low signal strength during our experiments, we add multiple amplification stages. The noise temperature of the amplification chain is limited by a high-electron-mobility-transistor (HEMT) at 4 K. At the operation frequency of the sample, the HEMT amplifies the signal by roughly 35 dB. Between sample and HEMT amplifier, all cabling in the output line is done with UT85 superconducting niobium-titanium coaxial cabling in order to minimize losses. After this stage, losses are not as critical, as the signal is already heavily amplified. The overall noise temperature of the amplification chain is given by the Friis formula

$$T_{\text{total}} = T_1 + \frac{T_2}{G_1} + \frac{T_3}{G_1 G_2} + ... \tag{4.1}$$

Here, T_i is the noise temperature of the i-th component in the chain and G_i is its power gain in ratios. One easily sees, that losses (i.e., gain values lower than one) before the first amplification step can strongly increase the noise temperature. In addition the contribution of an amplifier to the total noise temperature is reduced by the gain of previous stages. As a consequence, after the HEMT, stainless steel cables can be used up to room temperature. Outside of the fridge, we add a fourth circulator in order to prevent any backwards reflection into the HEMT amplifiers from the second amplifier stage. Here, we use a JS2 amplifier, with a gain of approximately 23 dB. The outputs of this room temperature amplifier is then connected to either the vector network analyzer (see Sec. 4.2.3) or an intermediate frequency (IF) downconversion box (see Sec. 4.2.4). In

[2] VHF-3500+ made by Mini-Circuits

the second case, we use an additional JS2 amplifier, which is directly connected to the first one.

On-chip antennas and superconducting coil

We connect both on-chip antennas and a superconducting coil with DC-wires to external current sources. In addition, the antennas are also connected to microwave cables, but these are not used during the experiments presented here. This connection is done by using a bias-T which combines microwave and DC wiring. The current sources that apply the current I_{ant1} and I_{ant2} for the DC flux through the antennas are home-made current sources with a range of up to 10 mA. We find that, when we apply a current of 1.5 mA, the sample slowly heats up. At currents above 2 mA the sample often heats up above the critical temperature of aluminum and and superconductivity breaks down. We therefore operate the antennas at a maximum of 2 mA. The superconducting coil is equipped with a persistent current switch. When setting the current through the coil I_{coil}, this switch heats a superconducting shunt so that the current through the coil can be changed. We operate the switch at 60 mA. The current itself is controlled by a Keithley 6430 current source. We find that the magnetic field created by the coil has a hysteretic dependence on the applied current. We therefore take care to set the current through the coil always in the same way, starting at 0 mA and increasing it slowly to its set value. The current ramp rate also influences the reproducibility of the set point. We operate the antennas at 10 µA/s and the coil at 0.1 mA/s, which allows us to reproducibly set the magnetic fields created by the coil and antennas to the correct value.

4.2.3 Spectroscopic measurement setup

For spectroscopic measurements, we connect the microwave input and output lines to a VNA (PNA 5222A), which has a frequency range of 10 MHz to 26.5 GHz. For a typical measurement, we excite the system at one of the two input ports and measure both reflection of and transmission through the sample (see Fig. 4.3). For a full set of S-parameters, we have to perform two separate measurements. In addition, we can sweep the magnetic flux through the SQUID loop by tuning the current through the external coil or the on-chip antennas and perform a VNA measurement at each sweep point. This allows us to directly see the dependence of the frequency response as a function of the applied magnetic flux.

4.2.4 Correlation function measurement setup

In order to measure correlation functions and to perform photon number calibrations, we attach our cryogenic setup to a homemade copper downconversion box containing a set of mixers, filters and IF amplifiers. The output of the box is connected to a FPGA-

enhanced analog-to-digital (ADC) converter card. Inside the copper box, we convert the measurement signal from its frequency between 4 GHz and 8 GHz, to an intermediate frequency of 11 MHz. This signal is sampled by the ADC card with a sampling frequency of 175 MHz, filtered, digitally downconverted to DC, and split into its in-phase and quadrature (IQ) components. The analog downconversion step brings the signal into a frequency range which can conveniently be recorded by commercial ADC cards. With an analog down conversion to 11 MHz, a sample rate of 44 MHz would be sufficient. The digital downconversion step is implemented in the FPGA logic of the ADC card. It is used to avoid $1/f$-noise, which is omnipresent in the measurement electronics. In the following, we present more details about the downconversion box and the FPGA logic.

Downconversion box

We place all devices used for the analog down conversion inside a copper shielding box. A sketch of it is shown as part of the room temperature setup for the correlation measurements in Fig. 4.4. The box features two identical paths, which allow us to detect two signals simultaneously. This is necessary in future experiments in order to measure cross-correlation functions between the two resonator fields. In each path, the signal first passes through an isolator. Afterwards a first pass band filter with a passband of 5.6 GHz to 7.0 GHz cuts off the signal around the frequency range of the sample. Then, the signal enters an IQ-mixer. The outputs of this mixer are two output signals, one, where the signal is multiplied by a sine with the frequency of a local oscillator (LO) and one where the signal is multiplied by a cosine with the frequency of the LO. The output signals I and Q are given by

$$I = S \cdot \sin(2\pi \cdot f_{\mathrm{LO}} \cdot t) \tag{4.2}$$

$$Q = S \cdot \cos(2\pi \cdot f_{\mathrm{LO}} \cdot t), \tag{4.3}$$

where S is the signal incoming to the rf port and f_{LO} is the frequency of the local oscillator. The local oscillator signal is created by an additional signal source and wired into the box. I and Q are then filtered with a bandpass filter and split with a beam splitter. An isolator at the entrance of the IQ-mixer prevents any back scatter and especially any signal flow between the two paths. We detune the local oscillator frequency f_{LO} by 11 MHz from the signal frequency f_{signal}. I and Q each consist of two signals with a frequency of $f_{\mathrm{signal}} \pm f_{\mathrm{LO}}$. With a set of four filters, we heavily filter around the lower frequency $f_{\mathrm{signal}} - f_{\mathrm{LO}}$, so we can omit the part of the signal with higher frequency. After downconversion to the IF frequency, we use a third room temperature amplifier to further increase the signal strength. This amplifier adds an additional amplification of 56 dB in a frequency range between 0.001 MHz and 400 MHz. At the output of the downconversion box, a DC-Block with a cutoff frequency of 7 kHz additionally filters out any DC signal. The output of the

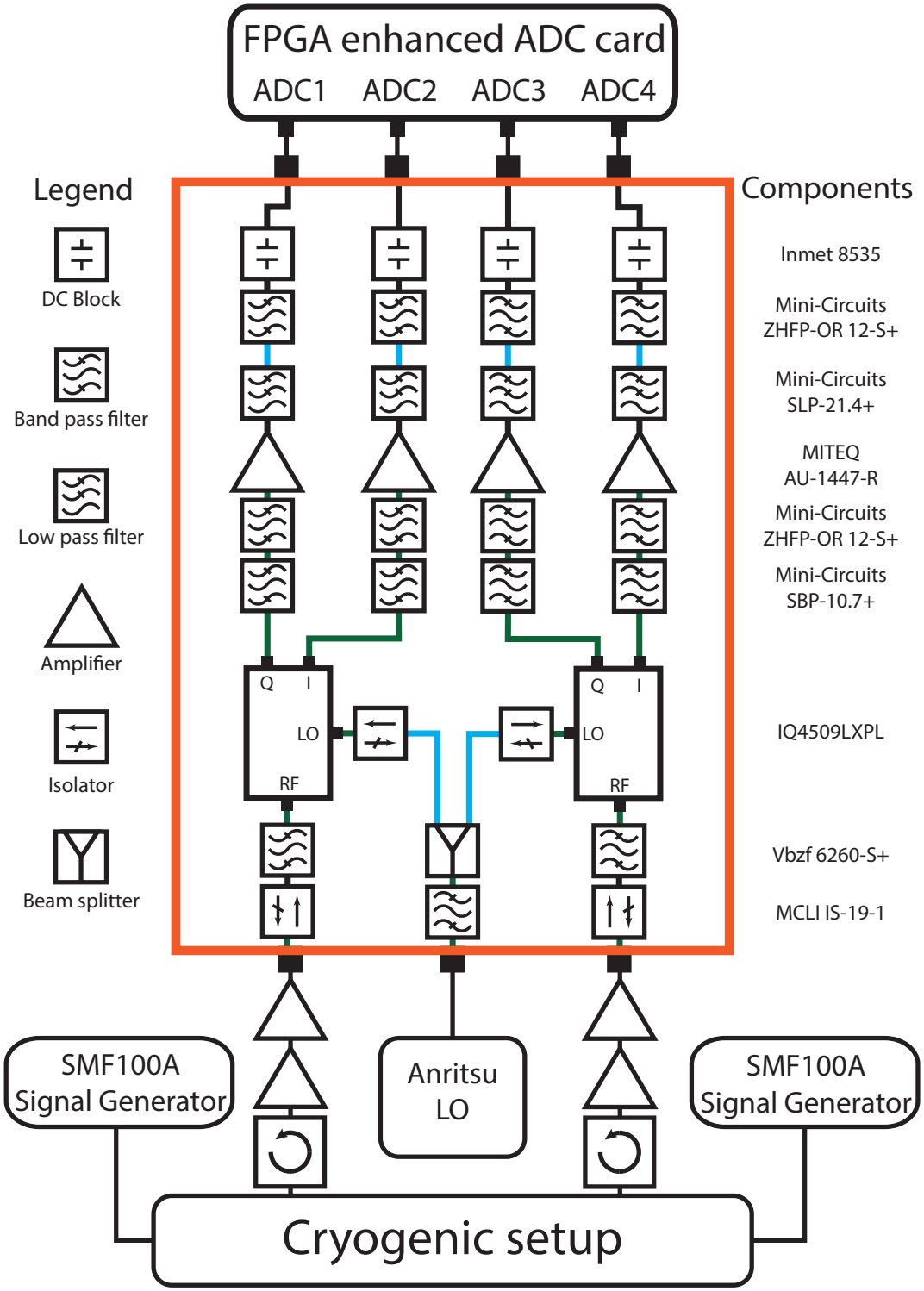

Figure 4.4: Room temperature setup for the correlation function measurements. The microwave output lines of the cryostat are fed into an analog downconversion box (orange) and after down conversion and filtering are digitized and processed by an FPGA-enhanced ADC card. Components are either directly connected to each other (black connection) or connected with a SMA adapter (green connection) or short cable (blue connection).

box consists of two pairs of ports, each composed of an I and Q signal part. These four signals are then wired to the FPGA-enhanced ADC card, where they are digitized and processed further.

FPGA-enhanced ADC card

In the following, we explain in details the working principle of the ADc card and its FPGA logic. We use a x6-250M card from Innovative Integration, which features eight 16-bit ADCs. Our logic only uses four of these inputs. The output ports of the mixer box are connected to these input ports of the card.

Any sinusoidal signal can be described as a sum of an in phase and quadrature component.

$$S = I\cos\left(2\pi \cdot f_{\text{signal}} \cdot t\right) + Q\sin\left(2\pi \cdot f_{\text{signal}} \cdot t\right) \tag{4.4}$$

The RF output signal of the sample is converted in the downconversion box to their in-phase and quadrature components oscillating at the IF frequency,

$$I_{\text{IF}} = \frac{1}{2}(I\cos(\omega_{\text{IF}}t) + Q\sin(\omega_{\text{IF}}t)) \tag{4.5}$$

$$Q_{\text{IF}} = \frac{1}{2}(-I\sin(\omega_{\text{IF}}t) + Q\cos(\omega_{\text{IF}}t)). \tag{4.6}$$

An exemplary signal can be seen in the middle panel of Fig. 4.5. After data acquisition by the ADCs with a sample rate of 175 MHz, the signal is digitally processed by the FPGA logic. In the following we will discuss the different steps taken by the card. In the first step, the card performs a digital down conversion (DDC), similar to the down conversion of the IF-mixer box. For this, the sine and cosine components of a digital local oscillator signal with frequency ω_{IF} are multiplied with the digitized IF signal

$$I_{\text{DC}} = I_{\text{IF}}\cos(\omega_{-}t) - Q_{\text{IF}}\sin(\omega_{-}t) = \frac{1}{2}\cdot I \tag{4.7}$$

$$Q_{\text{DC}} = I_{\text{IF}}\sin(\omega_{-}t) + Q_{\text{IF}}\cos(\omega_{-}t) = \frac{1}{2}\cdot Q. \tag{4.8}$$

For signals near the frequency ω_{rf}, the resulting signals I_{DC} and Q_{DC} are quasistatic components in the sense that they only reflect modulations of the original signal on timescales corresponding to the effective filter bandwidth resulting from analog filtering, digital filtering and averaging (see Fig. 4.5).

From a technical point of view, we have to consider that Eq. (4.7) and Eq. (4.8) also upconvert spurious low-frequency signals, creating unwanted terms oscillating at $2\omega_{\text{IF}}$.

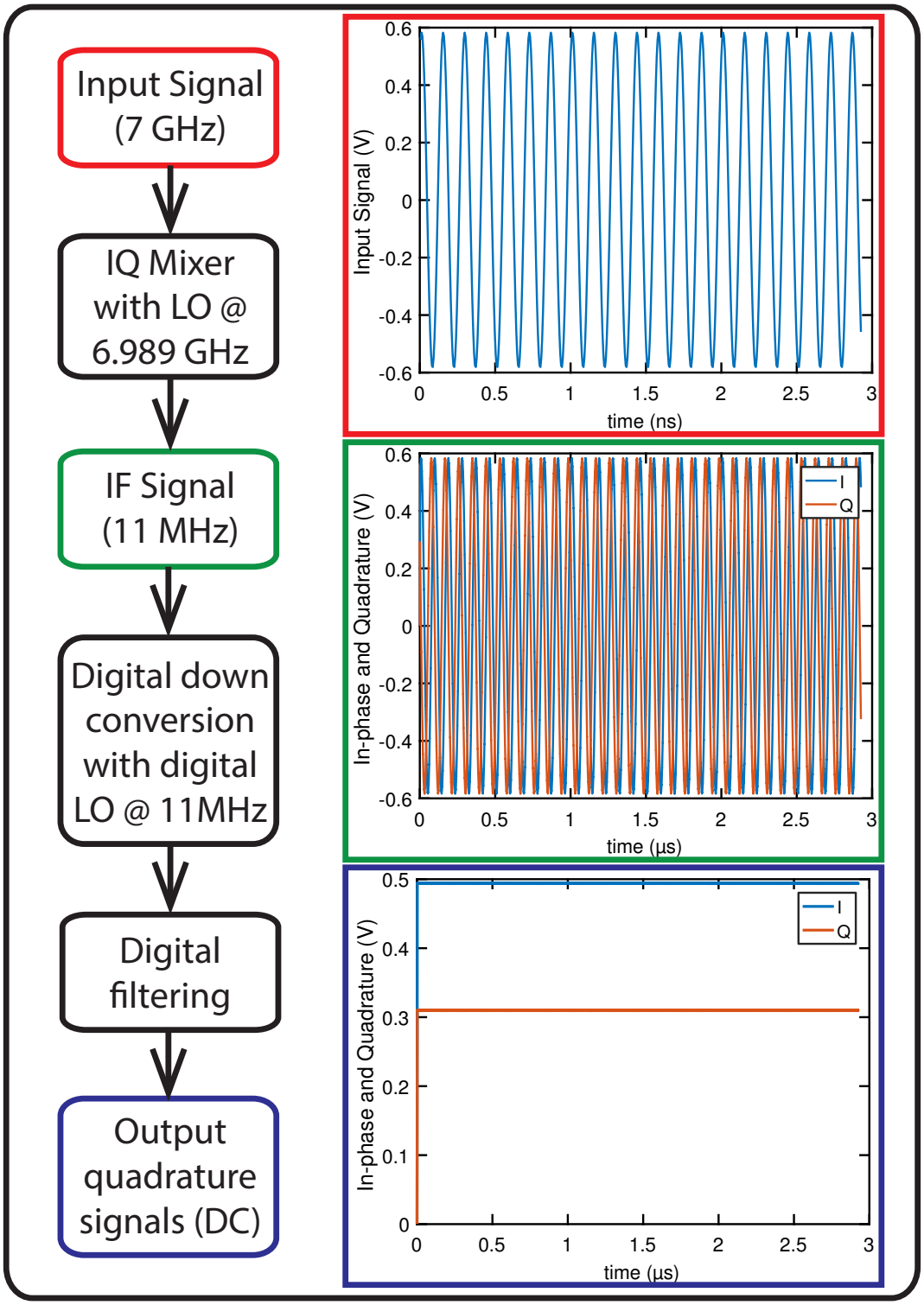

Figure 4.5: Working principle of the logic on the FPGA card. The input signal is digitally downconverted and filtered and all moments of the in-phase and quadrature component up to forth order are calculated. In order to give specific numbers, we have assumed a realistic signal frequency of 7 GHz in this sketch.

We therefore use a set of two digital filters. The first filter is a cascaded integrator-comb (CIC) filter. CIC filters combine integrator stages of the form

$$y[n] = y[n-1] + x[n], \tag{4.9}$$

where $y[n]$ ($x[n]$) is the n-th sample after (before) filtering, and comb stages of the form

$$y[n] = x[n] - x[n-1]. \tag{4.10}$$

A typical CIC filter consists of multiple integrator steps and multiple comb steps with a change of sampling rate in between. Integrator steps are run with the original sampling rate. Afterwards, the sampling rate is reduced in order to improve the efficiency of the filter and to reduce complexity of the filter architecture. After this filter step, we account for the filter gain by dividing the signal by the gain in order to stay in our computational data size. The main purpose of the CIC filter is to keep the computational complexity of the subsequent second filtering stage to a level which can still be handled by the FPGA resources. The second filter stage is a finite impulse response (FIR) filter. Here, the filter function is given by

$$y[n] = \sum_{i=0}^{N} (c_i \cdot x[n-i]), \tag{4.11}$$

where c_i is a set of filter coefficients, and N is the order of the filter. The filter coefficients define the shape of the filter function and its cut-off frequency. In the last step of the on-board data processing, all multiples of I and Q up to the fourth order are calculated($I^n \cdot Q^m$ with $m+n \leq 4$). From these values we compute an average of the signal moments $\langle I^n \cdot Q^m \rangle$ with $m+n \leq 4$. At this point, the data is transferred to a measurement computer, where it can be further processed or saved. The key purpose of the FPGA logic is to perform digital downconversion, digital filtering and moment calculation close to real time. This performance is possible, because we only have to send one strongly averaged data trace including all computed moments to the measurement computer in time intervals on the order of minutes. Otherwise the data transfer of each measured trace before the calculation and averaging, as well as the processing time on a standard computer, would dominate the measurement time.

Data format and parameters

The ADCs for data acquisition have a 16 bit resolution and operate at a sampling rate of 175 MHz. The logic is programmed to continuously measure traces with 8192 points after a trigger event until a set number of averages is reached. With a CIC down sampling factor of 16, we end up with traces with a length of 512 points or, equivalently, 46.8 µs.

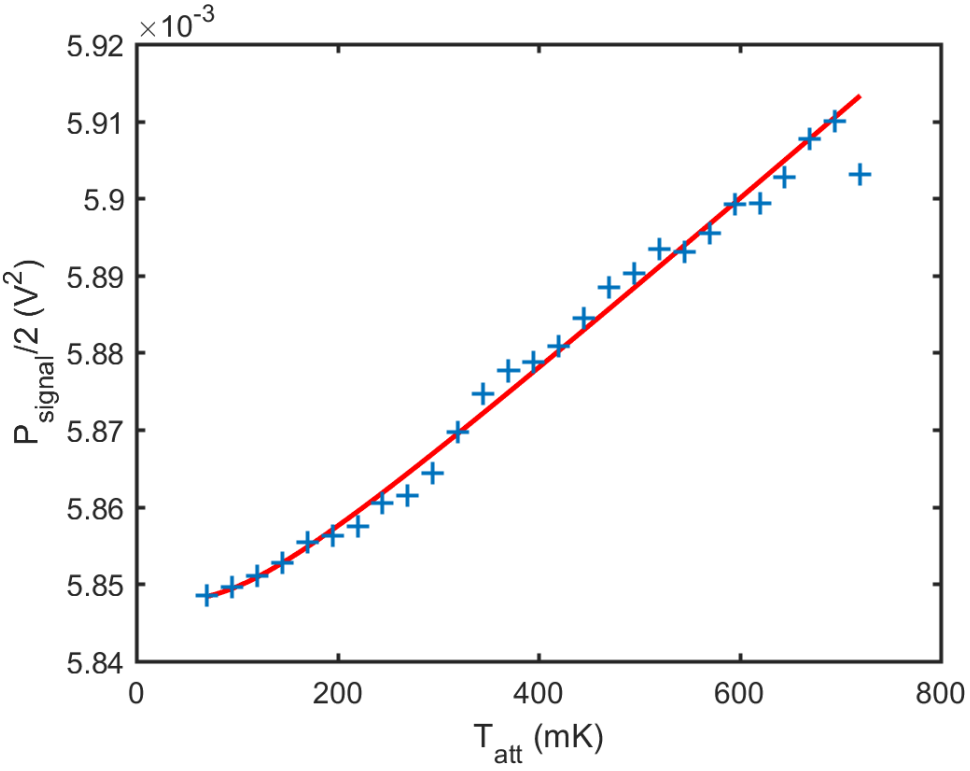

Figure 4.6: Measurement of the signal power P_{signal} in a temperature sweep of the heatable attenuator (blue symbols) while the resonators are far detuned from the signal frequency probed by the correlation measurement setup. The red line is a fit to the data using Eq. (4.12).

Due to digital filter ringup, we have to discard a number of points. The ringup time depends on the number of FIR filter coefficients. Using just the CIC filter drastically reduces ringup time. After filtering and moment calculation, we perform the averaging using 128 bit numbers. In this way, we are able to perform averaging up to millions of averaged traces without running into overflow problems.

Photon number calibration factor

As we cannot directly measure the gain of our amplification chain while the cryostat is cold, we perform Planck spectroscopy [65, 66] as a photon number calibration measurement. To this end, we use a heatable attenuator, that emits black body radiation towards the input of the sample. With the resonators far detuned, the signal is reflected into our amplification chain, and we can measure the resulting power with a digitizer card at room temperature. Before digitizing the signal, we convert the signal to an intermediate frequency of 11 MHz with an analog mixer setup. After digitizing, the data is digitally downconverted to DC. As a result, we get the in-phase (I) and quadrature (Q) components of the measured signal as a DC value. We can then write the power of the signal as a

function of the temperature of the attenuator

$$P_{\text{signal}} = \frac{I^2 + Q^2}{R} = \frac{\kappa G_{\text{cal}}}{R}\left[\frac{1}{2}\coth\left(\frac{hf_0}{2k_{\text{B}}T_{\text{att}}}\right) + n_{\text{noise}}\right], \tag{4.12}$$

with the Boltzmann constant k_{B}, $\kappa = 2R{\cdot}BW{\cdot}hf_0$, BW the bandwidth of the measurement and G_{cal} the total gain of the amplification chain. We perform a temperature sweep of the heatable attenuator and measure the resulting output quadrature components, which we can fit to the formula for the black body radiation. The result of this fit is the product κG_{cal}, which relates the number of photons at the sample to the measured voltages and the photon number n_{noise} of the noise of the amplification chain. In our setup, this photon number is dominated by the noise number from the cryogenic amplifier in the chain. In Fig. 4.6, we show a temperature sweep from 50 mK to 800 mK. From the fit, we get $\kappa G_{\text{cal}} = 8.1\,(\text{mV})^2/\text{photon}$ and a noise number $n_{\text{noise}} = 142$. The high noise number can be explained by aging effects in our HEMT amplifiers. Using the measurement bandwidth of $BW = 2\,\text{MHz}$, we can calculate the gain of the chain and find $G_{\text{cal}} = 109.8\,\text{dB}$. As we perform this calibration measurement with a slightly different setup (including an additional downconversion box, containing an intermediate frequency amplifier with significant gain), we cannot directly use this gain measurement for the interpretation in the experiments performed with a VNA.

In order to estimate the gain of the VNA setup, we measure the gain of the additional room temperature components used in the determination of G_{cal}. We measure the gain of the downconversion box, $G_{\text{box}} = 47.3\,\text{dB}$, and the gain of an additional rf room temperature amplifier $G_{\text{rf-amp}} = 24.6\,\text{dB}$. If we subtract these two values from the determined total gain G_{cal}, we get a value of the gain of the VNA setup $G = 38 \pm 4\,\text{dB}$, which we use in the main text of this paper. The uncertainties stem mainly from the frequency dependency of the gain as the measurement of the gain and of the nonlinearity have been performed at different frequencies (3 dB) and the different cables used in the two measurements, which cannot be reliably accounted for in our estimation (1 dB). The uncertainty in the gain is the main contribution to the uncertainty of the nonlinearity.

4.3 Characterization of the superconducting circuit

In this section, we present characterization measurements of our circuit. We show, that we are able to model the dependency of the resonance frequency on the flux created by the external coil as well as on the flux created by the on-chip antennas. Using these tuning knobs, we are able to tune the resonators in and out of resonance at any arbitrary frequency point within the bounds of the single resonator tunability.

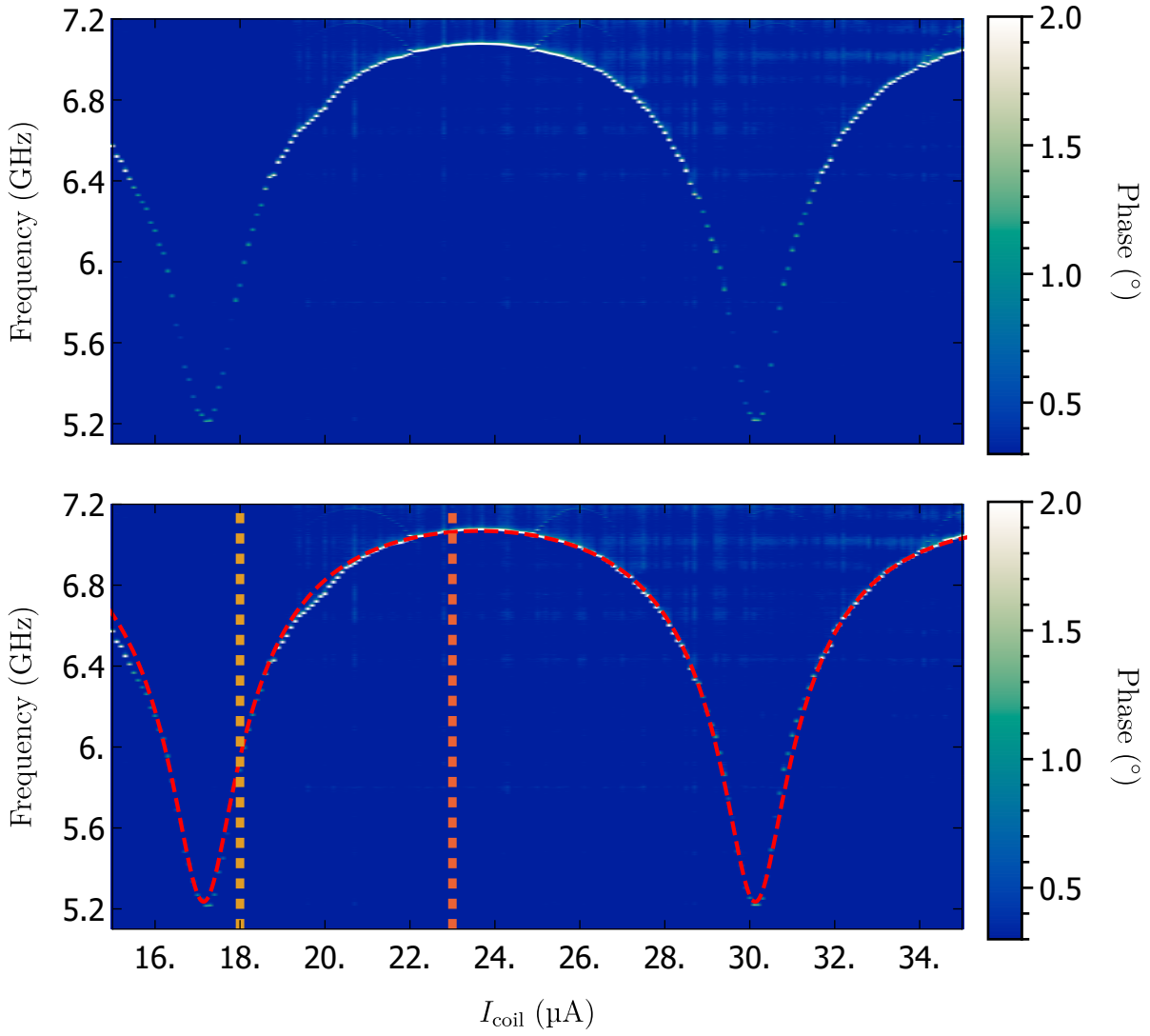

Figure 4.7: Measurement of the phase of the scattering parameter S_{11}. The resonance frequency of resonator 1 is clearly visible and performs a full oscillation within the current region shown in this figure. A theoretical calculation [Eq. (4.13)] (bottom panel, red dashed line), allows us to extract important system parameters (see Tab. 4.2).

Table 4.2: Resonator parameters

	$I_c(\mu A)$	$\Delta\Phi(\Phi_0)$	$\Delta\Phi/\Delta I_{coil}(\Phi_0 \mu A^{-1})$	d
Res 1	1.40	-0.18	0.077	0.147
Res 2	1.80	0.50	0.213	0.147

4.3.1 Influence of the external coil

First, we look at the individual response of each resonator. For this, we measure the scattering parameters S_{11} and S_{22}, which show the reflection of the system. If the resonators are detuned from each other, the signal enters the first resonator if it is on resonance, but cannot enter the second. The signal is therefore reflected, but obtains a phase shift. We extract the resonance frequency of an individual resonator by looking at the phase of the reflection measurement

Reflection measurements of resonator 1

A measurement of S_{11} for different current values I_{coil} through the external coil is shown in Fig. 4.7. We sweep the VNA input frequency from 5.2 GHz to 7.2 GHz and measure the signal at the output port. The resonance frequency is visible as a phase peak. We tune the resonance frequency of resonator 1 from 5.24 GHz to 7.07 GHz by changing the coil current by $\Delta I_{coil} = 6.58\,\mu A$. We can model this change in resonance frequency using equations 2.55 and 2.56 as

$$f_{res,i} = \frac{1}{2\pi\sqrt{L_i\left(\Phi_{ext,i}\right)\cdot C_i\left(\Phi_{ext,i}\right)}}, \tag{4.13}$$

where i denotes the resonator. The result of this calculation for resonator 1 is overlayed onto the measurement in the bottom panel of Fig. 4.7. The maximal resonance frequency of each resonator is determined by the maximal critical current of the two DC-SQUIDS which lets us directly extract this important parameter from the model. The minima of the dependence on the other hand are a result of the asymmetry parameter d of the junctions of each DC-SQUID. We introduce a parameter that relates the coil current I_{coil} to the effective external flux $\Phi_{ext,i}$, which is given in units of $\Phi_0/\mu A$ and one, that determines the amount of flux $\Delta\Phi$ that is applied to the SQUID loops for $I_{coil} = 0$. We determine the parameters of the model by matching the measured behavior. We find a parameter set (see Tab. 4.2), that recreates the dependency of the resonator on the external flux.

Reflection measurements of resonator 2

We perform a similar measurement in order to extract the parameters for resonator 2. We apply the input signal directly to resonator 2 and measure S_{22}. The measurement is shown

in Fig. 4.8. We find, that we can tune resonator 2 from 5.59 GHz to 7.17 GHz by changing the coil current by $\Delta I_{\mathrm{coil}} = 2.78\,\mu\mathrm{A}$. Parallel to the treatment of resonator 1 the resonance frequency of resonator 2 can be modeled by equation 4.13, and we can extract the model parameters (see table 4.2). We notice, that although the two resonators are equal by design, they differ both in critical current and in their dependence on the current through the external coil. The obtained critical currents for the two SQUIDs are $I_{\mathrm{c},1} = 1.40$ and $I_{\mathrm{c},2} = 1.80$. This difference stems from inaccuracies in the junction fabrication, where a spread of the critical current of up to 20 % is not unusual for homemade junctions [67]. To get a better understanding of the origin of these inaccuracies, we can also take a look at the asymmetry parameter d. We find, that for both SQUIDs the asymmetry is the same $d_1 = d_2 = 0.147$. This shows us, that the ratio of the critical currents of the Josephson junctions in each SQUID has to be the same for the two SQUIDs. Therefore it is likely, that the difference stems from variations in fabrication, that occur on a large scale, compared to the SQUID size. These variations can be created by a slight misalignment of the sample in z direction by e.g. residual resists below the chip. The focus of the beam is then different for different regions of the sample and can create sharper or less sharp junctions or even junctions of different size, which can both lead to a difference in critical current. It is also possible, that the oxidation process occurred with a different speed at the two SQUID sites, which would create different critical current densities, also affecting the critical current. In the next section, where we show transmission measurements through the whole system, we also discuss the differences in the dependence on the external coil current in more detail.

Transmission through both resonators

We measure transmission through the two resonator system and show the influence the external coil has on the combined system. Fig. 4.9 is a VNA measurement of the scattering parameter S_{21} as a function of the current through the external coil I_{coil} and the frequency applied by the VNA. In a transmission measurement, one can see the resonance frequencies of each resonator as peaks in transmission. As already shown in the previous sections, both resonance frequencies are shifted by the external coil. In the displayed coil current window from 10 µA to 30 µA the resonance frequencies both undergo more than a full oscillation. We observe a maximal resonance frequency of 7.14 GHz for resonator 1 and a maximum of 7.20 GHz for resonator 2. Again, this difference in maximal frequency of 0.06 GHz is a direct indication for a difference in critical current of the SQUIDs, which is also evident from the calculated paramters (Tab. 4.3) using Eq. (4.13). Note that, as the reflection measurements and the transmission measurements we show here, were performed in different cooldowns, the maximal resonance frequency and therefore the critical currents of the SQUIDs differ between the measurements. Changes in critical current of Josephson junctions due to degrading effects and mechanical stress during warmup and cooldown procedures, is a well known and typical occurrence. The difference

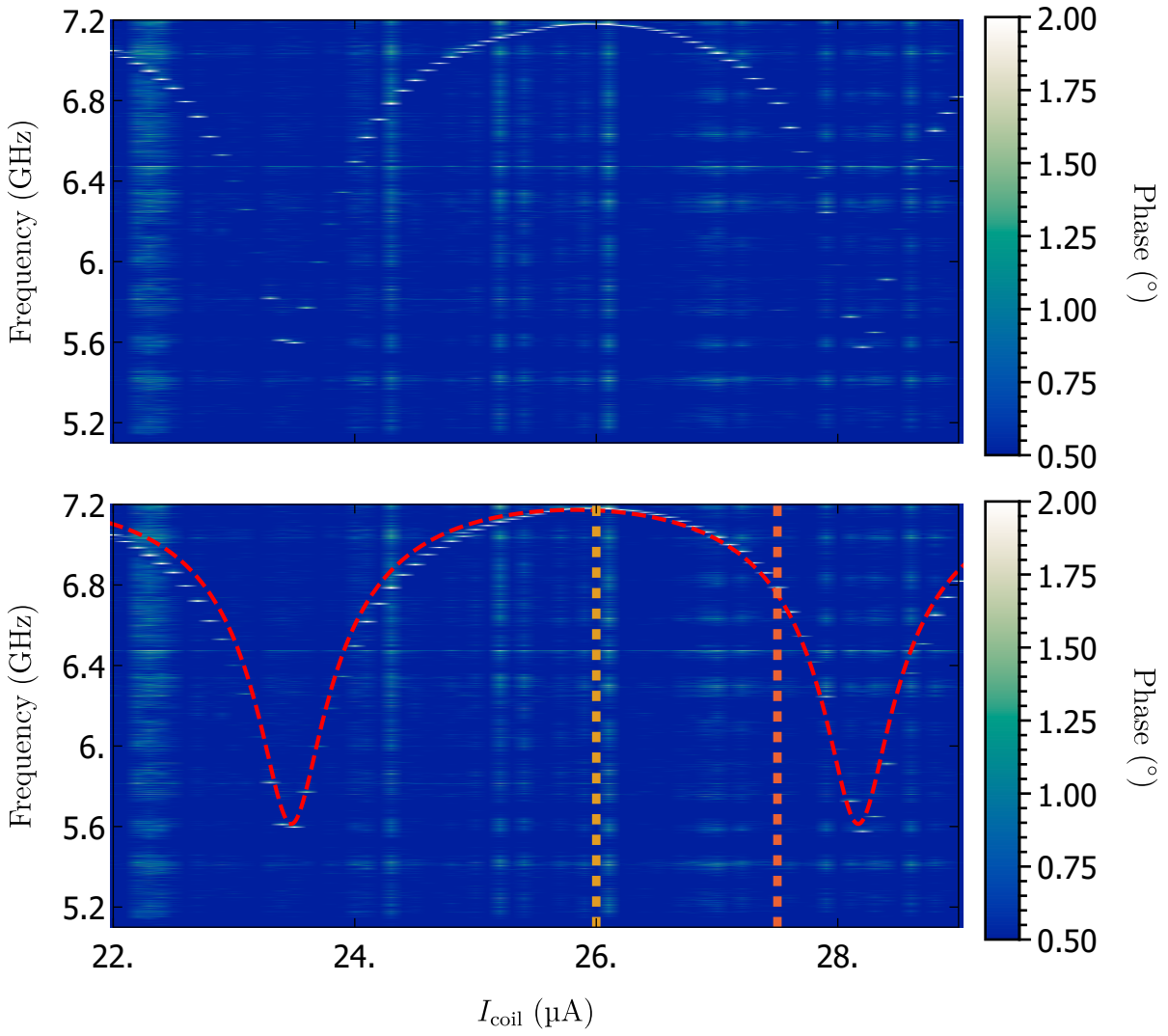

Figure 4.8: Measurement of the phase of the scattering parameter S_{22}. The resonance frequency of resonator 2 is clearly visible and performs a full oscillation within the current region shown in this figure. A theoretical calculation of the measured dependency (bottom panel, red dashed line), allows us to extract important system parameters.

Table 4.3: Parameters of the two resonators

	$I_c(\mu A)$	$\Delta\Phi(\Phi_0)$	$\Delta\Phi/\Delta I_{coil}(\Phi_0 \mu A^{-1})$	d
Res 1	1.65	-0.39	0.076	0.147
Res 2	1.93	0.08	0.199	0.147

in maximal resonance frequency is well below 0.1 GHz for both resonators. The calculated resonance frequencies for both resonators overlayed on the data can be seen in Fig. 4.10. While resonator 1 is visible over the whole measurement span, the resonance frequency of resonator 2 vanishes while it is far detuned from resonator 1. We can explain this behavior by the influence of the environment of the sample. For a detailed description, see section 5.1. We also notice that for smaller coil currents $I_{coil} \leq 14\,\mu A$, the expected and measured resonance frequency deviate by up to 0.1 GHz, which stems from a nonlinear dependency of the external flux applied at the SQUID loop on the coil current. For low coil currents (0 µA to around 6 µA, not depicted in the measurement here), we find a strongly hysteretic behavior of this dependency. As the coil is a larger coil with many windings, this hysteresis likely comes from charging effects of the coil. For higher coil currents we also observe a deviation from the expected linear behavior. Here we find that the external flux changes faster for higher coil currents. For a further discussion of this behavior, that we can also observe in measurements where we apply flux through the on-chip antennas, can be found in chapter 4.3.2.

In addition to the different maximal resonance frequencies, resonator 2 has a larger mutual inductance with the external coil than resonator 1. The main influence on the conversion from the coil current to the actual flux through the SQUID loops should be the position of the SQUID in relation to the coil and the size of the SQUID loop. As both the sample design and the position of the coil are chosen to be symmetric, the reaction of the two resonators to the external coil should be the same. We suspect that the reason for the observed difference stems from additional superconducting loops that are created by the bond wires. As they are not placed perfectly symmetrical on the sample, induced on-chip current flow can differ between the two SQUIDs.

We are able to tune the resonators in and out of resonance using the external coil. In the bottom panel of Fig. 4.9, we show cuts of the sample's frequency response at two coil currents. For $I_{coil} = 18.5\,\mu A$ the two resonators are far detuned and we can observe the single resonator response of resonator 1. For $I_{coil} = 21.5\,\mu A$, the degeneracy point is reached and the resonance frequencies exhibit an avoided crossing.

As the measurement does not show the lowest possible resonance frequencies, we individually show the calculated frequencies in Fig. 4.11. The frequency range, where both resonators can be brought into resonance, is defined by the maximum of resonator 1 and the minimum of resonator 2. This gives us a range from 5.67 GHz to 7.14 GHz, which is a span of 1.47 GHz.

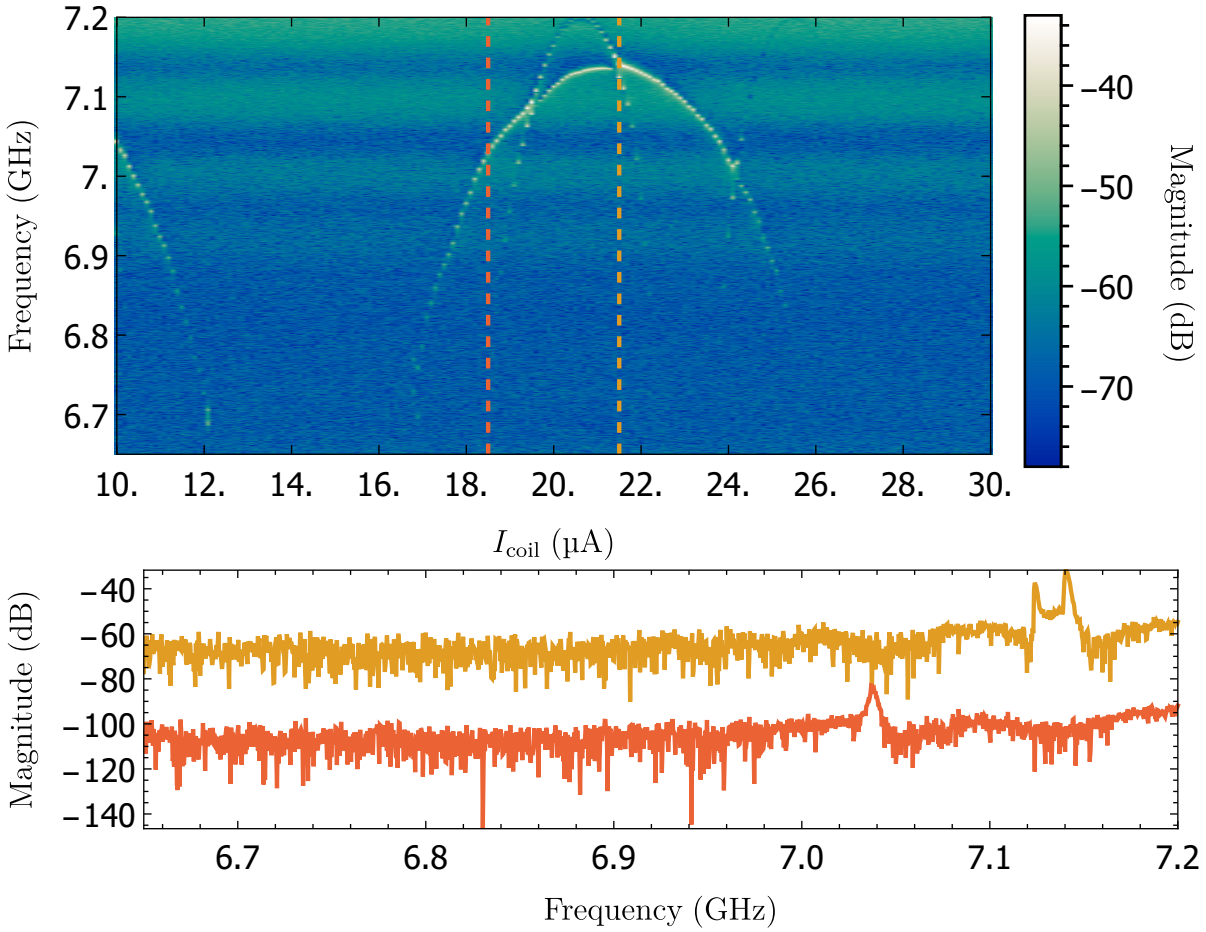

Figure 4.9: Transmission magnitude S_{21} through both resonators in dependence of the coil current and the applied frequency. We can see the two resonators tuning in and out of resonance multiple times of the span of 20 µA. The bottom panel shows cuts at 18.5 µA (red, resonators detuned) and 21.5 µA (yellow, resonators in resonance).

4.3.2 Antenna sweeps and full control

In this chapter, we show, that in addition to the external coil, we can also use two on-chip antennas in order to tune and control the resonance frequencies of our system. On-chip systems offer fast tuning, but are prone to crosstalk and can therefore negatively affect the actual circuit. For our system they are necessary, as we cannot address each resonator individually with the external coil, but if we want to tune the two into resonance at any possible frequency point, it is vital that we are able to do so. On-chip antennas are designed to create a local magnetic field near the end of its antenna line, so that only the close vicinity of the antenna is affected. In theory, we can use this in order to individually tune the external flux through one SQUID loop in order to control each resonator independently. Our sample features two antennas, each located near one of the two SQUIDs (see Sec. 4.1).

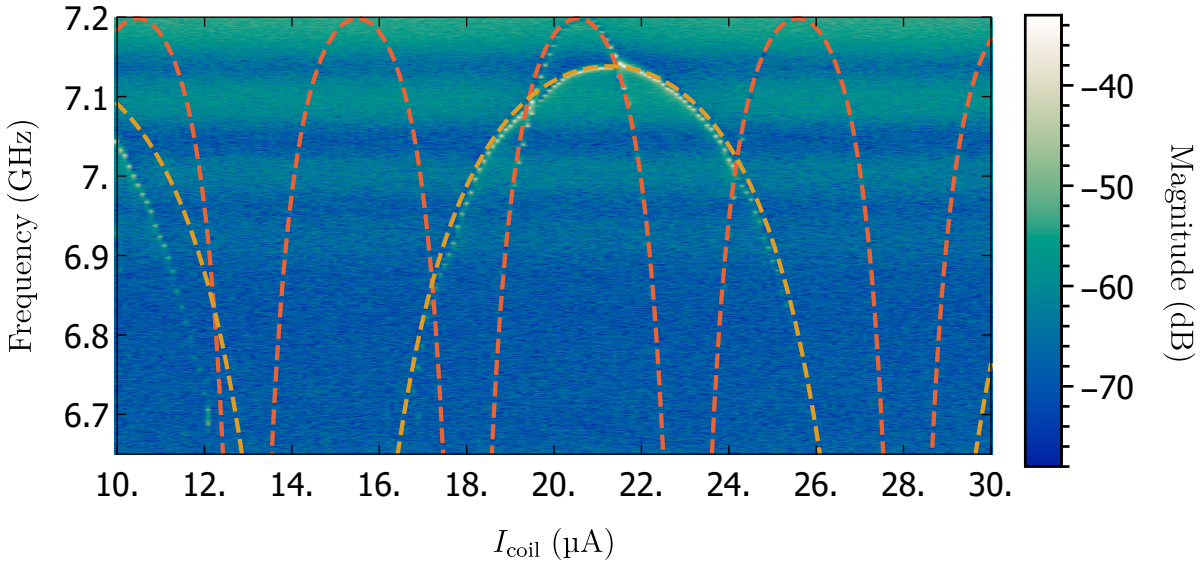

Figure 4.10: Measured transmission through the resonator system with the calculated resonance frequency of resonator 1 (yellow) and resonator 2 (red) overlayed. We see, that between 14 and 28 µA the theoretical descriptions models the data well.

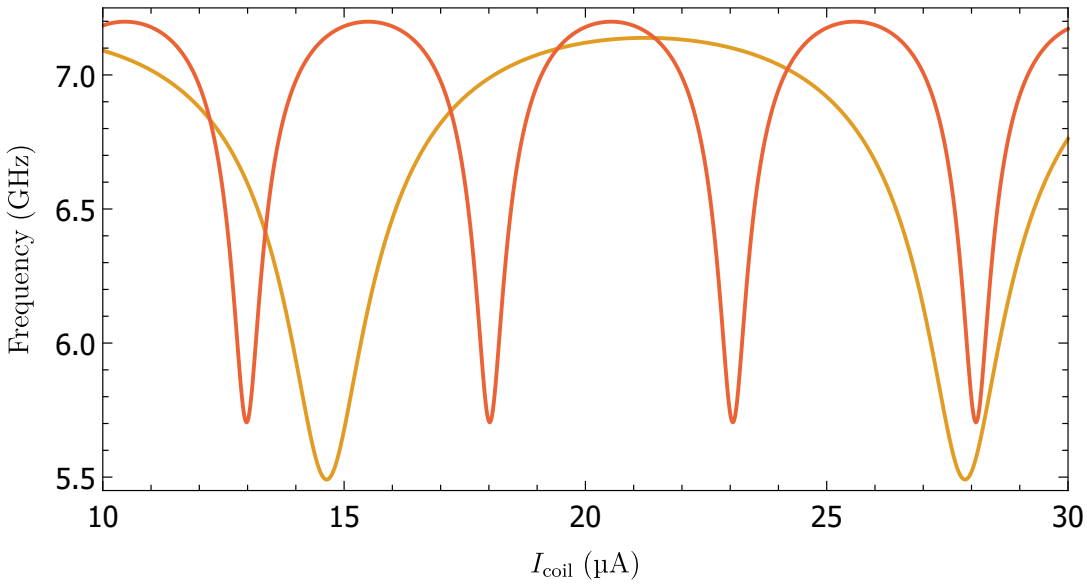

Figure 4.11: Calculated resonance frequency of resonator 1 (yellow) and resonator 2 (red) in their full frequency range.

Table 4.4: Parameters of the two resonators

	$\Delta\Phi(\Phi_0)$	$\Delta\Phi/\Delta I_{\mathrm{A1}}(\Phi_0\mathrm{mA}^{-1})$	$\Delta\Phi/\Delta I_{\mathrm{A2}}(\Phi_0\mathrm{mA}^{-1})$
Res 1	-0.25	0.58	1.1
Res 2	0.05	0.075	0.59

Heating effects of the on-chip antennas

When we apply a current through the antennas, we observe heating effects across the whole chip structure. In order to quantify these effects, we look at the temperature of the sample box with a thermometer that is fixed on the outside of the box. Up until roughly 1500 µA, the sample temperature rises on the order of tens of mK. For currents larger than this, the temperature increased drastically in some experiments even exceeding the critical temperature T_c of aluminum. This rise occurs on a short time scale, at a time, where the full sample stage was still at temperatures far below T_c. We therefore suspect, that the current flow locally heats small parts of the sample above T_c, which leads to a high resistance in this part, which in turn accelerates the heating process. The most likely candidates where this heating takes place is either the small conductor that forms the antenna itself, or the aluminum bonds, that are used to connect the sample to the PCB. The latter are likely, as they do not offer a perfect connection. Mechanical stress, corrosion or oxidation can weaken the electrical connection and lead to a finite resistance in the bond or the bond connection. We account for this heating effect, by limiting the current through the antennas. In the following sections, where we show the influence of the antennas on the two measurements, we show a measurement, where the mentioned drastic increase in temperature does not happen, and we are able to present data up to 2000 µA.

Flux tuning and crosstalk using antenna 1

In our measurements, we observe a strong crosstalk between the two on-chip antennas. We therefore investigate both the effect each antenna has on the resonator that is close by, and the resonator that should be unaffected by the antenna. In Fig. 4.12, we show a reflection measurement (S_{11}) of resonator 1, where we increase the current through antenna 1. For better visibility, we show the phase of the scattering parameter. We can clearly see, that in the range of 2000 µA, we can change the resonance frequency of resonator 1 from the minimal frequency of our frequency range 6.90 GHz to the resonators maximal frequency of 7.14 GHz and back. Similar to the treatment of the coil sweeps, we can use the theoretically expected dependence to calculate the conversion between the current through the on-chip antenna and the created flux through the SQUID loop. We find, that with antenna 1 we can create one flux quantum in the loop of resonator 1 over the span of 1724 µA, giving us a tuning rate of 0.58 $\Phi_0\mathrm{mA}^{-1}$.

The cross talk between the current applied to the antenna of resonator 1 and resonator

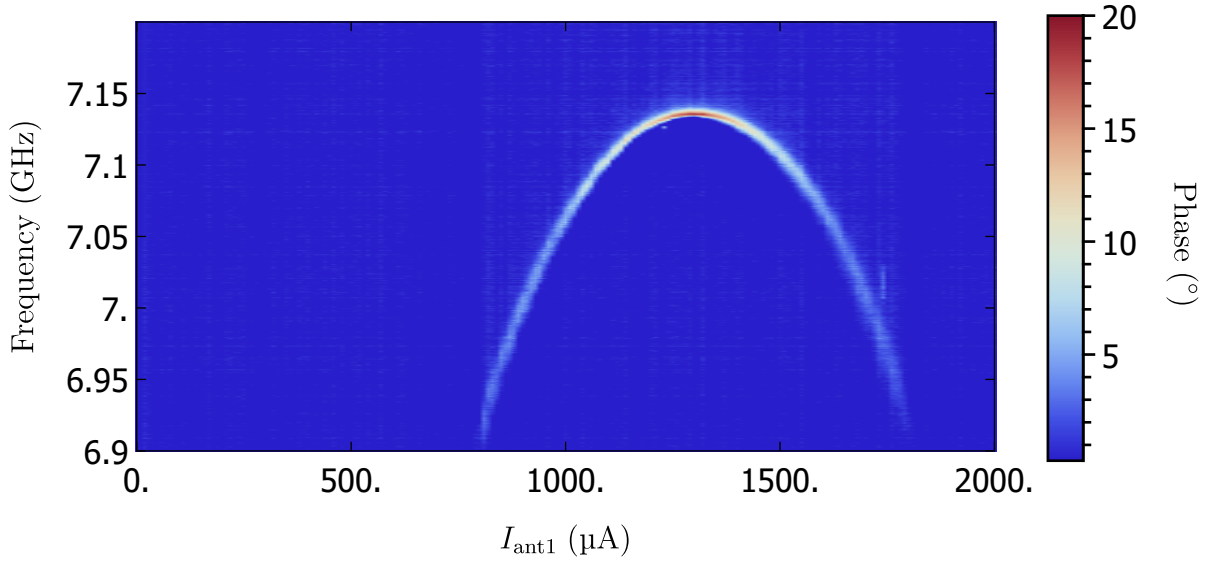

Figure 4.12: Measurement of the phase of S_{11} while sweeping the current of antenna 1. We can clearly observe the expected dependency of the resonance frequency of resonator 1 on the applied current. We create an external flux of $\Phi_{\mathrm{ext}} = 0.58\Phi_0$ in the SQUID loop by applying $I_{\mathrm{ant1}} = 1\,\mathrm{mA}$.

2 can be seen in the scattering parameter S_{22} shown in Fig. 4.13. Due to the coupling of resonator 1 to the parasitic path, we can still see its resonance in this reflection measurement, although it is less visible. In addition, we can also see the resonance of resonator 2, which is close to its maximal value at $I_{\mathrm{ant1}} = 0$. We observe a slight tuning of said mode, indicating a finite crosstalk between the magnetic field of antenna 1 and the SQUID loop of resonator 2. To better visualize the mode and this tuning, we overlay the theoretical model [Eq. (4.13)] onto the measurement. The tuning of resonator 2 is almost an order of magnitude smaller than the one for resonator 1. We find, that to create one Φ_0 of external flux in SQUID loop 2, we have to apply a current of $I_{\mathrm{ant1}} = 13.3\,\mathrm{mA}$.

Flux tuning and crosstalk using antenna 2

Next, we investigate the flux tuning of resonator 2 with antenna 2 and the resulting crosstalk on resonator 1. Fig. 4.14 shows the phase of the reflection measurement S_{22}. In this measurement, similar to the previous measurement, we observe both the desired control of resonator 2 and a crosstalk to resonator 1. A visual indication for the behavior of resonator 2 can be seen in the bottom panel. As expected from the symmetric design, the tuning rate for resonator 2, $0.59\ \Phi_0\mathrm{mA}^{-1}$, is similar to the one observed between antenna 1 and resonator 1 in the previous section. To tune the resonator by a full period, we therefore have to apply 1695 µA.

Surprisingly, the crosstalk between antenna 2 and resonator 1 is drastically different from the one between antenna 1 and resonator 2. As can be seen in the reflection

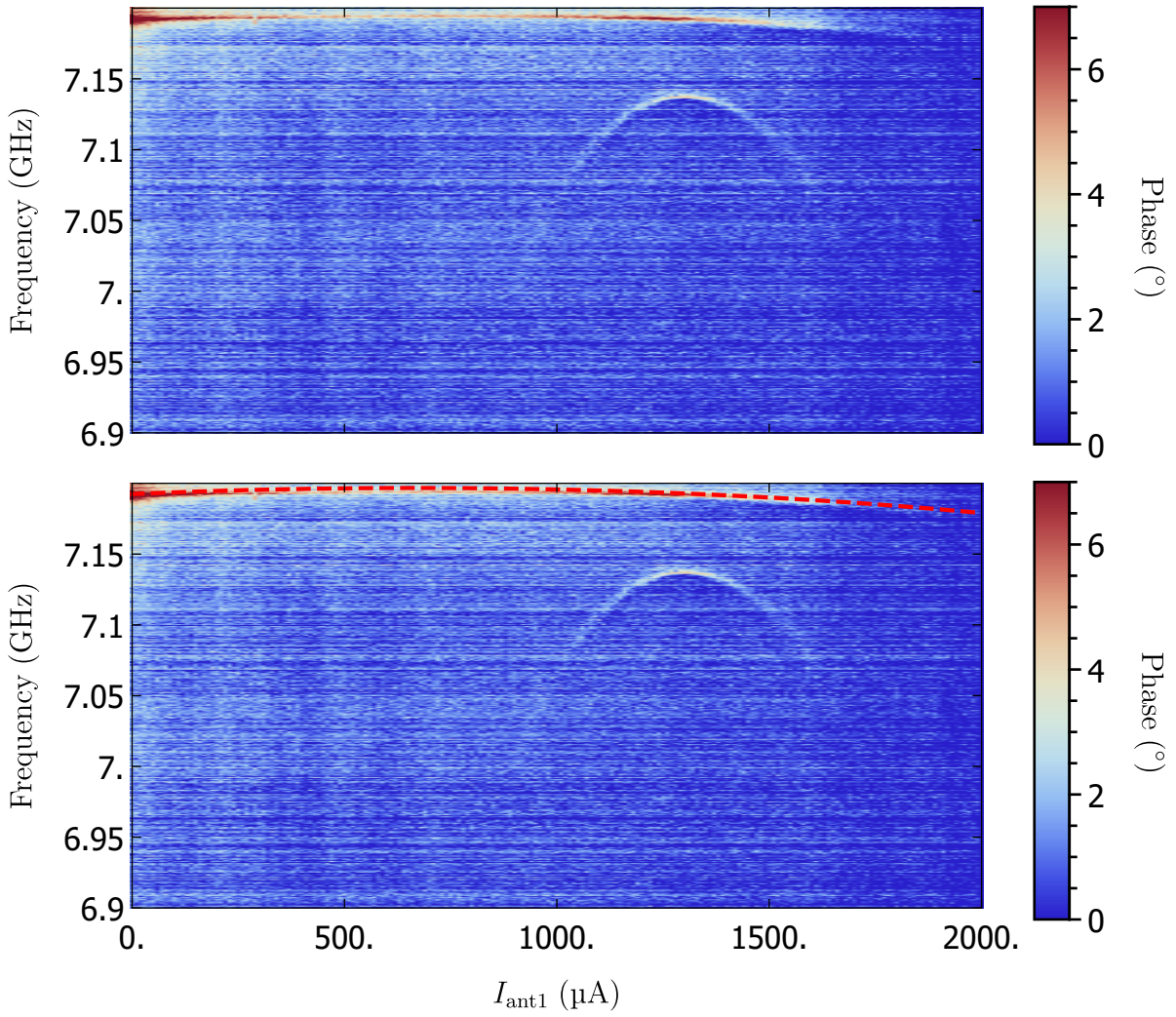

Figure 4.13: Measurement of the phase of S_{22} while sweeping the current of antenna 1. We find that we create an external flux of $\Phi_{\mathrm{ext}} = 0.075\Phi_0$ in the SQUID loop of resonator 2 by applying $I_{\mathrm{ant1}} = 1\,\mathrm{mA}$. The dashed line in the is the calculated resonance frequency using Eq. (4.13). In order to increase visibility, it is displayed in a separate panel.

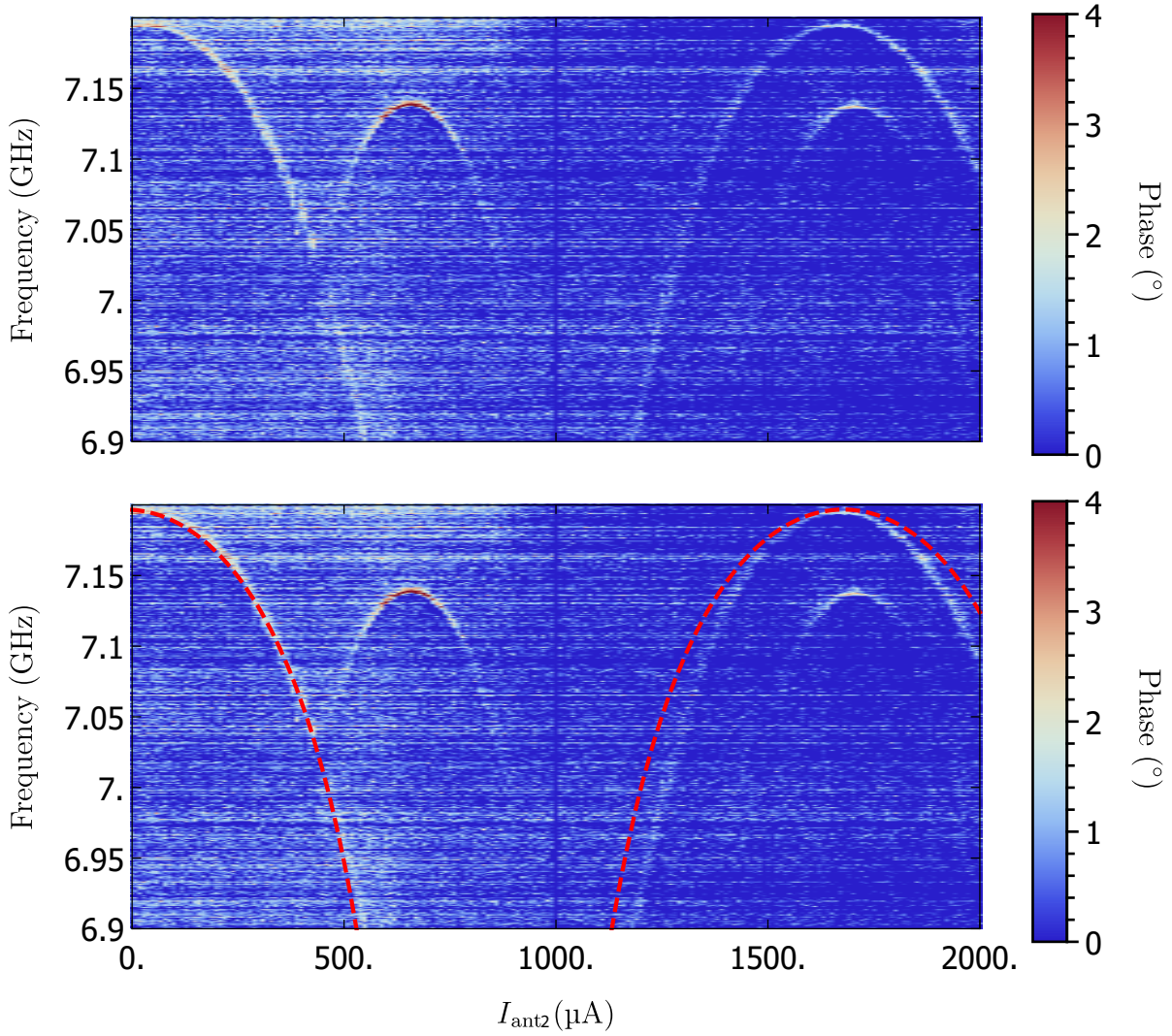

Figure 4.14: Measurement of the phase of S_{22} while sweeping the current of antenna 2. Similar to the measurement where we sweep I_{ant1}, we can see both the resonance frequency of resonator 1 and the one of resonator 2 being affected by antenna 1. We find that we create an external flux of $\Phi_{\mathrm{ext}} = 0.59\Phi_0$ in the SQUID loop of resonator 2 by applying $I_{\mathrm{ant2}} = 1\,\mathrm{mA}$. In order to increase visibility, it is displayed in a separate panel.

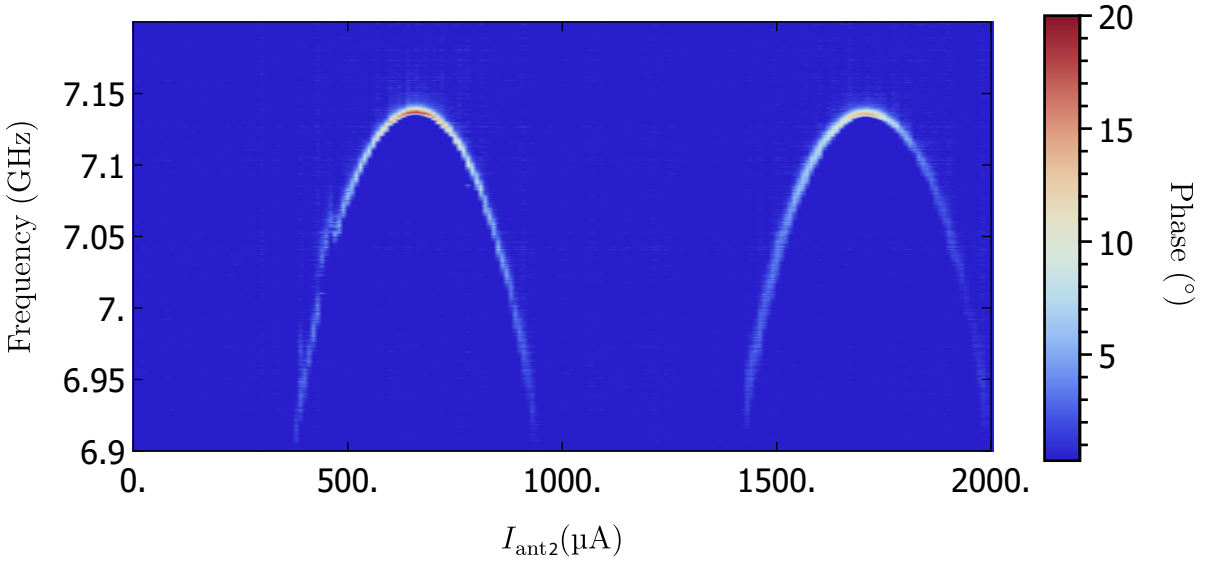

Figure 4.15: Measurement of the phase of S_{11} while sweeping the current of antenna 2. We can clearly observe the expected dependency of the resonance frequency of resonator 1 on the applied current. We create an external flux of $\Phi_{\mathrm{ext}} = 1.1\Phi_0$ in the SQUID loop by applying $I_{\mathrm{ant1}} = 1\,\mathrm{mA}$.

measurement S_{11} shown in Fig. 4.15, antenna 2 creates an even larger flux in the SQUID loop of resonator 1, than in resonator 2. We find, that a current of 909 µA is sufficient to create one flux quantum inside this SQUID loop. This result indicates that small deviations in the circuit symmetry, e.g., due to the wire bonds on the chip, can cause strongly asymmetric current flows and unexpected crosstalk. While such an effect may be difficult for future scaling, it can be easily compensated in our two-resonator sample.

Full control of the two-resonator system

The precise control of the resonators via the flux through their dc SQUID is of great importance for the two-resonator system. The flux through the SQUID defines the critical current and, in turn, both the resonance frequency and the nonlinearity of each resonator. As we have seen in the previous sections, individual control of both resonators requires the consideration of the effect of both on-chip antennas on both SQUID loops. In the experiment, we use a combination of on-chip antennas and the external coil to effectively control each resonator individually. We use Eq. (4.13) in order to calculate the resonance frequency of each resonator as a function of the external flux through each SQUID loop .

The two fluxes induced by the three currents we can apply are

$$\begin{aligned}\phi_1(I_{\text{ant1}}, I_{\text{ant2}}, I_{\text{coil}}) = M_{\text{ant1, 1}} \cdot I_{\text{ant1}} + M_{\text{ant2, 1}} \cdot I_{\text{ant2}} \\ + M_{\text{coil, 1}} \cdot I_{\text{coil}} + \Delta\phi_1\end{aligned} \tag{4.14}$$

$$\begin{aligned}\phi_2(I_{\text{ant1}}, I_{\text{ant2}}, I_{\text{coil}}) = M_{\text{ant1, 2}} \cdot I_{\text{ant1}} + M_{\text{ant2, 2}} \cdot I_{\text{ant2}} \\ + M_{\text{coil, 2}} \cdot I_{\text{coil}} + \Delta\phi_2.\end{aligned} \tag{4.15}$$

Here, $M_{\text{ant } i/\text{coil, } j}$ is the mutual inductance between antenna i / coil and SQUID loop j. The parameters extracted from our data can be found in tables 4.4 and 4.2. Based on these tables we are able to calculate the possible currents we have to apply in order to set each resonator to a specific frequency. As the three currents are only determined by two independent equations, we are able to choose one current independently. In this way, we can overcome the issue of non ideal SQUID characteristics (see Fig. 4.10 and Fig. 4.14). For more details please refer to [68].

In order to implement this full control in an experiment, we pre-calculate the current values for the frequency points we want to set and than automatically set the current values of the coil and both antennas one after another.

4.3.3 Coupling strength J between the two resonators

The coupling strength between the two resonators is, alongside the nonlinearity of the system, one of the main deciding parameters for the physics of the bosonic excitations in the lattice. In the Bose-Hubbard model, the ratio between nonlinearity and the coupling strength define whether the system is in its superfluid or mott-insulating state. For future applications it is therefore necessary, to be able to design, predict and determine this parameter J. Here, we present two possibilities to extract J from our measurements. First, we can directly measure it, as half the smallest distance in frequency between the two modes at their point of degeneracy. Here, the two separate modes couple and form two coupled modes, that are shifted by $\pm J/2\pi$ from the uncoupled modes (see section 2.1.3).

In Fig. 4.16, we show a transmission measurement where we tune both resonators into resonance. As expected, we observe an avoided crossing of the two resonator modes. The difference between the two modes is given by

$$\Delta f = \sqrt{4J^2 + \Delta^2}, \tag{4.16}$$

with Δ being the detuning of the uncoupled modes. For $\Delta = 0$ the splitting becomes minimal, and we can directly extract the coupling from the measurement. We measure the distance between the two modes at a current of 9.12 µA, which is the current that creates the smallest splitting. Along with two other cuts at 8.98 µA and 9.22 µA, this slice is shown in Fig. 4.17. We find a minimal splitting of $\Delta f = 17.2$ MHz, which gives us a

coupling strength of $J/2\pi = 8.6\,\mathrm{MHz}$.

Although the coupling capacitor is independent of the flux bias we apply to the SQUID loops, the actual coupling strength is flux dependent. This is due to the fact, that the coupling strength depends on the resonance frequency of the resonator and on the ratio between the coupling capacitance and the effective capacitance of the resonators. As already presented in previous sections, the latter changes with the applied flux, which in turn creates a dependency for the coupling strength. As it is very time consuming to perform a full characterization of J, where we create the degeneracy point at all possible frequencies, we present a second way in order to estimate the coupling strength. Using the Lagrangian of the system, we can calculate the coupling strength from the circuit model, we used for the simulations of the system

$$J = \omega_\mathrm{r} \frac{C_\mathrm{c}}{C_\mathrm{i}}. \tag{4.17}$$

As we look at points where the two resonators are in resonance, we can use both the capacitance C_i of resonator 1 and 2 here. We plot the results for the coupling strength for the flux dependence of resonator 1 in Fig. 4.18. We get a coupling strength J of 5.02 MHz to 8.76 MHz. Note that the actual possible minimal coupling is limited by the tunability of resonator 2, and is therefore only 5.38 MHz. The measured coupling strength of 8.6 MHz near the maximal frequency of resonator 1 fits well to the theoretically calculated results. We conclude, that although the coupling strength between the two resonators depends on the resonance frequency, the actual change of around 40 % is quite low as compared to the change in nonlinearity. We will discuss this in further detail after we introduced the measurement and calculation of the nonlinearity in Sec. 5.1.2.

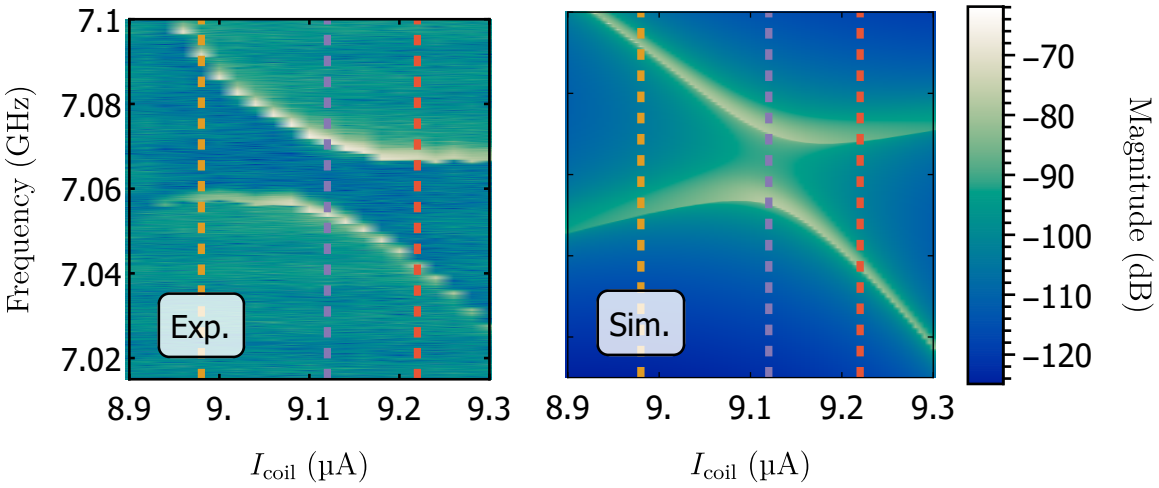

Figure 4.16: Measurement (left panel) and simulation (right panel) of a transmission measurement near the degeneracy point of the two resonators. Dashed colored lines show the position of cuts shown in Fig. 4.17.

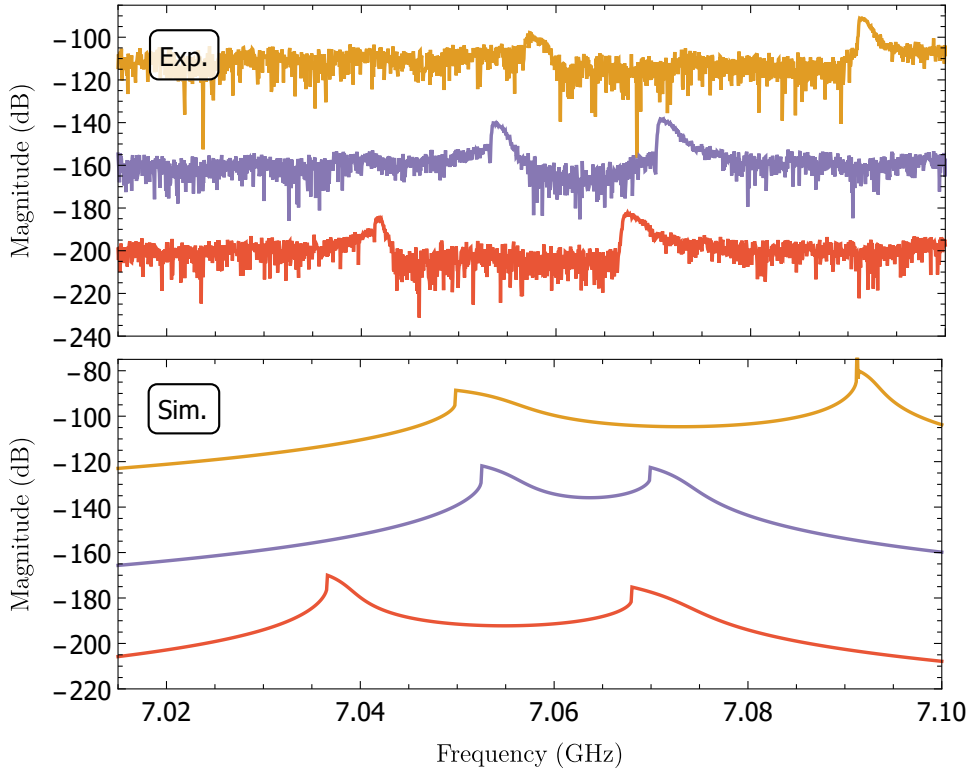

Figure 4.17: Cuts of the measurement (top panel) and simulation (bottom panel) of a transmission measurement near the degeneracy point of the two resonators. The shown cuts are visible as lines in the picture of the full measurement in Fig. 4.16. The current values are 8.98 µA (yellow), 9.12 µA (purple) and 9.22 µA (red). From the purple graph we can extract a coupling strength of $J/2\pi = 8.6$ MHz.

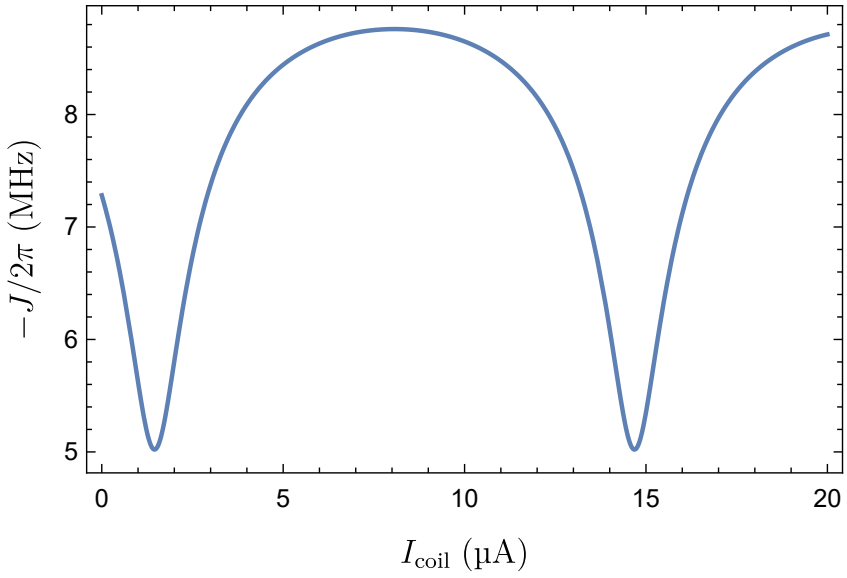

Figure 4.18: Calculation of the coupling strength J with the flux dependence of resonator 1. We find a maximal coupling strength of 8.76 MHz and a minimal one of 5.02 MHz

Chapter 5

In situ tunable nonlinearity and competing signal paths in coupled superconducting resonators

In Sec. 2.1.7, we discuss how to set up a circuit model for the characterization of a nonlinear two-resonator system in the presence of a spurious environment whose microscopic origin does not need to be exactly known. In this section, we show that this environment can be modeled with a spurious parallel signal path giving rise to Fano-like resonances. In this way, we gain access to the full parameter space of the coupled systems in a controlled way. Consequently, we can investigate a key property of our system: the nonlinearity of the resonators. Specifically, we employ two different characterization techniques including a direct measurement. We show that the nonlinearity of our resonators can be tuned *in situ* from values much smaller to values larger than the resonator-resonator coupling. In this way, we provide a technique for a controlled access to promising parameter regimes for future quantum simulations. For additional reading, please also refer to [69]. As additional preparation for the future quantum simulation experiments, we perform first tests of our correlation function measurement setup and show that we are able to detect the second-order correlation function of a coherent signal.

5.1 Nonlinearity from the circuit model

In the scope of a quantum simulation experiment, it is vital to know the full parameter set of the underlying circuit in order to precisely predict its behavior. For a system of nonlinear resonators, the nonlinearity is of key interest. We therefore implement two ways to experimentally determine the nonlinearity of our system. In the following, we present a circuit model accurately reproducing our data (see Sec. 5.1.1), which allows us to calculate the nonlinearity (see Sec. 5.1.2). In Sec. 5.2.2, we compare these results to a direct measurement of the nonlinearity based on the power-dependent response of the resonators.

5.1.1 Circuit model with competing signal path

In the experiment, we measure the transmission S_{ca} or S_{21} through our two-resonator system as a function of the current I_{coil} through the coil and of the frequency $\omega_{\mathrm{d}}/2\pi$ of the applied microwave drive. The result is shown in Fig. 5.1(a). As expected, we observe periodic modulations of the two resonance frequencies of the coupled resonators. The maximum resonance frequencies of the two resonators differ by approximately 50 MHz due to inaccuracies in the junction fabrication.

In order to extract the circuits parameters, we first simulate the response of the sample with a simple circuit model taking into account only the resonators and coupling capacitors (see Fig. 2.9). Details of the simulation can be found in Sec. 2.1.7. The simple circuit model predicts an increased transmission in regions where the resonators are close to resonance and a strongly suppressed transmission elsewhere [see Fig. 5.1(a, orange line)]. Comparing the experimental data to the results of the simulation, we find good agreement when the two resonators are close to resonance with each other, but significant differences otherwise. For example, in the experiment, there is a clear transmission signal of resonator 1 even if resonator 2 is far detuned. The model, on the other hand, predicts a strong damping of the resonance of resonator 2 in this regime. These observations become even more apparent when we look at the transmission signal for certain fixed coil currents. As shown by Fig. 5.2(a, orange line), the simple model can reproduce the measured resonances qualitatively well, despite the fact that the measurement shows a larger background signal. In contrast, Fig. 5.2(b, orange line) shows that, when the two resonators are far detuned, the transmission through the system is predicted to be strongly damped over the whole frequency range. Even on resonance the measured peak is approximately 15 dB higher than predicted.

We can account for these deviations by introducing a generic environment in form of a parasitic signal path (see Fig. 2.9). This parasitic path consists of a series connection of resistive, inductive, and capacitive elements. They are coupled capacitively to the input and output lines and also inductively to the resonators. As shown in Fig. 5.1, the model that includes this parasitic path (see Sec. 2.1.7 for detailed calculations) reproduces the experimental data very well over the whole frequency range. The reason for this significant improvement is the fact that the parasitic path opens up additional transmission channels for the system. First of all, the signal can be directly coupled into the parasitic path via the input line and then be transmitted to the output line leading to an increased constant background even if both resonators are far detuned from the input frequency. Secondly, if the signal is in resonance with resonator 1, it can enter the resonator and then couple inductively to the parasitic path. This can be seen by the increased signal at the resonance frequency of resonator 1 even where resonator 2 is detuned.

Turning back to the frequency-dependent transmission at fixed coil current values, we can clearly distinguish between regions, where the path through the resonator system dominates, and regions, where the parasitic path plays a crucial role. In Fig. 5.2(a), the

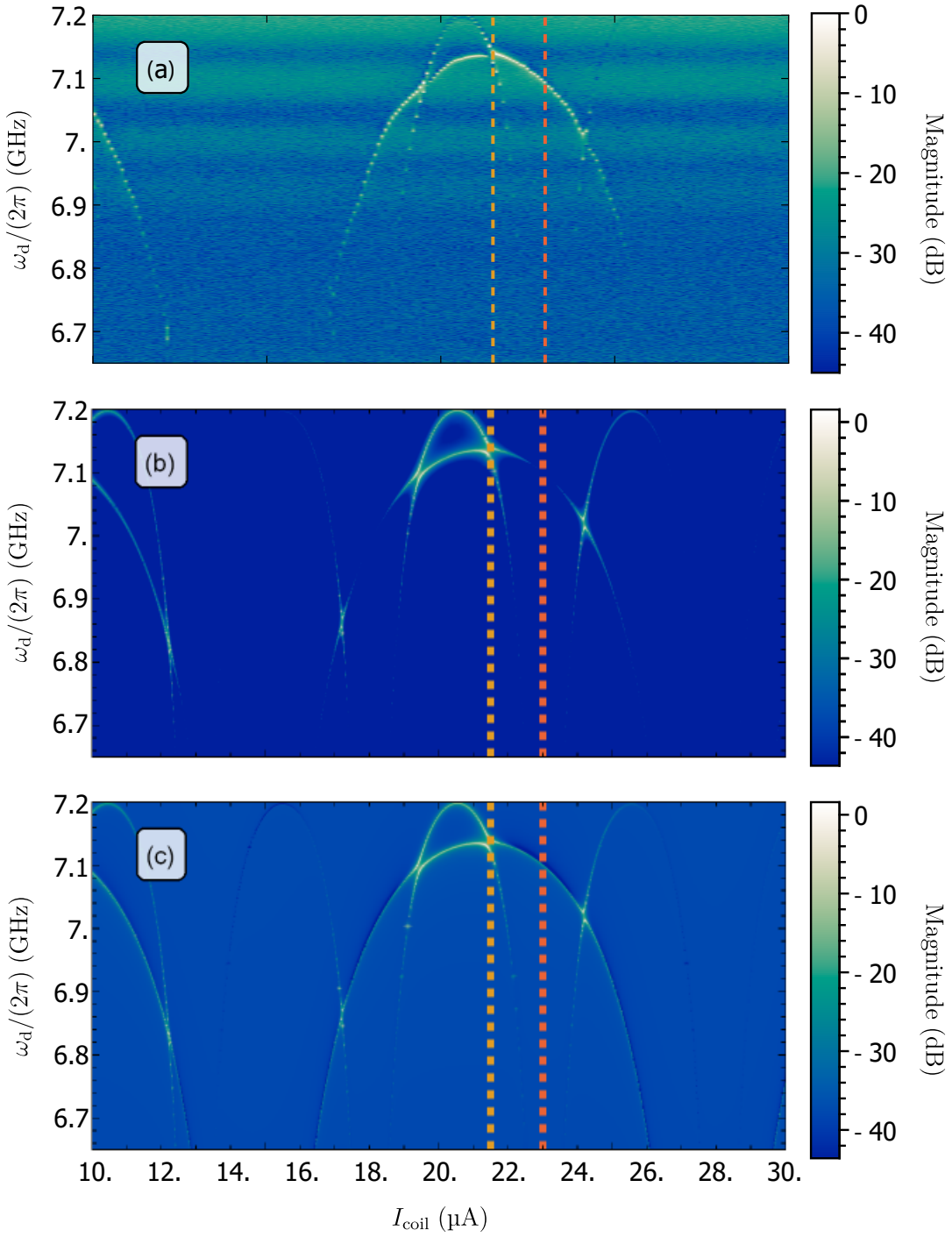

Figure 5.1: Normalized transmission magnitude (S_{ca} (VNA ports) or S_{21} (sample ports)) through the sample as a function of the coil current and the probe frequency. (a) Measurement using the setup shown in Fig. 4.3 with an input power of $P_{in} = -30\,\mathrm{dBm}$. (b) Simulation only considering the resonators and coupling capacitors. (c) Simulation taking into account a parasitic path. Data profiles at working points indicated by the dashed lines are displayed in Fig. 5.2. Parameters used in the simulations are shown in Tab. 4.2 and Tab. 5.2.

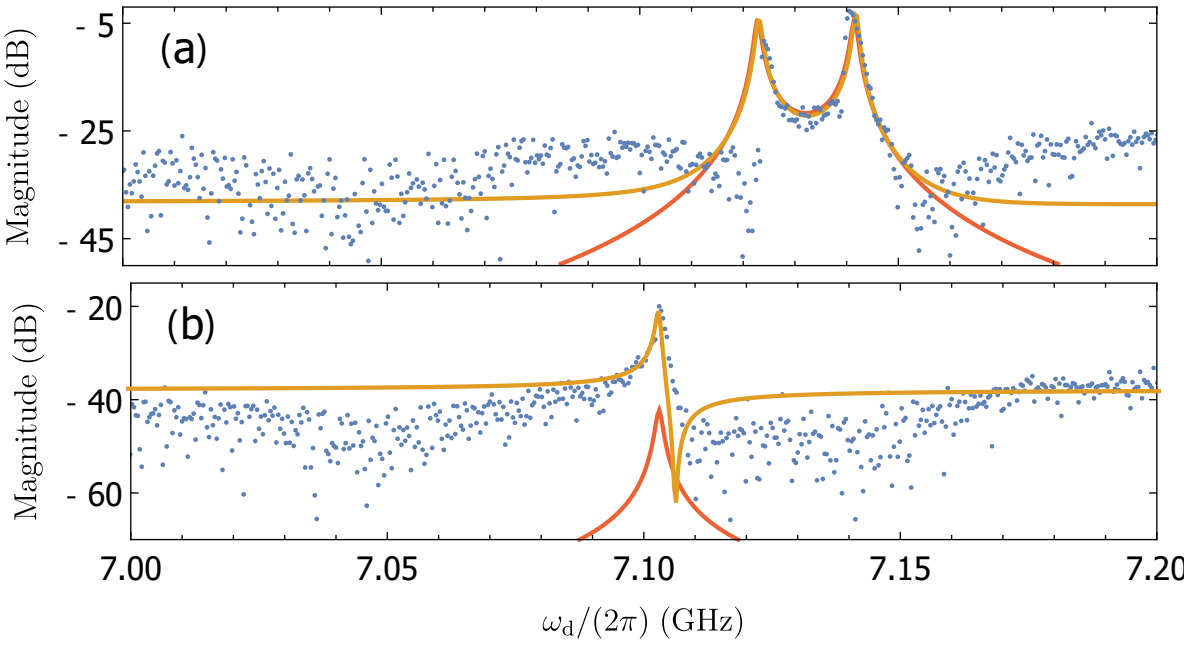

Figure 5.2: Measured transmission magnitude S_{ca} or S_{21} (blue dots) as a function of the probe frequency for two fixed coil currents with input power $P_{in} = -30\,\mathrm{dBm}$. (a) Both resonators in resonance, $I_{coil} = 21.5\,\mu\mathrm{A}$. solid yellow line: fit based on parasitic path model, solid orange line: fit based on simple model. (b) Resonator 2 far detuned ($\omega_{r,2} = 5.7\,\mathrm{GHz}$), $I_{coil} = 23.0\,\mu\mathrm{A}$. Solid yellow line: fit based on parasitic path model, solid orange line: fit based on simple model.

two resonators have similar resonance frequencies and therefore transmit most of the signal to the output port. Hence, the parasitic path does not contribute to the shape of the resonances. Away from the resonances, the broadband nature of the parasitic path allows for an increased transmission background as it is observed in the measurements. When the two resonators are far detuned, the presence of the parasitic path also changes the qualitative shape of the resonance, making it Fano-like. While the peaks are symmetric in the simple model at all times [see Fig. 5.2(b, orange line)], the parasitic path model matches the peak-dip feature of the measurement [Fig. 5.2(b, yellow line)]. In summary, based on the parasitic path model, we obtain a realistic set of parameters for each resonator (see Tab. 4.2 and Tab. 5.2). Additionally, we calculate the capacitance per unit length $C_0 = 0.18\,\mathrm{nF\,m^{-1}}$ and the inductance per unit length $L_0 = 0.44\,\mu\mathrm{H\,m^{-1}}$ of the resonators from their bare resonance frequency. Our simulations have shown, that both capacitive and inductive coupling are necessary in order to correctly model the experimental results. For definitions and further explanations regarding these parameters, please refer to Sec. 2.1.7.

5.1.2 Calculation of the nonlinearity from the circuit model

Using the parameters extracted from the parasitic-path model discussed in the previous section, we can estimate the nonlinearity U created by the SQUID for a single half-

	$I_c(\mu A)$	$\delta\Phi(\Phi_0)$	$\Delta\Phi/\Delta I_{coil}(\Phi_0 \mu A^{-1})$	d	$k_L(10^{-3})$
Res 1	1.56	-0.39	0.076	0.13	8
Res 2	1.80	0.30	0.180	0.13	0.75

Table 5.1: Resonator parameters extracted from the circuit model. For each resonator, we show the total critical current $I_c = I_{c1} + I_{c2}$ of the SQUID, the zero current offset $\delta\Phi$ of the flux through the SQUID loop, the flux change $\Delta\Phi$ per applied coil current ΔI_{coil}, the SQUID asymmetry parameter d, and the inductive coupling constant k_L to the parasitic path. For better readability, the index i representing each resonator has been omitted in this table.

C_p(fF)	$R_p(\Omega)$	L_p(nH)
6.2	8000	133

Table 5.2: Parameters of the parasitic path (see Fig. 2.9). Here, we show the capacitance C_p, resistance R_p and inductance L_p of the parasitic path.

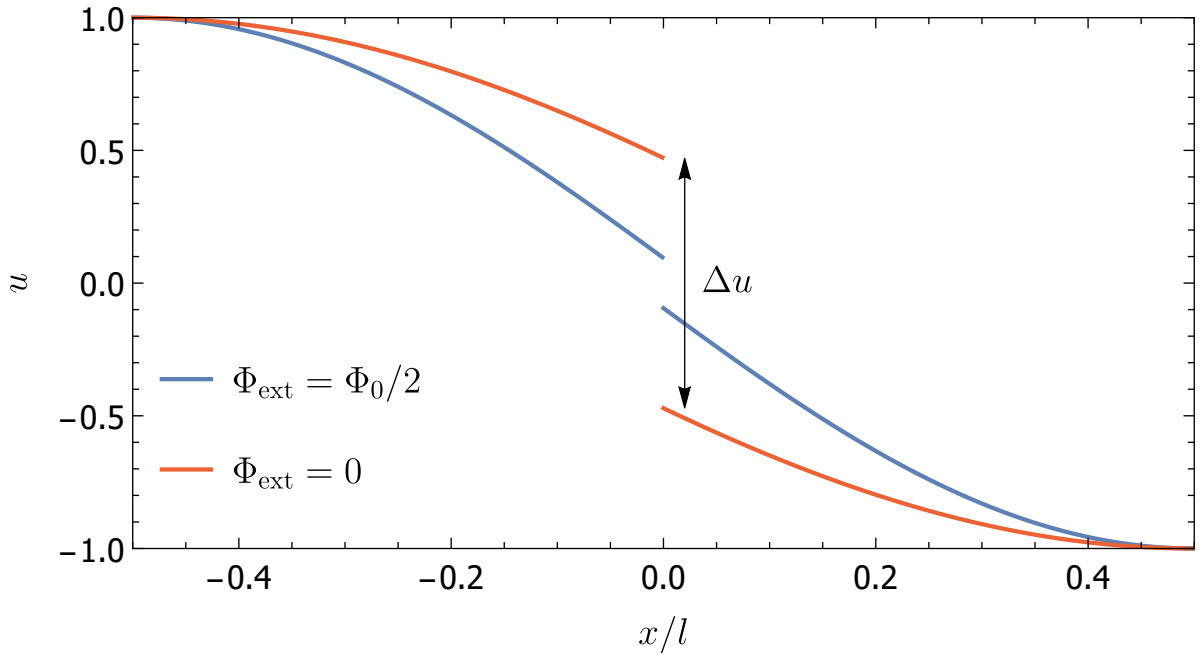

Figure 5.3: Dimensionless envelope u of the first spatial voltage mode at $\Phi_{ext} = 0$ and $\Phi_{ext} = \Phi_0/2$ of a resonator of length l with a SQUID at position $x = 0$. The difference of the spatial mode across the SQUID, Δu, is a direct measure of the nonlinearity of the resonator.

wavelength coplanar waveguide resonator following Ref. [49] via the relation

$$U = -\frac{e^2}{2\hbar L_\mathrm{J}} \frac{L\Delta u^4}{C}. \tag{5.1}$$

Here, the parameters C and L are the effective capacitance and inductance of the resonator including the contribution from the SQUID. We numerically calculate Δu, which is the difference of the dimensionless spatial voltage mode envelope u of the first resonator mode across the point-like SQUID (see Fig. 5.3 for details). For a detailed derivation, see Sec. 2.1.6.

For our two resonators, the dependence of U as a function of I_coil is shown in Fig. 5.4. The absolute value of the nonlinearity of resonator 1 (2) can be tuned between a minimum of 0.1 MHz (0.06 MHz) and a maximum of 8.0 MHz (6.1 MHz). Due to the difference in the maximal critical currents of the two dc SQUIDs, the tuning ranges for the nonlinearity differ slightly. Nonetheless, they extend over almost two orders of magnitude. This fact allows us to set the nonlinearity U *in situ* between values well below the resonator-resonator coupling rate $J = 8.6 \pm 0.3$ MHz and values well above J by changing the magnetic bias fields. J is extracted from the level splitting at the frequency degeneracy point of the two resonators. For more details, see Sec. 4.3.3. As J is also dependent on the flux through the SQUIDs, we plot both U and J against the coil current I_coil using the parameters found in Tab. 5.1. We can clearly observe the two regions where $J > U$ and vice versa.

5.2 Nonlinearity from a direct power-dependent measurement

In addition to the values extracted from the circuit model in the previous section, we present a direct measurement of the nonlinearity of resonator 2. Specifically, we exploit the response of the resonance frequency as a function of the input power. The relevant parameter to determine U is the actual power circulating inside the resonator. Therefore, we first have to extract the external coupling strength between resonator and transmission line to convert the applied power to the field strength inside the resonator.

5.2.1 Quality factor

In order to extract the quality factor of our system, we use an input output formalism [53] and fit the transmission and reflection of the two resonator chain. For the output signals

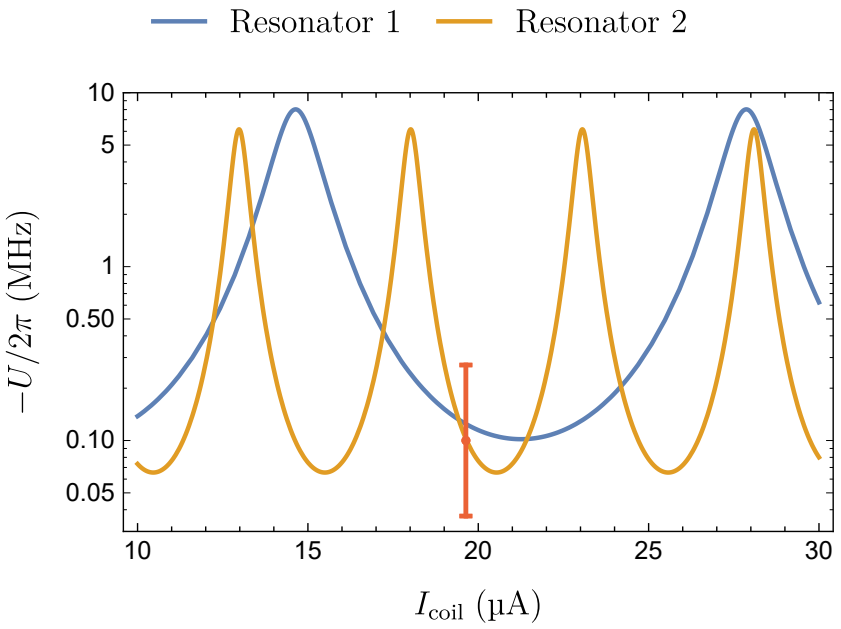

Figure 5.4: The nonlinearity U as a function of the current flowing through the external coil. Solid lines represent calculations based on parameters extracted from transmission data and parasitic-path model for resonator 1 (blue) and resonator 2 (yellow). The red dot is the result of a direct measurement for resonator 2 described in Sec. 5.2.2.

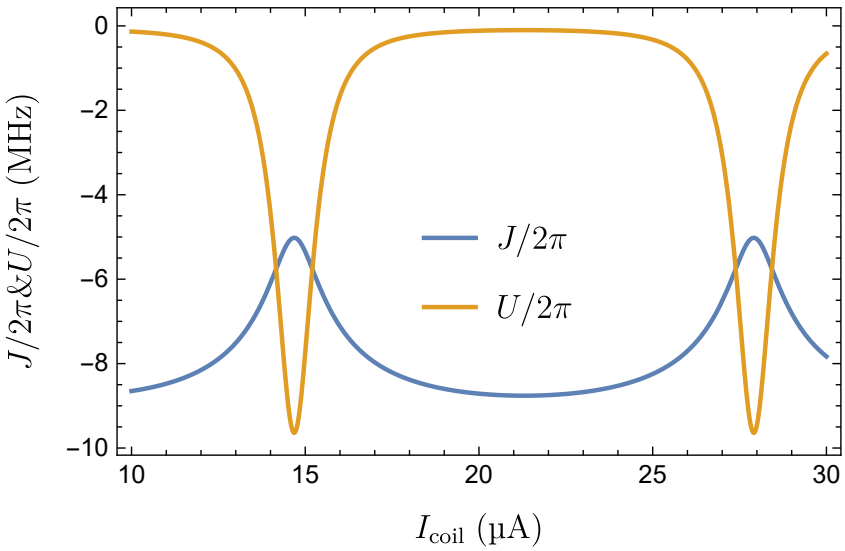

Figure 5.5: Comparison of the calculated values of the nonlinearity U and the coupling strength J. The nonlinearity can be tuned by almost two orders of magnitude. There are regions where $U > J$ and vice versa.

of resonator 1 (a_{OUT}) and resonator 2 (c_{OUT}) we get

$$c_{\mathrm{OUT}} = \frac{\sqrt{\kappa_{\mathrm{ext}}\kappa_{\mathrm{c}}}b_{\mathrm{right}} + \left(\frac{\kappa_{\mathrm{c}}-\kappa_{\mathrm{ext}}}{2} - i\left(\omega-\omega_0\right)\right)c_{\mathrm{IN}}}{\frac{\kappa_{\mathrm{ext}}+\kappa_{\mathrm{c}}}{2} - i\left(\omega-\omega_0\right)} \tag{5.2}$$

$$a_{\mathrm{OUT}} = \frac{\sqrt{\kappa_{\mathrm{ext}}\kappa_{\mathrm{c}}}b_{\mathrm{left}} + \left(\frac{\kappa_{\mathrm{c}}-\kappa_{\mathrm{ext}}}{2} - i\left(\omega-\omega_0\right)\right)a_{\mathrm{IN}}}{\frac{\kappa_{\mathrm{ext}}+\kappa_{\mathrm{c}}}{2} - i\left(\omega-\omega_0\right)}, \tag{5.3}$$

where b_{left} and b_{right} are the signals flowing over the coupling capacitor. κ_{ext} is the coupling rate to the feed lines and κ_{c} the coupling rate between the two resonators. Further information on the derivation of these equations and how we solve them can be found in section 2.1.3. We use the solution we get for a_{OUT} to fit the theoretically calculated magnitude of the S-Parameter (Fig. 5.6)

$$\mathrm{Mag}(S_{11}) = A\left|a_{\mathrm{OUT}}\right|^2 + c_{\mathrm{off}}, \quad \text{with} \tag{5.4}$$

$$a_{\mathrm{IN}} = 1 \quad \text{and} \quad c_{\mathrm{IN}} = 0 \tag{5.5}$$

to our measured data. We use the factor A to account for cable damping and the constant c_{off} to account for background noise. Note that, we use a calibrated measurement, where we subtracted the background from a measurement, where the resonators are detuned from the region of interest. From the fit we extract $\kappa_{\mathrm{ext}}/2\pi = 1.75\,\mathrm{MHz}$ and $\kappa_{\mathrm{c}}/2\pi = 15.24\,\mathrm{MHz}$. We calculate a quality factor $Q = 4045.6$ and a coupling strength $J = 7.62\,\mathrm{MHz}$. The input output method we use here, allows us only to investigate the points of avoided crossing, as it assumes that the two resonators are in resonance. In addition to this, it does not include the influence on the environment and is therefore only useful when we describe regions, where the signal flow through the resonators dominate over the background contributions. In order to account for these additional contributions, we can model the resonances with a Fano like description. We introduced the difference between a standard Lorentzian line shape and a Fano line shape in section 2.1.8. In this model, the Fano parameter q is the defining parameter for the shape of the resonance. q is in turn defined by the participation of the continuum of background modes. We now look at two different resonance frequencies of resonator 2. The full measurement from where we extracted the following data can be seen in Fig. 5.1. We choose coil currents of 6.6 µA (Fig. 5.7, left panel) and 8.1 µA (Fig. 5.7, right panel). We can see, that the two line shapes are very different, the one at a lower resonance frequency being a asymmetric dip feature, while the one close to maximum resonance frequency of resonator 2 being a dip feature. We can fit the resonances with the model of a Fano resonance (Eq. 2.67), and are able to find solutions that fit the line shape well. The Fano parameter q is different for the two fits, which indicates a different participation ratio of the background. We get $q_{\mathrm{left}} = -2.68$ and $q_{\mathrm{right}} = 0.6$. In the simulations we perform, the shape of the measured resonances near the frequency maximum of resonator 2 are not reproduced well. The simulation

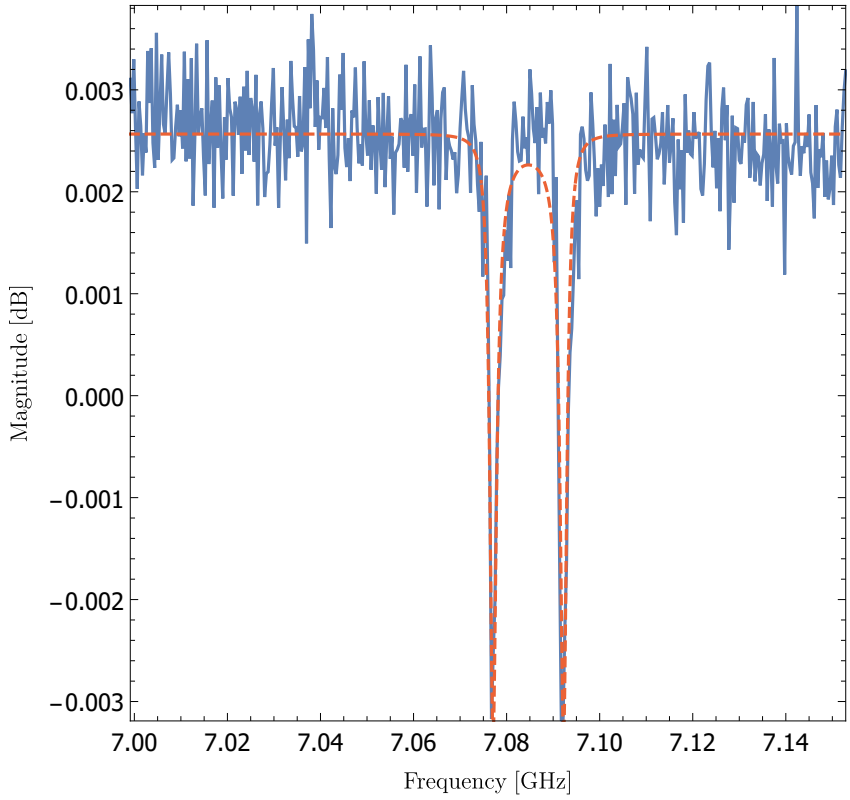

Figure 5.6: A fit calculated from the Input-Output-Formalism (red) to the measured magnitude of a reflection measurement (blue).

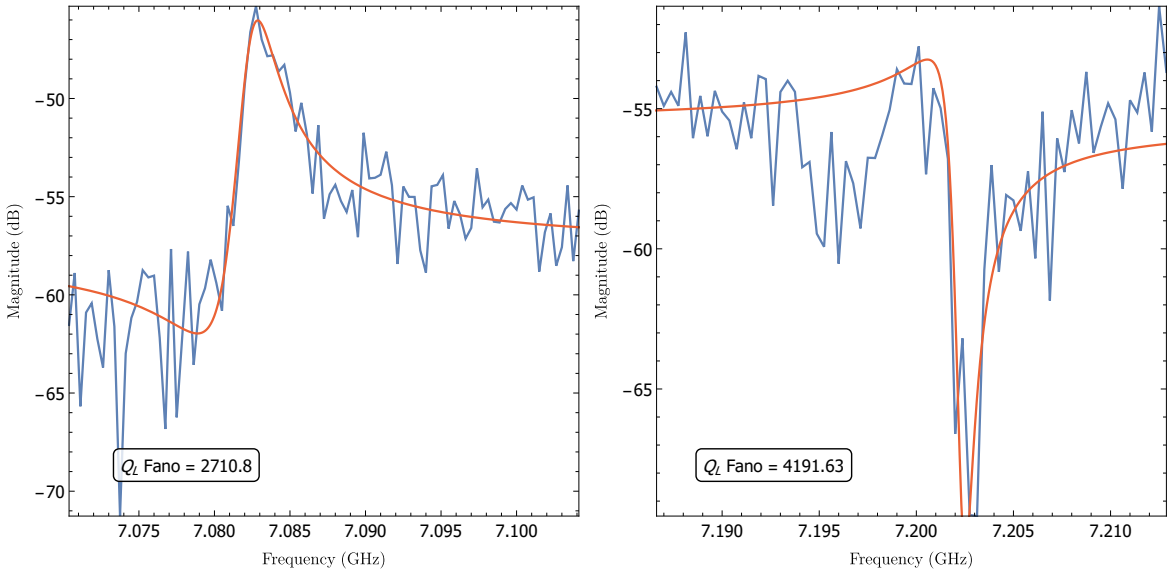

Figure 5.7: Measurements (blue) of two resonances of resonator 2 at coil currents of 6.6 µA (left panel) and 8.1 µA(right panel). Fits with a Fano model are shown in red. The fits produce different Fano parameters $q = -2.68$ (left) and $q = 0.6$ (right).

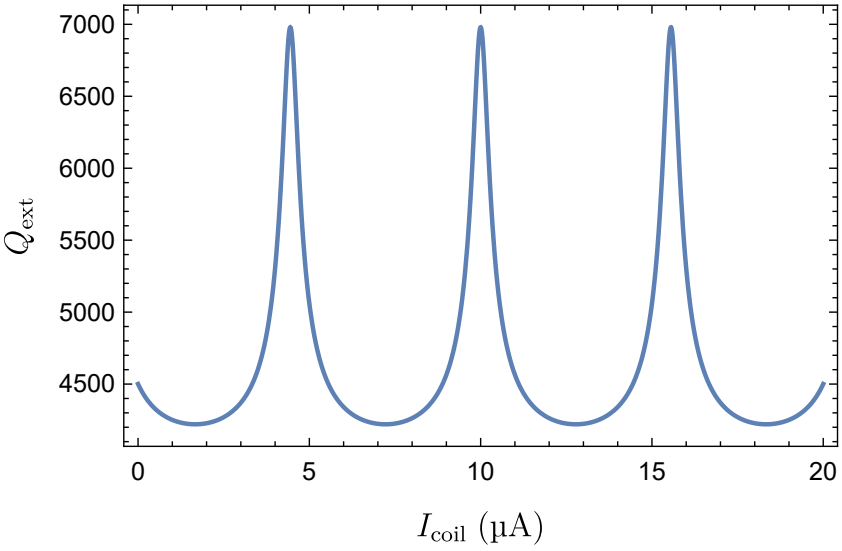

Figure 5.8: Theoretical calculation of the external quality factor of resonator 2.

predicts a peak feature, while we observe a dip in the measurement. The simulation uses a single background contribution which leads to an almost flat continuum distribution. In the measurement, the background actually changes quite drastically over the whole frequency range, especially showing a large increase towards higher frequencies. This leads to stronger contribution of said background, which can be seen in the lower Fano parameter in the fit of this resonance. We extract a loaded quality factor of $Q_{\mathrm{loaded},1} = 2710.8$ for resonator 1 and $Q_{\mathrm{loaded},2} = 4191.6$ for resonator 2, each measured near their respective maximal frequency. The theory predicts an inverse correlation of the quality factor with resonance frequency as can be seen in Fig. 5.8. Here we used results of the circuit model to estimate the dependence of the quality factor on the coil current as

$$Q = \frac{\omega_r C_2}{2}\left(\frac{1+(\omega C_{\mathrm{io}} Z_0)^2}{(\omega_r C_{\mathrm{io}})^2 Z_0}\right). \tag{5.6}$$

The calculation matches both the quality factor we extracted with the Fano fit from resonator 2 and the one we got from the input output formalism. The lower quality factor of resonator 1 can not be explained by this model. A possible reason for the result is the power dependence of the resonator. As the participation ratio of the background is lower for this resonance point, more power is transmitted to the resonator. Due to the nonlinearity of the system, a higher input power broadens the resonance shape. This is reinforced by the fact that the nonlinearity is stronger for lower resonant frequencies. As the Fano model does not take these effects into account, it determines a lower quality factor. We therefore have to be careful that for the estimation of the quality factor, we use only measurements, that are performed with such low input power that the nonlinearity does not play a significant role.

External quality factor

In order to extract the external quality factor of our resonators, we use an input-output formalism [53] and fit the result to the measured reflection signal of the two-resonator chain. In the limit where resonator 1 is far detuned, we find a dependency of the scattering parameter S_{22} on the quality factors of resonator 2,

$$S_{22} \approx 1 - \frac{2Q_{\ell,2}/Q_{\mathrm{ext},2}}{1 - 2iQ_{\ell,2}\left(\omega_{\mathrm{r},2} - \omega_{\mathrm{d}}\right)}. \tag{5.7}$$

Here, we have used the loaded quality factor $Q_{\mathrm{l},2}$, the external quality factor $Q_{\mathrm{ext},2}$ and the resonance frequency $\omega_{\mathrm{r},2}$, each of resonator 2. The parameter ω_{d} denotes the angular frequency of the driving field. On resonance of the second resonator, $\omega_{\mathrm{r},2} - \omega_{\mathrm{d}} = 0$, Eq. (5.7) further simplifies to

$$S_{22} \approx 1 - \frac{2Q_{\ell,2}}{Q_{\mathrm{ext},2}}. \tag{5.8}$$

Further information on the derivation of these equations can be found in App. A. We first fit the predicted phase dependence, $\theta = \theta_0 + 2\arctan(2Q_{\ell,2}(1 - \omega/\omega_{\mathrm{r},2}))$, to the measured scattering parameter data to extract the loaded quality factor. Then, we fit Eq. (5.7) to the magnitude and use Eq. (5.8) to determine the external quality factor (see Fig. 5.9). For resonator 2, we obtain an external quality factor of $Q_{\mathrm{ext},2} = 1.35 \cdot 10^5$.

5.2.2 Nonlinearity from power-dependent resonance amplitude

In order to get a relation between the directly measurable output voltage of our system and the nonlinearity, we start with the equation of motion for a single resonator driven with a strength of F_0. It can be written in terms of the flux $\Psi = \int V(x,t)\mathrm{d}t$, where $V(x,t)$ is the internal voltage of the resonator,

$$\frac{\Psi}{L} + C\ddot{\Psi} + \frac{\dot{\Psi}}{R} + \beta\Psi^3 = F_0 e^{i\omega t}. \tag{5.9}$$

Here,

$$\beta = -\frac{1}{24}\left(\frac{2\pi}{\Phi_0}\right)^2 \frac{\Delta u^4}{L_{\mathrm{J}}} \tag{5.10}$$

is the prefactor of the nonlinear term due to the tunable Josephson junction formed by the SQUID. The parameter β depends on the SQUID inductance L_{J} and the drop Δu in the spatial voltage mode across the SQUID (see also Fig. 5.3). Obviously, the prefactor β is a direct measure for the nonlinearity of the system.

For the Duffing-like equation of motion, we can show that the maximum amplitude a of the mode is inversely proportional to the nonlinearity for small deviations from the

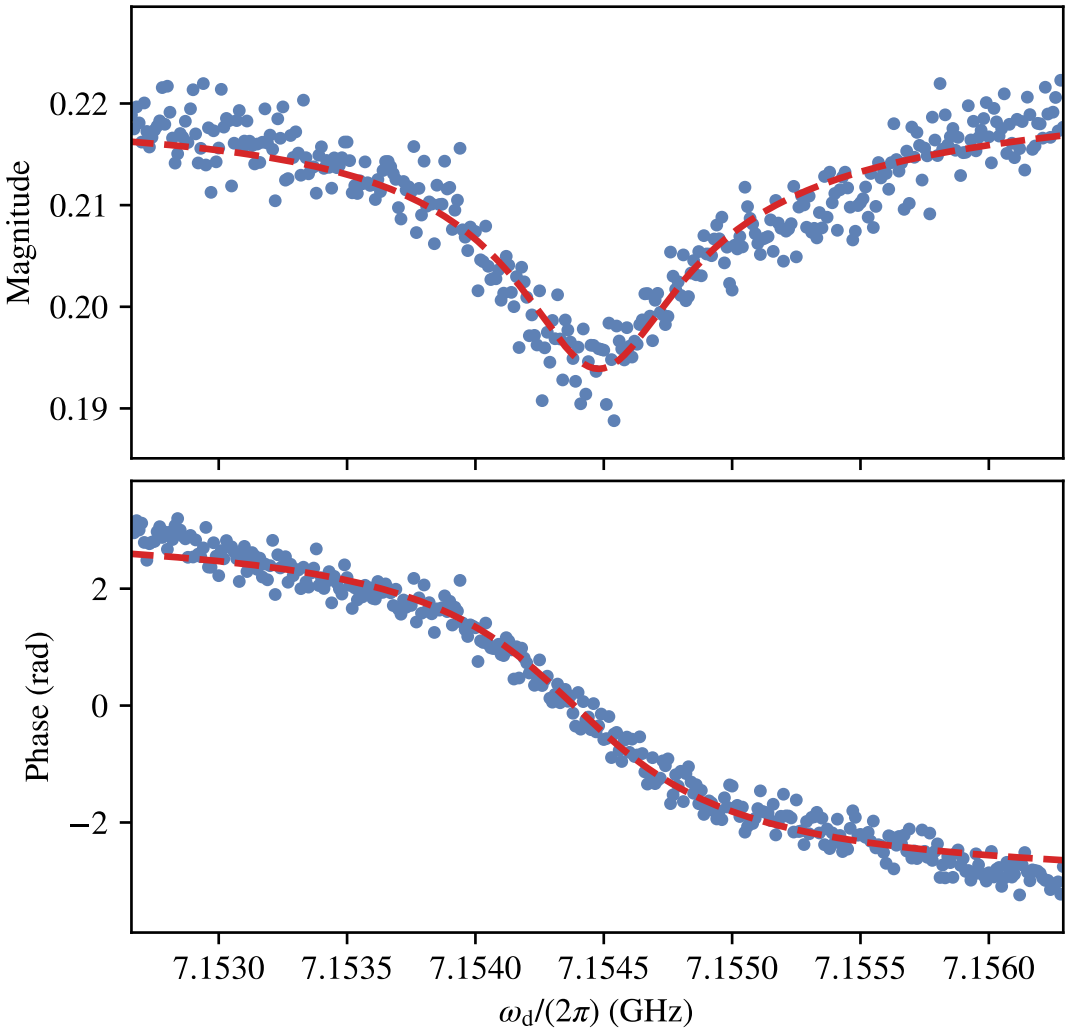

Figure 5.9: Fit (red dashed line) to the reflection data S_{cd} or S_{22} (blue dots) at the maximum frequency of resonator 2 when resonator 1 is far detuned.

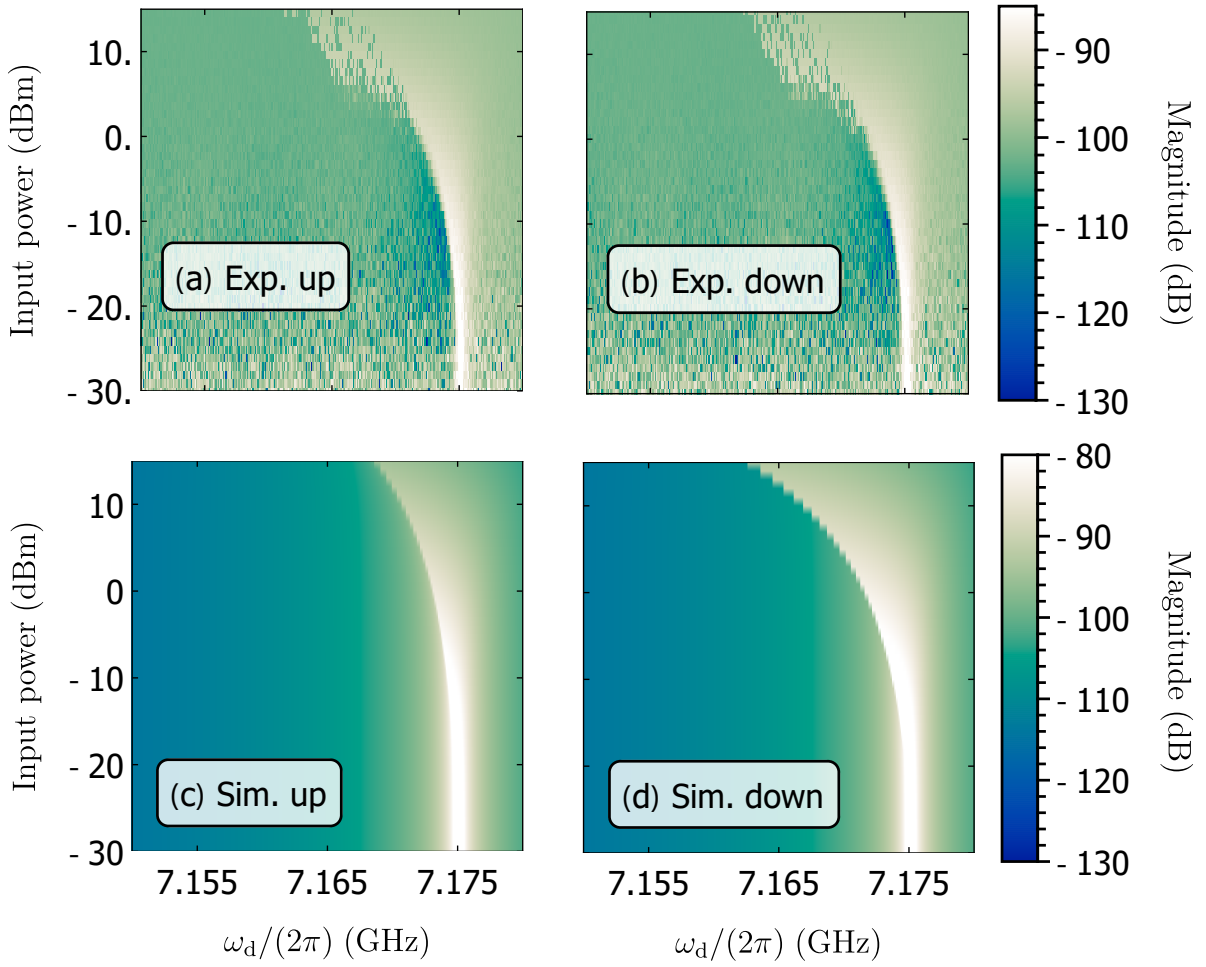

Figure 5.10: Frequency-dependent transmission measurements S_{ca} or S_{21} near the maximum frequency of resonator 2 as a function of the VNA output power. For this experiment resonator 2 is at 7.1 GHz. (a), (b) Experimental data and (c), (d) simulation using parameters extracted from the parasitic-path model. Frequency up(down)-sweeps are labelled with "up" ("down"). The simulation has been calibrated with the input attenuation and output amplification measured for our setup (for details, see App. 4.2.4).

unperturbed resonance frequency ω_0 [56]

$$|\Psi|^2 = a^2 = \frac{8}{3}\frac{\omega_0 C}{\beta}(\omega - \omega_0)\,. \tag{5.11}$$

For the experimental output voltage we derive (Sec. 2.1.9)

$$V_{\text{out}}^2 = \frac{8}{3}\frac{\omega_0 C}{\beta}(\omega_0 - \omega)\frac{Z_0\omega}{2Q_{\text{ext}}L}G, \tag{5.12}$$

with $Z_0 = 50\,\Omega$ being the characteristic impedance of the circuit and G the gain of the amplification chain.

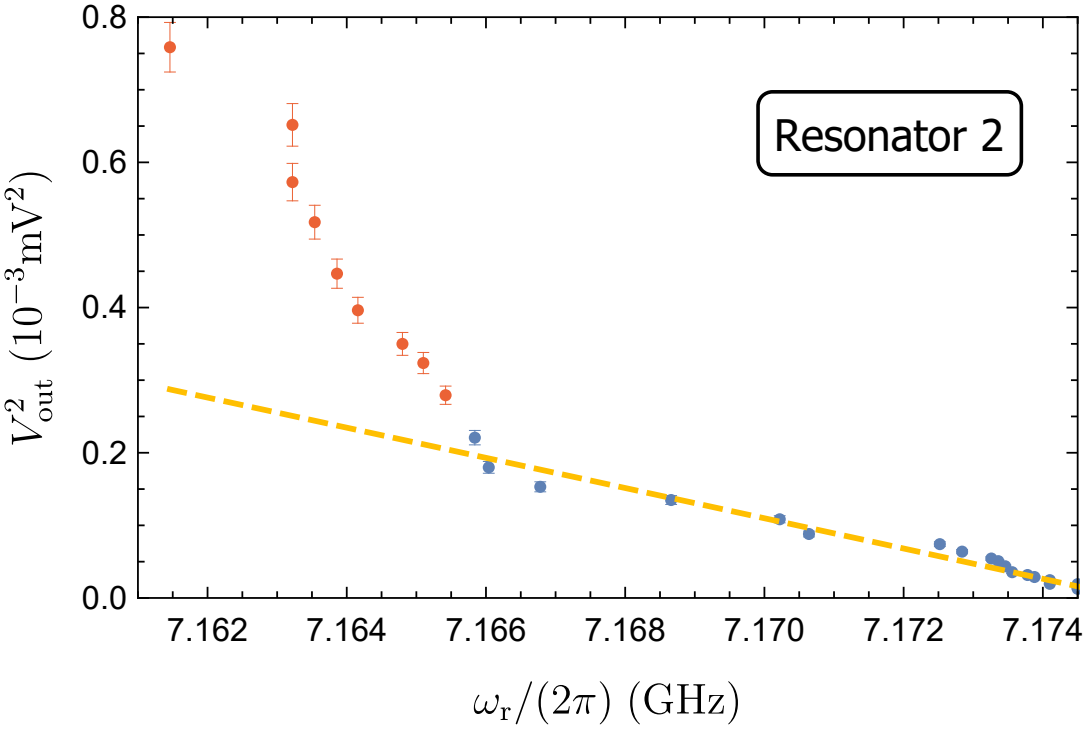

Figure 5.11: Squared output voltage at the resonance frequency ω_r as a function of this frequency for resonator 2 (blue and red dots) and the respective fit (dashed yellow line) of Eq. (5.12) to data points of low input power (blue dots). If not shown, the error bars are smaller than the symbol size. We estimate the uncertainty of each frequency point to be ±2 MHz.

In order to obtain information on β, we perform power-dependent measurements of the transmission through the tunable resonator system near the maximum resonance frequency of resonator 2. The corresponding data is shown in Fig. 5.10. As expected for a softening nonlinearity $U < 0$, the resonance frequency decreases with increasing power. We adjust the previous circuit model to include the purely nonlinear part of the equation of motion, $\beta\Psi^3$, and model the power dependence of the system. The current is adjusted by a nonlinear perturbation of the linear current I

$$I_{\mathrm{NL}} = I_i - \frac{\beta}{i\omega_\mathrm{d}^3} V_i^3. \tag{5.13}$$

Here, we use $\Psi = \int V \mathrm{d}t = V/(i\omega)$ to calculate the perturbation. Comparing the frequency up-sweep to the down-sweep, both for the measurement and simulation, we can observe a region of bistability for high input powers (starting at roughly 0 dBm). While the simulation predicts that the system is in different but stable states during sweeping up and down, the measurement shows jumps between the high and the low transmission state for both the up and down sweep. We find a good agreement for the upper and lower frequency bound of the bistability region between experiment and model (see Fig. 5.10).

In order to calculate the nonlinearity, we plot the square of the output voltage against the effective resonance frequency of the resonator, which is given by the maximum amplitude of the resonator response. As expected for a system with softening nonlinearity, the output voltage increases with decreasing resonance frequency. For small deviations from the unperturbed frequency, this increase is expected to be linear [see Eq. (5.12)]. The experimental data, taken from the transmission measurement shown in Fig. 5.10, indeed shows this linear increase for low input power (see Fig. 5.11). We use $C = C_2$ and $L = L_2$, i.e., the effective capacitance and inductance of resonator 2 from the parasitic-path model. As we look at the nonlinearity of resonator 2 in a transmission measurement, where we apply a signal at the input of resonator 1 and measure at the output of resonator 2, the measured output signal can be directly related to the voltage inside resonator 2 via the external quality factor determined in Sec. 5.2.1. From a photon number calibration measurement (see App. 4.2.4), we estimate that the gain of our amplification chain is $G = 38 \pm 4\,\mathrm{dB}$. The uncertainty of the following results is calculated using error propagation, where the main contributor is the uncertainty of the gain G. As the main contribution to the uncertainty of the nonlinearity stem from uncertainties of the gain, which was estimated in decibel, the error bars are asymmetric in linear units. A numerical fit of Eq. (5.12) to the squared output voltage as a function of the resonance frequency in the low power region (Fig. 5.11) yields $\beta = 1.97^{+3.03}_{-1.19} \times 10^{36}\,\mathrm{A\,V^{-3}\,s^3}$, which we can directly relate to the nonlinearity U via Eq. (5.1) and Eq. (5.10). For resonator 2, we get $U_{\mathrm{res2}} = 0.10^{+0.16}_{-0.06}\,\mathrm{MHz}$.

We find that the predictions of our theoretical model for the nonlinearity agree well with our measurement within its uncertainty (see Fig. 5.4).

5.3 Preliminary results of correlation function measurements

We perform first second order correlation function measurements [$g^{(2)}(0)$], using the setup described in 4.2.4. We use a coherent state that is sent to the sample and reflected by the far detuned resonators. Our tests confirm that the measurement apparatus works as expected.

5.3.1 Direct correlation function measurements

The first more direct approach is to calculate the correlation function directly from the measured moments of I and Q. Using

$$I = \frac{\hat{a} + \hat{a}^\dagger}{2} \quad \text{and} \quad Q = \frac{\hat{a} - \hat{a}^\dagger}{2i}, \tag{5.14}$$

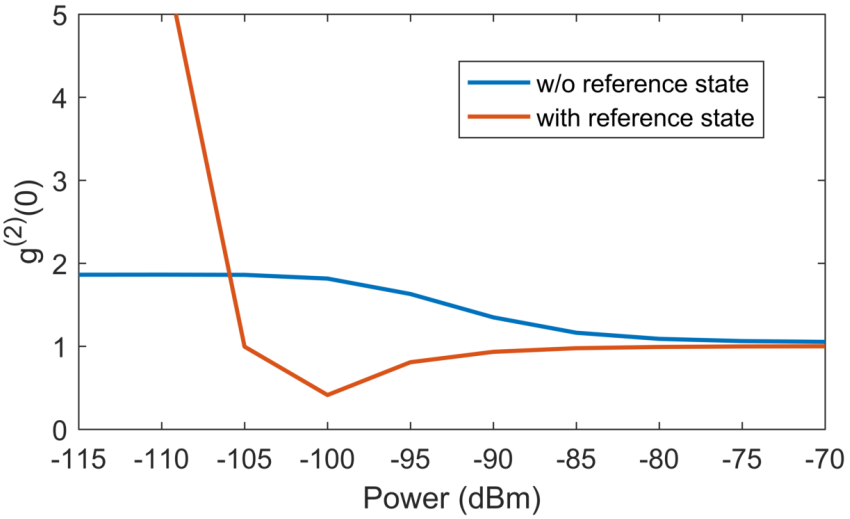

Figure 5.12: Correlation function measurement of a weak coherent signal reflected at the detuned sample both with with (red) and without (blue) a reference state.

we can calculate

$$g_{\mathrm{i}}^{(2)}(0) = \frac{\left\langle \hat{a}_{\mathrm{i}}^{\dagger}\hat{a}_{\mathrm{i}}^{\dagger}\hat{a}_{\mathrm{i}}\hat{a}_{\mathrm{i}} \right\rangle}{\left\langle \hat{a}_{\mathrm{i}}^{\dagger}\hat{a}_{\mathrm{i}} \right\rangle^{2}} = \frac{\left\langle \hat{I}_{\mathrm{i}}^{4} \right\rangle + 2\left\langle \hat{I}_{\mathrm{i}}^{2}\hat{Q}_{\mathrm{i}}^{2} \right\rangle + \left\langle \hat{Q}_{\mathrm{i}}^{4} \right\rangle}{\left(\left\langle \hat{I}_{\mathrm{i}}^{2} \right\rangle + \left\langle \hat{Q}_{\mathrm{i}}^{2} \right\rangle\right)^{2}}. \tag{5.15}$$

The averaged moments of the right hand side of the equation are all direct results of the measurement setup. In Fig. 5.12, where we plot the correlation function that was measured like this in blue for a coherent signal, that is reflected at the far detuned resonators, for varying input power. We see that for higher input powers ($P_{\mathrm{input}} \geq -80\,\mathrm{dBm}$) the correlation function trends towards 1, which is the expected value for a coherent signal. Around the mentioned threshold, the difference to 1 is less then 0.1 and gets smaller the higher the input power. For low input power, the measured correlation function deviates from 1 and trends towards 2, saturating at around 1.86. In this region, the signal statistics is dominated by thermal room temperature and amplifier noise.

5.3.2 Correlation function measurements with a reference state

Future measurements on the correlation function of the two-resonator sample will require the detection of low-power microwave signals emerging from the cryostat. Since these signals have to be amplified, they are covered with the noise added by the amplification chain. This noise contribution can be separated from the actual signal by means of the so-called reference method, where the noise moments of the chain are probed with a well-known reference state. In order to test our setup, we use a well know state to calibrate the noise contribution to the measurement shown in the previous section. In the experiment, we do this by pulsing the input signal. The pulse is performed in a way,

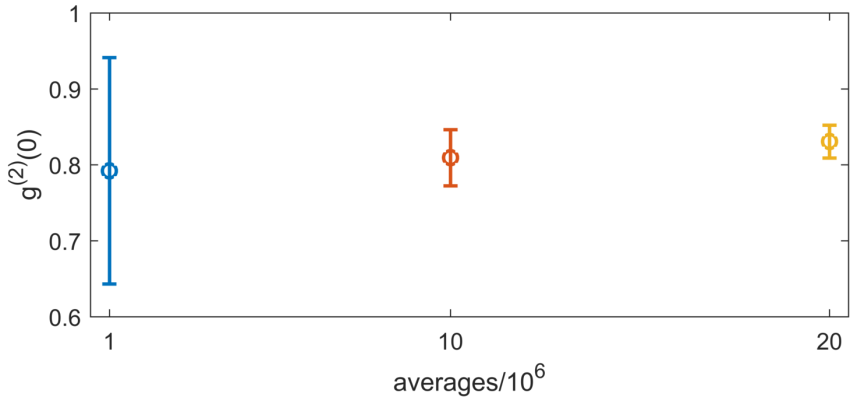

Figure 5.13: Correlation function measurement with fixed input power and varying averaging number. For a higher number of averages, the measured correlation function increases slowly, but stays well below 1 even when taking its standard deviation into account.

so that in the first half of the measured trace the signal is off, meaning that we detect a vacuum state. The state is still overlayed with noise contribution and can therefore be used in order to calculate the noise terms that distort our measurement results. It can be shown that

$$\hat{I}_\mathrm{i} = \hat{i}_\mathrm{i} + \hat{V}_\mathrm{i}^\dagger \tag{5.16}$$

$$\hat{Q}_\mathrm{i} = \hat{q}_\mathrm{i} + \hat{V}_\mathrm{i}^\dagger. \tag{5.17}$$

Here, $\hat{V}_\mathrm{i}^\dagger$ is the contribution of the noise and $\hat{i}_\mathrm{i}$ ($\hat{q}_\mathrm{i}$) is the actual in-phase (quadrature) component of the input signal without the noise contribution. $\hat{I}_\mathrm{i}$ and $\hat{Q}_\mathrm{i}$ refer to the measured components that include the noise. Using the reference state, we can extract the noise components $\hat{V}_\mathrm{i}^\dagger$ from the well known components $\hat{i}_\mathrm{i}$ and $\hat{q}_\mathrm{i}$ of a vacuum state. For further details on the calculations, we refer the reader to [70].

In the second half of the measurement trace, the coherent signal is on and we measure the components of the signal overlayed by the noise contribution. Knowing $\hat{V}_\mathrm{i}^\dagger$, we can then calculate the actual signal components using a equivalent calculation as above. The correlation function is then calculated in the same way as in the measurement without the reference state from the calibrated quadrature components. The result of the reference state method is shown in Fig. 5.12 (red curve). For higher input power we see a similar behavior as in the previous measurement (blue curve), where the correlation function is equal to the expected one of a coherent signal. We notice that both measurements do not fully coincide, as the one measured without the reference state stays just above 1. The one measured with the reference state on the other hand is almost exactly 1 ($g_\mathrm{i}^{(2)}(0) = 0.992$ at $-80\,\mathrm{dBm}$). Also for lower input power, the measurement with reference state deviates less from the expected value. Taking e.g. 10 % deviation from 1 as the threshold, we get a sensitivity increase between 10 dB and 15 decibel for the reference state method.

At $P_\mathrm{input} \leq -90\,\mathrm{dBm}$ the correlation function drops well below 1 (down to $g_\mathrm{i}^{(2)}(0) = 0.4$)

and quickly increases below $P_{\text{input}} \leq -100\,\text{dBm}$ to values above 2. Not shown here for visibility reasons is the increase of the correlation function to more than 1000. Although we have not fully understood why we measure a correlation function below 1 for low input power in the experiment, we have performed investigations, that let us believe, that this is in fact a physical property of the input signal and not a effect of the measurement technique. First, we perform the same measurement as shown for an increased number of averages in order to exclude a stochastical process. The results for a measurement performed at $P_{\text{input}} = -95\,\text{dBm}$ can be seen in Fig. 5.13. We increase the average number from 10^6 to 20^7 averages and show the average calculated correlation function (circle) and its standard deviation (error bar). We can see, that for a higher number of averages, the standard deviation decreases to 0.05. Although the calculated correlation function increases with higher number of averages, the edges of the standard deviation are clearly lower than 1 meaning that the observed effect is not of statistical nature.

We can however simulate a different behavior by adding randomly created noise to a simulated coherent signal. We reproduce the pulse shape of the input signal and the averaging process. We then use the reference state algorithm to calculate the correlation function similar to the experiment. Here, we find that the correlation function stays above 1 at all times. The strong increase in correlation function at the lowest input powers can be observed as well. We can therefore exclude the algorithm itself as the source of the effect. As a last step, we were also able to reproduce the measurement results in a different experimental setup, excluding the distinct setup from being the origin.

In order to fully understand this behavior further investigations both on a experimental and theoretical level have to be made. Nevertheless we conclude that the fact that we measure a correlation function of below 1 for a weak coherent signal is a physical property of the coherent signal.

Chapter 6

Summary and Outlook

In this thesis we have presented experimental results of a superconducting circuit that is suitable for quantum simulation of a Bose-Hubbard system. We also have showed theoretical calculations of the Bose-Hubbard model that is represented by our circuit. Dependent on the parameters of the model, the calculated second order correlation function $g^{(2)}(0)$ inside a lattice site and the cross correlation function $g^{(2X)}(0)$ between two sites can both be lower, equal or higher than 1, which is the expected value of a coherent field. The four main parameters, which determine the properties of the field are the on-site nonlinearity U, the hopping rate J between the lattice sites, the driving frequency and the driving strength of the external driving field. By tuning these parameters, we can set the correlation functions of the system to different regimes, where $g^{(2X)}(0)$, $g^{(2)}(0) > 1$ or $g^{(2X)}(0)$, $g^{(2)}(0) < 1$. We can also set the correlations functions so that $g^{(2X)}(0) > 1$ and $g^{(2)}(0) < 1$ and vice versa. These regions exhibit completely different physical properties and are therefore interesting to investigate further.

In order to do so experimentally, we have designed and fabricated a superconducting circuit that represents a Bose Hubbard dimer. The circuit consists of two capacitively coupled microwave waveguide resonators each intercepted by a DC-SQUID. The SQUID adds a nonlinearity into the otherwise linear system. Additionally, it offers the possibility to tune the nonlinearity and with it the resonance frequency of the resonators with an externally or on-chip applied magnetic field. The resonator fields can be driven through two waveguides that are capacitively coupled to each end of the resonator chain. These input lines can also be used to read out the resonators. We have showed, that we are able to control all relevant parameters of the system, i.e. the nonlinearity and the driving field. The hopping rate is indirectly coupled to the nonlinearity and cannot be controlled individually. In order to be able to set the nonlinearity of both resonators to the same arbitrary value, we have calibrated the external coil and the on-chip antennas, so that we can create the needed magnetic field at each SQUID loop.

We have presented two ways to determine the nonlinearity of the resonators representing this Bose Hubbard dimer. First, we have estimated the nonlinearity by modeling the experimental data of a magnetic flux sweep with a circuit model that includes a parasitic path. We have then calculated the nonlinearity from the extracted parameters of the

theoretical model. We have calculated the absolute value of the nonlinearity of resonator 1 (2) which can be tuned from a minimum of 0.1 MHz (0.06 MHz) to a maximum of 8.0 MHz (6.1 MHz). The nonlinearity can therefore be tuned by almost two orders of magnitude. We are limited by design as our experimental setup is not suited for larger tuning of the resonance frequency. When tuning the nonlinearity over its full possible range, the system is brought into regions where $J > U$ as well as ones where $U > J$. Second, we have directly measured the nonlinearity from the power dependence of the non-linear resonators. An increasing drive power at the entrance of the resonator shifts the resonance frequency of the resonator to lower frequencies. Fitting this behavior gives us direct access to the nonlinearity of the resonator. For the nonlinearity of resonator 2 we get $U_{\mathrm{res2}} = 0.10^{+0.16}_{-0.06}\,\mathrm{MHz}$.

The first steps going forward will be to further improve the measurement technique of the nonlinearity. For this, the most important part will be to especially improve the calibration of the input power. Doing so, will allow for a much more precise measurement of the nonlinearity. Furthermore, we will implement the presented setup for the measurement of the second order correlation functions. With this, it will be possible to verify the theoretical calculations presented in this work. Finally, larger scale samples with additional lattice sites will allow for quantum simulations of the phase transitions of the Bose-Hubbard model. Both longer chains of resonators or two dimensional setups could be possible.

Appendix A

Calculation of the external quality factor

In Sec. 2.1.9, it is shown that, in order to extract the nonlinearity from a power dependent measurement, we need to know the external quality factor of the resonators. Here, we derive equations, that allow us to extract the external quality factor from a reflection measurement of our two resonator system.

First, we consider a system without intrinsic damping, of which the Hamiltonian

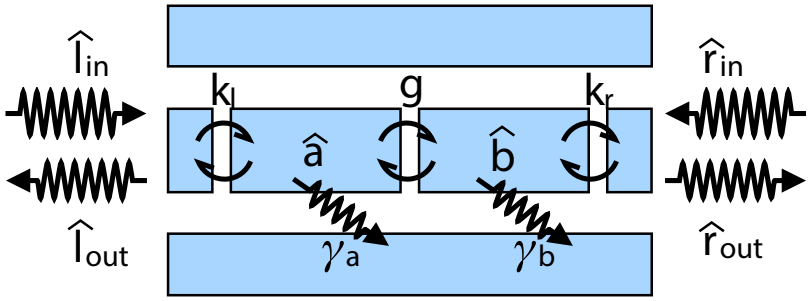

Figure A.1: Quantum description of the system. The two intra-resonator fields, a and b, are coupled with a coupling strength g, which are also coupled to two independent baths with strengths κ_l and κ_r, respectively. From the two baths, one can identify the input and output fields as l_{in} and l_{out}, or r_{in} and r_{out}, depending on the boundary conditions. In addition, we denote the intrinsic losses of the two cavities as γ_a and γ_b, respectively. The hat symbols denoting quantum operators in the sketch are omitted in the text to simplify the notation.

reads [71–73]

$$H_{sys} = \hbar\omega_{\mathrm{a}} a^{\dagger} a + \hbar\omega_{\mathrm{b}} b^{\dagger} b + \hbar g \left(a^{\dagger} b + a b^{\dagger}\right) \tag{A.1}$$

$$\begin{aligned} H = H_{sys} &+ \hbar \int_{-\infty}^{+\infty} d\omega \left\{ \omega l^{\dagger}(\omega)\, l(\omega) + \right. \\ &\left. i\kappa_l(\omega) \left[l^{\dagger}(\omega)\, a - l(\omega)\, a^{\dagger} \right] \right\} \\ &+ \hbar \int_{-\infty}^{+\infty} d\omega \left\{ \omega r^{\dagger}(\omega)\, r(\omega) + \right. \\ &\left. i\kappa_l(\omega) \left[r^{\dagger}(\omega)\, b - r(\omega)\, b^{\dagger} \right] \right\}. \end{aligned} \tag{A.2}$$

Here, by convention, we define the specific type of coupling between the intra-resonator fields, a for resonator 1 and b for resonator 2, and the bath, $l(\omega)$ and $r(\omega)$, respectively, for the simplicity of derivation. Then, one can derive the following Heisenberg equations of motion for the field operators

$$\dot{l}(\omega) = -i\omega l(\omega) + \kappa_{\ell}(\omega)\, a, \tag{A.3}$$

$$\dot{a} = -\frac{i}{\hbar}\left[a, H_{sys}\right] - \int_{-\infty}^{+\infty} d\omega \kappa_{\ell}(\omega)\, l(\omega), \tag{A.4}$$

$$\dot{r}(\omega) = -i\omega r(\omega) + \kappa_r(\omega)\, b, \tag{A.5}$$

$$\dot{b} = -\frac{i}{\hbar}\left[b, H_{sys}\right] - \int_{-\infty}^{+\infty} d\omega \kappa_r(\omega)\, r(\omega). \tag{A.6}$$

We note that the above equations can be split into two groups, namely Eq. (A.3)/(A.4) and Eq. (A.5)/(A.6), each of which is identical to the input-output formalism of a single system. Following the same procedure as in Ref. [71], we define the input fields

$$l_{\mathrm{in}} = \frac{1}{\sqrt{2\pi}} \int_{-\infty}^{+\infty} d\omega e^{-i\omega t} l(\omega), \tag{A.7}$$

$$r_{\mathrm{in}} = \frac{1}{\sqrt{2\pi}} \int_{-\infty}^{+\infty} d\omega e^{-i\omega t} r(\omega). \tag{A.8}$$

The equations of the intra-resonator fields thus read

$$\dot{a} = -i\omega_{\mathrm{a}} a - igb - \frac{\gamma_{\ell} + \gamma_{\mathrm{a}}}{2} a - \sqrt{\gamma_{\ell}} l_{\mathrm{in}}(t), \tag{A.9}$$

$$\dot{b} = -i\omega_{\mathrm{b}} b - iga - \frac{\gamma_{\mathrm{r}} + \gamma_{\mathrm{b}}}{2} b - \sqrt{\gamma_{\mathrm{r}}} r_{\mathrm{in}}(t). \tag{A.10}$$

Here, we have used the first Markov approximation $\gamma_{\ell} = 2\pi\kappa_{\ell}^2(\omega)$, $\gamma_{\mathrm{r}} = 2\pi\kappa_r^2(\omega)$ [71]. We also added the internal loss rates γ_{a} γ_{b} of resonator 2. The two output fields are

$$l_{out} = l_{\mathrm{in}} + \sqrt{\gamma_{\ell}} a(t), \tag{A.11}$$

$$r_{out} = r_{\mathrm{in}} + \sqrt{\gamma_{\mathrm{r}}} b(t). \tag{A.12}$$

Then, we move to the frame rotating with respect to the reference frequency ω_d and define $\Delta_\mathrm{a} = \omega_\mathrm{a} - \omega_\mathrm{d}$, $\Delta_\mathrm{b} = \omega_\mathrm{b} - \omega_\mathrm{d}$, where ω_d is the frequency of the driving field. For steady state solutions, we find

$$S_{11} = \frac{l_{out}}{l_{in}} = 1 - \frac{\gamma_\ell \left(i\Delta_\mathrm{b} + \frac{\gamma_\mathrm{r}+\gamma_b}{2}\right)}{\left(i\Delta_\mathrm{a} + \frac{\gamma_\ell+\gamma_a}{2}\right)\left(i\Delta_\mathrm{b} + \frac{\gamma_\mathrm{r}+\gamma_b}{2}\right) + g^2}, \tag{A.13}$$

$$S_{21} = \frac{r_{out}}{l_{in}} = \frac{ig\sqrt{\gamma_\ell\gamma_\mathrm{r}}}{\left(i\Delta_\mathrm{a} + \frac{\gamma_\ell+\gamma_a}{2}\right)\left(i\Delta_\mathrm{b} + \frac{\gamma_\mathrm{r}+\gamma_b}{2}\right) + g^2}, \tag{A.14}$$

$$S_{12} = \frac{l_{out}}{r_{in}} = \frac{ig\sqrt{\gamma_\ell\gamma_\mathrm{r}}}{\left(i\Delta_\mathrm{a} + \frac{\gamma_\ell+\gamma_a}{2}\right)\left(i\Delta_\mathrm{b} + \frac{\gamma_\mathrm{r}+\gamma_b}{2}\right) + g^2}, \tag{A.15}$$

$$S_{22} = \frac{r_{out}}{r_{in}} = 1 - \frac{\gamma_\mathrm{r} \left(i\Delta_\mathrm{a} + \frac{\gamma_\ell+\gamma_a}{2}\right)}{\left(i\Delta_\mathrm{a} + \frac{\gamma_\ell+\gamma_a}{2}\right)\left(i\Delta_\mathrm{b} + \frac{\gamma_\mathrm{r}+\gamma_b}{2}\right) + g^2}. \tag{A.16}$$

Here, we have used the imaginary unit i, which is related to the imaginary unit in electrical engineering by $i = -j$. We find that all the damping coefficients, γ_a, γ_b, γ_ℓ, and γ_r can be obtained by detuning the two resonators, and measuring the internal and coupling quality factors from the reflection responses S_{11} and S_{22}, respectively.

We find that the scattering parameter S_{22} only depends on the external quality factor $Q_{\mathrm{ext},2} = \omega_\mathrm{b}/\gamma_b$ and the loaded quality factor $Q_{\ell,2}$ of resonator 2, in the limit where resonator 1 is far detuned $\Delta_\mathrm{a} \to \infty$:

$$S_{22} \approx 1 - \frac{2Q_{\ell,2}/Q_{\mathrm{ext},2}}{1 - 2iQ_{\ell,2}\Delta_b}. \tag{A.17}$$

On resonance of the second resonator, $\Delta_\mathrm{b} = 0$, we then get

$$S_{22} \approx 1 - \frac{2Q_{\ell,2}}{Q_{\mathrm{ext},2}}. \tag{A.18}$$

We extract the loaded quality factor from a fit to the phase θ of the scattering parameter using

$$\theta = \theta_0 + 2\arctan(2Q_{\ell,2}(1 - \omega/\omega_{\mathrm{r},2})). \tag{A.19}$$

From this we calculate the external quality factor with Eq. (A.18).

In our experiment, we detune the two resonators by approximately 200 MHz and measure the reflection response S_{22}. To determine the internal and external quality factors from the scattering coefficients, we follow the recipe described in Ref. [74] which includes different corrections of the measurement signal. The corresponding fit to the measurement data is shown in Fig. 5.9. Finally, Tab. A.1 summarizes all determined values. Specifically, we obtain $Q_{ext,2} = 1.35 \cdot 10^5$. Comparing this to the internal loss of $7.8 \cdot 10^3$, we find

parameter	value
ω_b	$2\pi \times 7.154\,\mathrm{GHz}$
$Q_{\ell,2}$	$7.4 \cdot 10^3$
$Q_{int,2}$	$7.8 \cdot 10^3$
$Q_{ext,2}$	$1.35 \cdot 10^5$
γ_b	$2\pi \times 0.91\,\mathrm{MHz}$
γ_r	$2\pi \times 0.05\,\mathrm{MHz}$

Table A.1: Parameters extracted from the quality factor fitting procedure described in App. A near the maximum resonance frequency of resonator 2. We assume the external quality factor to be frequency-independent.

that our system is undercoupled. For use in larger quantum simulation experiments, an investigation into the causes for the high internal loss is needed to enable longer polariton life times. In order to achieve this, changing the sensitivity of the SQUID both to external fields and to the fields of the flux lines would be the first thing to try.

Bibliography

[1] R. P. Feynman, "Simulating physics with computers", International Journal of Theoretical Physics **21**, 467 (1982).

[2] J. I. Cirac and P. Zoller, "Goals and opportunities in quantum simulation", Nature Physics **8**, 264 (2012).

[3] I. Buluta and F. Nori, "Quantum Simulators", Science **326**, 108 (2009).

[4] D. Jaksch and P. Zoller, "The cold atom Hubbard toolbox", Annals of Physics **315**, 52 (2005).

[5] M. Hartmann, F. Brandao, and M. Plenio, "Strongly interacting polaritons in coupled arrays of cavities", Nature Physics **2**, 849 (2006).

[6] A. D. Greentree, C. Tahan, J. H. Cole, and L. C. L. Hollenberg, "Quantum phase transitions of light", Nature Physics **2**, 856 (2006).

[7] J. Chiaverini and W. E. Lybarger, "Laserless trapped-ion quantum simulations without spontaneous scattering using microtrap arrays", Phys. Rev. A **77**, 022324 (2008).

[8] A. A. Houck, H. E. Türeci, and J. Koch, "On-chip quantum simulation with superconducting circuits", Nat Phys **8**, 292 (2012).

[9] T. Yamamoto, M. Watanabe, J. Q. You, Y. A. Pashkin, O. Astafiev, Y. Nakamura, F. Nori, and J. S. Tsai, "Spectroscopy of superconducting charge qubits coupled by a Josephson inductance", Phys. Rev. B **77**, 064505 (2008).

[10] J. You and F. Nori, "Superconducting circuits and quantum information", arXiv preprint quant-ph/0601121 (2006).

[11] M. Hofheinz, H. Wang, M. Ansmann, R. C. Bialczak, E. Lucero, M. Neeley, A. O'connell, D. Sank, J. Wenner, J. M. Martinis, et al., "Synthesizing arbitrary quantum states in a superconducting resonator", Nature **459**, 546 (2009).

[12] T. Niemczyk, F. Deppe, H. Huebl, E. P. Menzel, F. Hocke, M. J. Schwarz, J. J. Garcia-Ripoll, D. Zueco, T. Hümmer, E. Solano, A. Marx, and R. Gross, "Circuit quantum electrodynamics in the ultrastrong-coupling regime", Nature Physics **6**, 772 (2010).

[13] J. Goetz, F. Deppe, K. G. Fedorov, P. Eder, M. Fischer, S. Pogorzalek, E. Xie, A. Marx, and R. Gross, "Parity-Engineered Light-Matter Interaction", Phys. Rev. Lett. **121**, 060503 (2018).

[14] F. Deppe, M. Mariantoni, E. P. Menzel, A. Marx, S. Saito, K. Kakuyanagi, H. Tanaka, T. Meno, K. Semba, H. Takayanagi, E. Solano, and R. Gross, "Two-photon probe of the Jaynes–Cummings model and controlled symmetry breaking in circuit QED", Nature Physics **4**, 686 (2008).

[15] J. E. Mooij, T. P. Orlando, L. Levitov, L. Tian, C. H. van der Wal, and S. Lloyd, "Josephson Persistent-Current Qubit", Science **285**, 1036 (1999).

[16] A. Wallraff, D. I. Schuster, A. Blais, L. Frunzio, R.-S. Huang, J. Majer, S. Kumar, S. M. Girvin, and R. J. Schoelkopf, "Strong coupling of a single photon to a superconducting qubit using circuit quantum electrodynamics", Nature **431**, 162 (2004).

[17] J.-T. Shen and S. Fan, "Coherent Single Photon Transport in a One-Dimensional Waveguide Coupled with Superconducting Quantum Bits", Phys. Rev. Lett. **95**, 213001 (2005).

[18] J. Koch, M. Y. Terri, J. Gambetta, A. A. Houck, D. Schuster, J. Majer, A. Blais, M. H. Devoret, S. M. Girvin, and R. J. Schoelkopf, "Charge-insensitive qubit design derived from the Cooper pair box", Physical Review A **76**, 042319 (2007).

[19] J. M. Martinis, "Superconducting phase qubits", Quantum Information Processing **8**, 81 (2009).

[20] L. Frunzio, A. Wallraff, D. Schuster, J. Majer, and R. Schoelkopf, "Fabrication and characterization of superconducting circuit QED devices for quantum computation", IEEE Transactions on Applied Superconductivity **15**, 860 (2005).

[21] T. Niemczyk, F. Deppe, M. Mariantoni, E. P. Menzel, E. Hoffmann, G. Wild, L. Eggenstein, A. Marx, and R. Gross, "Fabrication technology of and symmetry breaking in superconducting quantum circuits", Superconductor Science and Technology **22**, 034009 (2009).

[22] P. Eder, T. Ramos, J. Goetz, M. Fischer, S. Pogorzalek, J. P. Martínez, E. P. Menzel, F. Loacker, E. Xie, J. J. Garcia-Ripoll, K. G. Fedorov, A. Marx, F. Deppe, and R. Gross, "Quantum probe of an on-chip broadband interferometer for quantum microwave photonics", Superconductor Science and Technology **31**, 115002 (2018).

[23] J. Goetz, F. Deppe, P. Eder, M. Fischer, M. Müting, J. P. Martínez, S. Pogorzalek, F. Wulschner, E. Xie, K. G. Fedorov, A. Marx, and R. Gross, "Second-order decoherence mechanisms of a transmon qubit probed with thermal microwave states", Quantum Science and Technology **2**, 025002 (2017).

[24] F. Paauw, A. Fedorov, C. M. Harmans, and J. Mooij, "Tuning the gap of a superconducting flux qubit", Physical review letters **102**, 090501 (2009).

[25] J. Majer, J. Chow, J. Gambetta, J. Koch, B. Johnson, J. Schreier, L. Frunzio, D. Schuster, A. A. Houck, A. Wallraff, et al., "Coupling superconducting qubits via a cavity bus", Nature **449**, 443 (2007).

[26] F. Arute, K. Arya, R. Babbush, D. Bacon, J. C. Bardin, R. Barends, R. Biswas, S. Boixo, F. G. Brandao, D. A. Buell, et al., "Quantum supremacy using a programmable superconducting processor", Nature **574**, 505 (2019).

[27] J. Goetz, F. Deppe, M. Haeberlein, F. Wulschner, C. W. Zollitsch, S. Meier, M. Fischer, P. Eder, E. Xie, K. G. Fedorov, E. P. Menzel, A. Marx, and R. Gross, "Loss mechanisms in superconducting thin film microwave resonators", Journal of Applied Physics **119**, 015304 (2016).

[28] A. Megrant, C. Neill, R. Barends, B. Chiaro, Y. Chen, L. Feigl, J. Kelly, E. Lucero, M. Mariantoni, P. J. O?Malley, et al., "Planar superconducting resonators with internal quality factors above one million", Applied Physics Letters **100**, 113510 (2012).

[29] E. Xie, F. Deppe, M. Renger, D. Repp, P. Eder, M. Fischer, J. Goetz, S. Pogorzalek, K. G. Fedorov, A. Marx, and R. Gross, "Compact 3D quantum memory", Applied Physics Letters **112**, 202601 (2018).

[30] M. Reagor, H. Paik, G. Catelani, L. Sun, C. Axline, E. Holland, I. M. Pop, N. A. Masluk, T. Brecht, L. Frunzio, et al., "Reaching 10 ms single photon lifetimes for superconducting aluminum cavities", Applied Physics Letters **102**, 192604 (2013).

[31] C. Noh and D. G. Angelakis, "Quantum simulations and many-body physics with light", Reports on Progress in Physics **80** (2017).

[32] C. Rigetti, J. M. Gambetta, S. Poletto, B. L. T. Plourde, J. M. Chow, A. D. Córcoles, J. A. Smolin, S. T. Merkel, J. R. Rozen, G. A. Keefe, M. B. Rothwell, M. B. Ketchen, and M. Steffen, "Superconducting qubit in a waveguide cavity with a coherence time approaching 0.1 ms", Phys. Rev. B **86**, 100506 (2012).

[33] P. Coleman, *Introduction to many-body physics* (Cambridge University Press, 2015).

[34] C. Noh and D. G. Angelakis, "Quantum simulations and many-body physics with light", Reports on Progress in Physics **80**, 016401 (2016).

[35] I. Bloch, J. Dalibard, and W. Zwerger, "Many-body physics with ultracold gases", Reviews of Modern Physics **80**, 885 (2008).

[36] M. J. Hartmann, "Quantum simulation with interacting photons", Journal of Optics **18**, 104005 (2016).

[37] M. Greiner, O. Mandel, T. Esslinger, T. W. Hänsch, and I. Bloch, "Quantum phase transition from a superfluid to a Mott insulator in a gas of ultracold atoms", Nature **415**, 39 (2002).

[38] I. Bloch, J. Dalibard, and S. Nascimbene, "Quantum simulations with ultracold quantum gases", Nature Physics **8**, 267 (2012).

[39] J. Zhang, G. Pagano, P. W. Hess, A. Kyprianidis, P. Becker, H. Kaplan, A. V. Gorshkov, Z.-X. Gong, and C. Monroe, "Observation of a many-body dynamical phase transition with a 53-qubit quantum simulator", Nature **551**, 601 (2017).

[40] R. Blatt and C. F. Roos, "Quantum simulations with trapped ions", Nature Physics **8**, 277 (2012).

[41] S. Barrett, K. Hammerer, S. Harrison, T. E. Northup, and T. J. Osborne, "Simulating quantum fields with cavity QED", Physical review letters **110**, 090501 (2013).

[42] Y. Salathé, M. Mondal, M. Oppliger, J. Heinsoo, P. Kurpiers, A. Potočnik, A. Mezzacapo, U. Las Heras, L. Lamata, E. Solano, et al., "Digital quantum simulation of spin models with circuit quantum electrodynamics", Physical Review X **5**, 021027 (2015).

[43] S. Schmidt and J. Koch, "Circuit QED lattices: towards quantum simulation with superconducting circuits", Annalen der Physik **525**, 395 (2013).

[44] R. Barends, L. Lamata, J. Kelly, L. García-Álvarez, A. Fowler, A. Megrant, E. Jeffrey, T. White, D. Sank, J. Mutus, et al., "Digital quantum simulation of fermionic models with a superconducting circuit", Nature communications **6**, 7654 (2015).

[45] A. Kandala, A. Mezzacapo, K. Temme, M. Takita, M. Brink, J. M. Chow, and J. M. Gambetta, "Hardware-efficient variational quantum eigensolver for small molecules and quantum magnets", Nature **549**, 242 (2017).

[46] M. Leib and M. J. Hartmann, "Bose-Hubbard dynamics of polaritons in a chain of circuit quantum electrodynamics cavities", New Journal of Physics **12**, 93031 (2010).

[47] M. Leib, F. Deppe, A. Marx, R. Gross, and M. J. Hartmann, "Networks of nonlinear superconducting transmission line resonators", New Journal of Physics **14**, 75024 (2012).

[48] M. Leib and M. J. Hartmann, "Many body physics with coupled transmission line resonators", Phys. Scr. **T153**, 14042 (2013).

[49] J. Bourassa, F. Beaudoin, J. M. Gambetta, and A. Blais, "Josephson-junction-embedded transmission-line resonators: From Kerr medium to in-line transmon", Phys. Rev. A **86** (2012).

[50] M. Fitzpatrick, N. M. Sundaresan, A. C. Y. Li, J. Koch, and A. A. Houck, "Observation of a Dissipative Phase Transition in a One-Dimensional Circuit QED Lattice", Phys. Rev. X **7**, 011016 (2017).

[51] M. C. Collodo, A. Potočnik, S. Gasparinetti, J.-C. Besse, M. Pechal, M. Sameti, M. J. Hartmann, A. Wallraff, and C. Eichler, "Observation of the Crossover from Photon Ordering to Delocalization in Tunably Coupled Resonators", Phys. Rev. Lett. **122**, 183601 (2019).

[52] D. M. Pozar, *Microwave engineering; 3rd ed.* (Wiley, Hoboken, NJ, 2005), URL https://cds.cern.ch/record/882338.

[53] D. F. Walls and G. J. Milburn, *Quantum optics / D.F. Walls, G.J. Milburn* (Springer-Verlag Berlin ; New York, 1995), springer study ed. ed., ISBN 3540588310.

[54] J. Clarke and A. I. Braginski, *The SQUID Handbook Fundamentals and Technology of SQUIDs and SQUID Systems*, vol. 1 (Wiley-VCH, Weinheim, 2006), URL http://public.eblib.com/EBLPublic/PublicView.do?ptiID=481572.

[55] U. Fano, "Effects of Configuration Interaction on Intensities and Phase Shifts", Phys. Rev. **124**, 1866 (1961).

[56] A. Nayfeh and D. Mook, *Nonlinear Oscillations*, Wiley Classics Library (Wiley, 1995), ISBN 9780471121428, URL https://www.wiley.com/en-us/Nonlinear+Oscillations-p-9780471121428.

[57] M. Am-Shallem, A. Levy, I. Schaefer, and R. Kosloff, "Three approaches for representing Lindblad dynamics by a matrix-vector notation", arXiv e-prints:1510.08634 arXiv:1510.08634 (2015).

[58] G. Lindblad, "On the generators of quantum dynamical semigroups", Communications in Mathematical Physics **48**, 119 (1976).

[59] C. Navarrete-Benlloch, "Open systems dynamics: Simulating master equations in the computer", arXiv e-prints:1504.05266 arXiv:1504.05266 (2015).

[60] R. Loudon, *The quantum theory of light*, Oxford science publications (Clarendon Press, 1983), ISBN 9780198511526, URL https://books.google.de/books?id=_FTwAAAAMAAJ.

[61] A. Lebreton, I. Abram, R. Braive, I. Sagnes, I. Robert-Philip, and A. Beveratos, "Theory of interferometric photon-correlation measurements: Differentiating coherent from chaotic light", Phys. Rev. A **88**, 013801 (2013).

[62] S. Binder, "Numerical simulation of a driven-dissipative Bose-Hubbard dimer", Bachelor thesis, Technische Universität München (2017).

[63] U. Schaumburger, "Ketten von Resonatoren mit einstellbarer Nichtlinearität", Diploma thesis, Technische Universität München (2014).

[64] J. Martinez, "Circuit quantum electrodynamics with transmon qubits", Master thesis, Technische Universität München (2015).

[65] M. Mariantoni, E. P. Menzel, F. Deppe, M. A. Araque Caballero, A. Baust, T. Niemczyk, E. Hoffmann, E. Solano, A. Marx, and R. Gross, "Planck Spectroscopy and Quantum Noise of Microwave Beam Splitters", Phys. Rev. Lett. **105**, 133601 (2010).

[66] E. P. Menzel, R. Di Candia, F. Deppe, P. Eder, L. Zhong, M. Ihmig, M. Haeberlein, A. Baust, E. Hoffmann, D. Ballester, K. Inomata, T. Yamamoto, Y. Nakamura, E. Solano, A. Marx, and R. Gross, "Path Entanglement of Continuous-Variable Quantum Microwaves", Phys. Rev. Lett. **109**, 250502 (2012).

[67] L. Wang, "Fabrication stability of Josephson junctions for superconducting qubits", Master thesis, Technische Universität München (2015).

[68] S. Grotowski, "Programmable control of two non-linear resonators", Bachelor thesis, Technische Universität München (2019).

[69] M. Fischer, Q.-M. Chen, C. Besson, P. Eder, J. Goetz, S. Pogorzalek, M. Renger, E. Xie, M. J. Hartmann, K. G. Fedorov, A. Marx, F. Deppe, and R. Gross, "In situ tunable nonlinearity and competing signal paths in coupled superconducting resonators", Phys. Rev. B **103**, 094515 (2021).

[70] E. Menzel, "Propagating Quantum Microwaves: Dual-path State Reconstructionand Path Entanglement", Phd thesis, Technische Universität München (2013).

[71] C. W. Gardiner and M. J. Collett, "Input and output in damped quantum systems: Quantum stochastic differential equations and the master equation", Physical Review A **31**, 3761 (1985).

[72] C. W. Gardiner, "Driving a quantum system with the output field from another driven quantum system", Physical Review Letters **70**, 2269 (1993).

[73] H. J. Carmichael, "Quantum trajectory theory for cascaded open systems", Physical Review Letters **70**, 2273 (1993).

[74] Q. Chen, personal communication.

Acknowledgments

This thesis would not exist without the help of many people, which supported, assisted and challenged me throughout my time as a Phd student. To all of you, I want to say: Thank you! Especially I want to thank:

- Rudolf Gross, for giving me the opportunity to work at the Walther-Meissner-Institute.
- Frank Deppe, for fruitful discussions, feedback and support throughout my time at the WMI.
- The whole Qubit group, for discussions, seminars and sitting together in the lab, staring at nonworking measurements;).
- My office mates, for a light hearted office atmosphere that made working quite a bit more enjoyable.
- The whole coffee gang, for so many enjoyable lunches and coffee breaks (and even the occasional frisbee throwing). I'm so happy, that we shared this time together and stayed friends also after most of us left the institute.
- My mum and sister, for always being there for me when I need them. Thanks for all the support and the good times we have together! You are the best family that I could wish for!
- My wife Lara, for giving me constant motivation, especially during the writing phase of my Phd. You pushed me forward, when I needed it most. I love you very much!